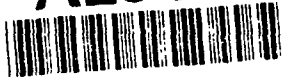②

DTIC
ELECTE
AUG 1 9 1992
S A D

FINAL TECHNICAL REPORT
May 1992
OFFICE OF NAVAL RESEARCH
Contract NO. N0014-91-J-1528

HIGH TEMPERATURE OXIDATION AND ELECTROCHEMICAL STUDIES RELATED TO HOT CORROSION

R. Reidy, D-H. Kim, J. Patton, and G. Simkovich

Department of Material Science and Engineering
The Pennsylvania State University
University Park, Pennsylvania 16802

92 8 17 014

92-22930

8. NAME OF FUNDING/SPONSORING ORGANIZATION	8b. OFFICE SYMBOL (If applicable)	9. PROCUREMENT INSTRUMENT IDENTIFICATION NUMBER			
Metallurgy Branch		N00014-91-J-1528			

8c. ADDRESS (City, State and ZIP Code)	10. SOURCE OF FUNDING NOS.			
Office of Naval Research Arlington, VA 22217	PROGRAM ELEMENT NO.	PROJECT NO.	TASK NO.	WORK UNIT NO.

11. TITLE (Include Security Classification)
High Temperature Oxidation and Electrochemical Studies Related to Hot Corrosion

12. PERSONAL AUTHOR(S)
R. Reidy, D-H. Kim, J. Patton, and G. Simkovich

13a. TYPE OF REPORT	13b. TIME COVERED		14. DATE OF REPORT (Yr., Mo., Day)	15. PAGE COUNT
Final Technical Report	FROM 11-85 TO 5-92		7-27-92	

16. SUPPLEMENTARY NOTATION

17.	COSATI CODES		18. SUBJECT TERMS (Continue on reverse if necessary and identify by block number)
FIELD	GROUP	SUB. GR.	

19. ABSTRACT (Continue on reverse if necessary and identify by block number)

see following page

20. DISTRIBUTION/AVAILABILITY OF ABSTRACT	21. ABSTRACT SECURITY CLASSIFICATION
UNCLASSIFIED/UNLIMITED ☐ SAME AS RPT. ☐ DTIC USERS ☐	

22a. NAME OF RESPONSIBLE INDIVIDUAL	22b. TELEPHONE NUMBER (Include Area Code)	22c. OFFICE SYMBOL

ABSTRACT

This research has examined the transport mechanisms relevant to hot corrosion. Three different approaches were used to elucidate this problem: an examination of the corrosion of the base metal, an exploration of the transport properties in Na_2SO_4, and an investigation in the role of defects in the transport behavior of a protective coating.

The transport properties of molten Na_2SO_4 have been investigated to aid further understanding of hot corrosion processes at 1173 K. Tests were conducted to determine: the effect of height of Na_2SO_4 melts, the effect of electronic short circuiting the Na_2SO_4 melts with gold wires, and the effect of presaturating the salt melt with corrosion products in the hot corrosion process. Basically, these tests showed that neither ionic nor electronic transport in the bulk melt controls the hot corrosion process. However, the amount of Na_2SO_4 present, which is directly proportional to the height of the melt, does affect the rate of corrosion. This was demonstrated by the decrease in rate observed when the melt was presaturated with the corrosion products.

An A.C. impedance technique for the total electrical conductivity, the potentiostatic polarization method for ionic transport numbers, and the steady state polarization method of Wagner and Hebb for the electronic conductivity were employed as a function of Na_2O activity in the melt by controlling the gas atmosphere. These results showed that the conductivities of the pure Na_2SO_4 were of the order of 0.232 $(ohm\text{-}cm)^{-1}$ and varied only slightly with Na_2O activity changes. From the polarization measurements, on the pure Na_2SO_4, it was found that electron conductivity was much higher than electron hole conductivity. The transport numbers were $t_e = 7.0 \times 10^{-3}$ and $t_\bullet = 5.7 \times 10^{-5}$.

Ceria-stabilized zirconia has tremendous potential as a thermal barrier coating in gas turbines and as a fuel cell material. Unlike most stabilized-zirconia systems which are ionic conductors, ceria-doped zirconia has exhibited large electronic contributions at moderate temperatures and oxygen activities. The focus of this research has been to characterize this mixed conduction behavior. Electrical conductivity, ionic transport number, and x-ray diffraction measurements have been performed as a function of composition, temperature, and oxygen partial pressures. At high oxygen activities, oxygen vacancies are the dominant charge carriers while at lower oxygen partial pressures an electron hopping mechanism dominates. Reduced cerium ions and Ce^{3+}-oxygen vacancy associates generate these conducting electrons. Kroger-Vink diagrams have been constructed which detail these mechanisms and describe the point defect behavior for ceria-stabilized zirconia.

Past efforts have concluded that hysteresis-type thermal expansion behavior is due to a repeating monoclinic-tetragonal transformation. High temperature x-ray diffraction found no evidence of the monoclinic phase above 700°C. In 12 and 15 m/o CeO_2-ZrO_2, an unidentified phase has been observed at temperatures between 700-900°C. In low oxygen partial pressures, the same phase has been discovered for 12, 15, and 20 mole percent ceria samples for the same temperature range.

A-1

TABLE OF CONTENTS

LIST OF FIGURES

INTRODUCTION

Due to the severity of their operating environments, marine turbines are subject to a variety of corrosive mechanisms. One of the most formidable forms of attack is hot corrosion, a chemical interaction leading to a breakdown of a protective oxide scale.(1) One of the dominant types of hot corrosion is sulfidation. In sulfidation, NaCl reacts with sulfur found in the fuel to form Na_2SO_4. The sodium sulfate reacts with the protective oxide scale resulting in scale failure.(1,2) This study examines three different aspects of hot corrosion:

1) the mechanisms of hot corrosion attack on nickel, chromium, and nickel-based superalloys,

2) the electronic and ionic transport properties of molten sodium sulfate, and

3) the transport properties of ceria stabilized-zirconia.

These three approaches explore the corrosion of the base metal, the transport through the molten sodium sulfate, and the role of defects in the transport behavior of potential protective coatings.

A large body of work details the roles of Na_2SO_4 and NaCl in the destruction of the oxide scale.(1-8) The mechanisms by which the sulfur compounds disrupt protective oxide scales of nickel-based superalloys in marine turbine hot zones are detailed in several literature surveys.(1,7,9) Bornstein and DeCrescente (2) and Jones (8) describe a general mechanism referred to as the salt fluxing or acid-base reaction model. In sulfidation,

4

Bornstein explains that the oxide scales are insoluble in stoichiometric sodium sulfate, but due to the reaction,

$$Na_2SO_4(l) = Na_2O + SO_3 \qquad\qquad 1)$$
$$\text{(molten salt)} \quad \text{(base)} \quad \text{(acid)}$$
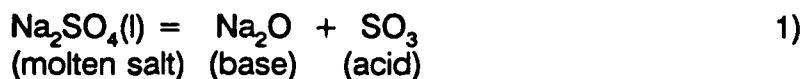
the oxide may dissolve in the base as an anion or in the acid as a cation.(1) From the Lux-Flood theory (10), the activities of the acidic and basic components in the molten salt are fixed by the dissociation constant of the reversible reaction 5).(8) In vanadium attack, a similar dissolution mechanism utilizes the Lewis definition of acids (electron acceptors) and bases (electron donors). A greater understanding of this transport phenomenon could yield the ability to retard or halt this dissolution.

HOT CORROSION OF NICKEL AND CHROMIUM-BASED ALLOYS

Hot corrosion experiments were performed using nickel, chromium and nickel base superalloys as samples. These experiments examined changes in molten salt thickness, short-circuiting of the salt melt with gold wire, and the effects of presaturating Na_2SO_4 with nickel and chromium oxide. All experiments were run as a function of Na_2O activity. The hot corrosion experiments conducted with varying levels of Na_2SO_4 were carried out in an effort to examine the role of bulk diffusion through the melt and its effect on the hot corrosion process. To further study the transport process through the bulk melt, electronic short-circuiting of the melt was done. This was accomplished

5

by attaching gold wires to the samples and extending the wires through the salt. This allowed the evaluation of other transport species and their effect on the hot corrosion process to be examined. In considering the possible role of the dissolution of the oxide scale, the effect of presaturating Na_2SO_4 melts with oxides was performed. The hot corrosion was carried out on pure nickel and chromium in Na_2SO_4 saturated with their respective oxides at various Na_2O activity. Kinetic studies were used to study these changes and are presented here in the form of weight gain versus time plots. In addition, SEM micrographs are used to supplement these plots and aid in understanding the hot corrosion.

Variations in Salt Thickness

Hot corrosion experiments, in which variations in salt thickness were used, allowed transport across the bulk Na_2SO_4 to be studied. The molten salt levels for these experiments ranged from 0.5 cm to 2.0 cm. The experiments were conducted using pure nickel and chromium samples. A metal coupon was placed in a fused silica crucible containing molten Na_2SO_4. All tests were run at 900°C for a period of 50 hours. In addition, all tests were carried out over a range of Na_2O activities corresponding to the acidic and basic fluxing regions and for the Na_2O activity corresponding to the point of minimum solubility for NiO and Cr_2O_3 in Na_2SO_4.

If, as a result of these experiments, it is found that by decreasing the

6

diffusion path (decreasing the thickness of the salt melt) an increase in kinetics occurs, then it may be concluded that the rate limiting step in this process could be transport across the bulk melt. Additionally, if it is found that, by decreasing the diffusion path across the Na_2SO_4, no change in the kinetics of the system is observed then it may be concluded that the transport across the salt is relatively fast and is not the rate limiting step. However, if by decreasing the diffusion path across the salt and a decrease in kinetics occurs, then one may conclude that first, transport across the bulk is not the rate limiting step, and second, that the hot corrosion process may involve the ability of the Na_2SO_4 to accommodate the products of the hot corrosion process.

The salt melt for experiments conducted nickel in the acidic and basic fluxing regions, for nickel, had a Na_2O activity of 6.3×10^{-16} and 1.4×10^{-8} respectively. The Na_2O activity corresponding to minimum solubility of NiO in Na_2SO_4 was 5.01×10^{-11}. For experiments carried out using chromium, the Na_2O activities corresponding to acidic and basic fluxing were 1.0×10^{-16} and 1.0×10^{-14} respectively. The minimum solubility experiments for chromium were carried out with a Na_2O activity of 5.01×10^{-16}.

The results from hot corrosion tests performed in the acidic fluxing region on pure nickel and chromium samples are shown in Figures 1 and 2 respectively. The total weight gain for nickel ranged from 109.2 mg/cm^2 (2.0 cm thickness of Na_2SO_4) to 52.6 (0.5 cm thickness of Na_2SO_4). For chromium the total weight gain ranged form 55.3 mg/cm^2 (2.0 cm thickness of Na_2SO_4) to

7
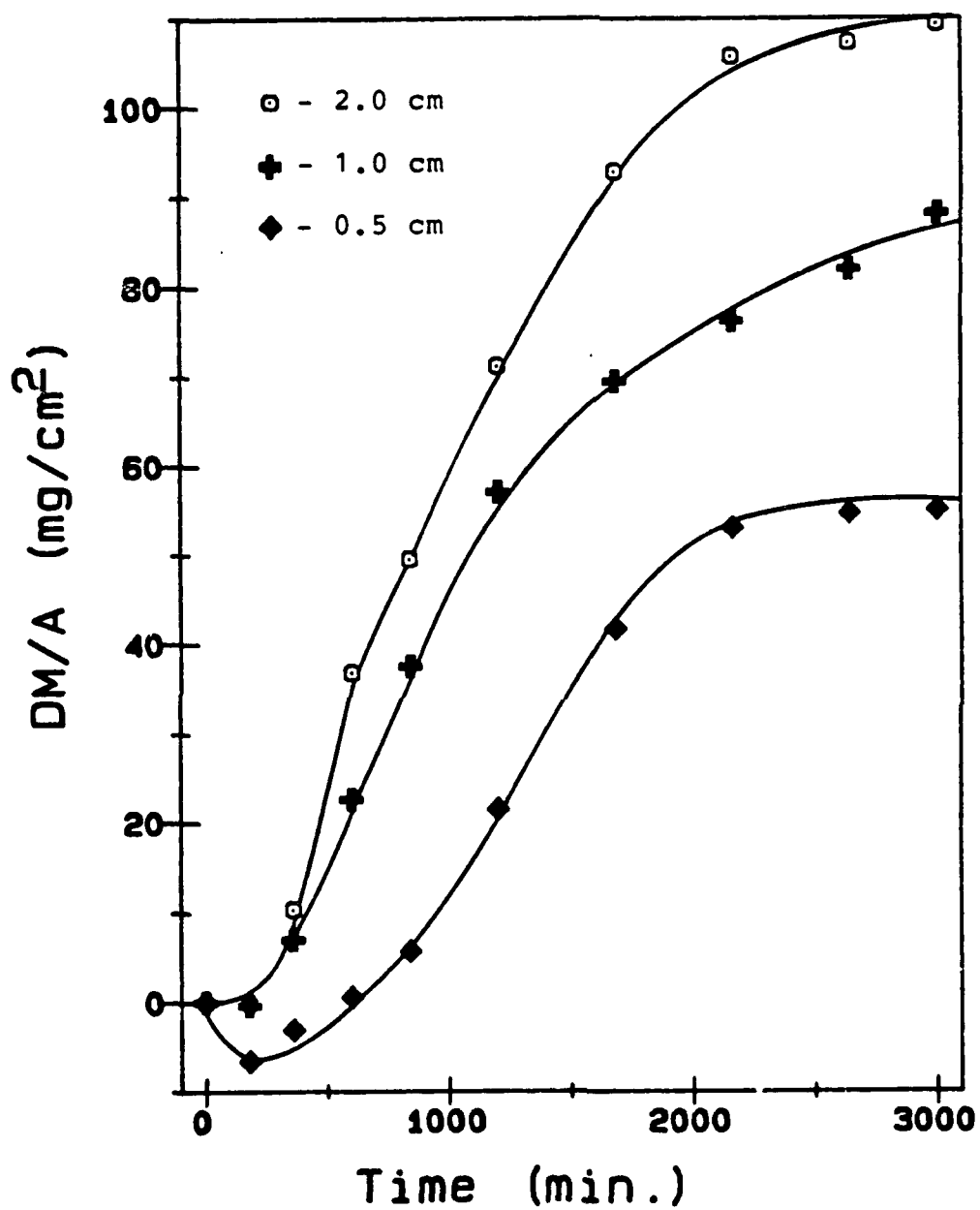
Figure 1 Weight gain per unit area of pure nickel as a function of Na_2SO_4 thickness (900°C and acidic fluxing condition, where $a_{Na2O} = 6.3 \times 10^{-16}$).

8
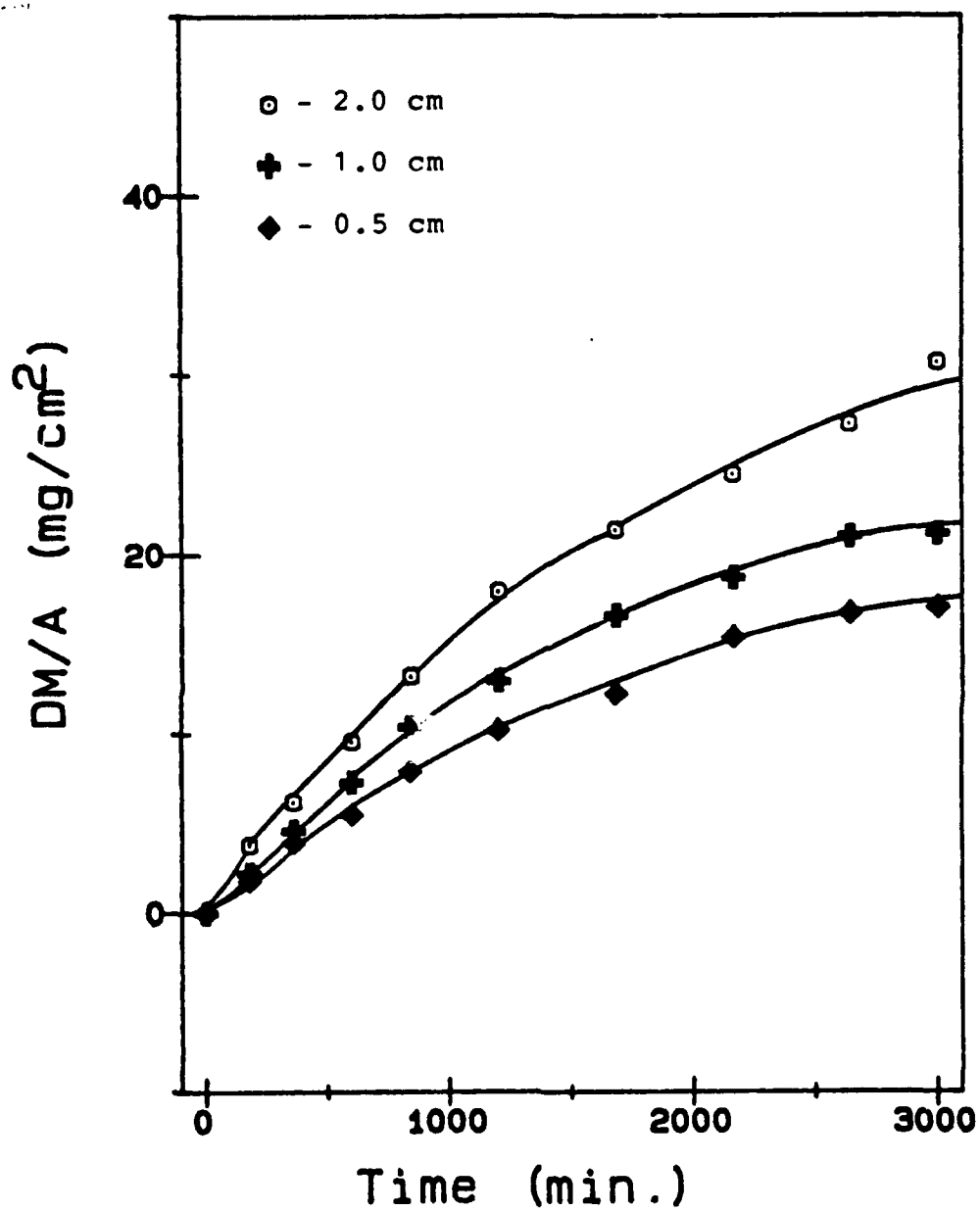
Figure 2 Weight gain per unit area of pure chromium as a function of Na_2SO_4 thickness ($900^\circ C$ and acidic fluxing condition, where $a_{Na2O} = 1.0 \times 10^{-16}$).

9

29.1 mg/cm^2 (0.5 cm thickness of Na$_2$SO$_4$). As can be seen from Figures 1 and 2, an increase in the height of the molten salt results in an increase in the weight gains per unit area of the corroding samples i.e. the kinetics of the system increase with increasing thickness. It can also be seen by comparing results from the nickel and chromium samples that chromium appears less affected by the increase in Na$_2$SO$_4$. Results from experiments conducted in the basic fluxing region are shown in Figures 3 and 4 for nickel and chromium respectively. As with the acidic fluxing region, there was a greater weight increase with increasing salt thickness with chromium and a greater resistance to the hot corrosion process than nickel. The overall weight gains for the basic fluxing region when compared to the acidic fluxing region were not as large for nickel while for chromium they were approximately equal. Results from experiments conducted at minimum solubility for NiO and Cr$_2$O$_3$ are shown in Figures 3 and 4 respectively. At minimum solubility, the results resemble those from the acidic and basic fluxing regions, i.e. an increase in kinetics corresponding to the increase in salt thickness. However, the overall kinetics of the system at minimum solubility is slower when compared to the results from the acidic and basic fluxing regions. This comparison is shown in Figures 5 and 6 for nickel and chromium respectively.

Presence of Na$_2$SO$_4$ on a nickel surface will subject the nickel to simultaneous attack from both sulfur and oxygen. In addition, Na$_2$SO$_4$ promotes accelerated oxidation of the metal or alloy. The mechanism for the
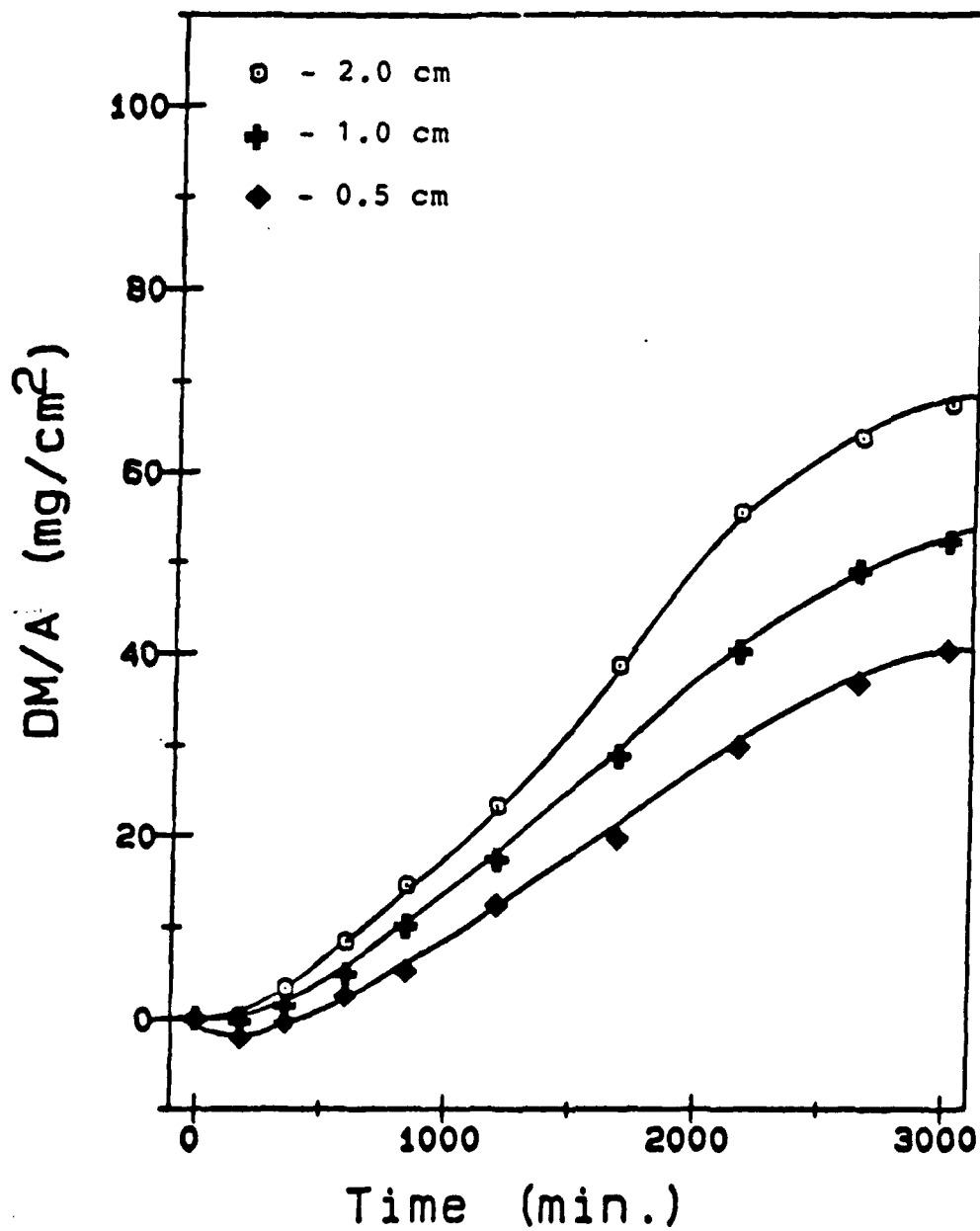
Figure 3 Weight gain per unit area of pure nickel as a function of Na_2SO_4 thickness (900°C and basic fluxing condition, where $a_{Na2O} = 1.4 \times 10^{-8}$).
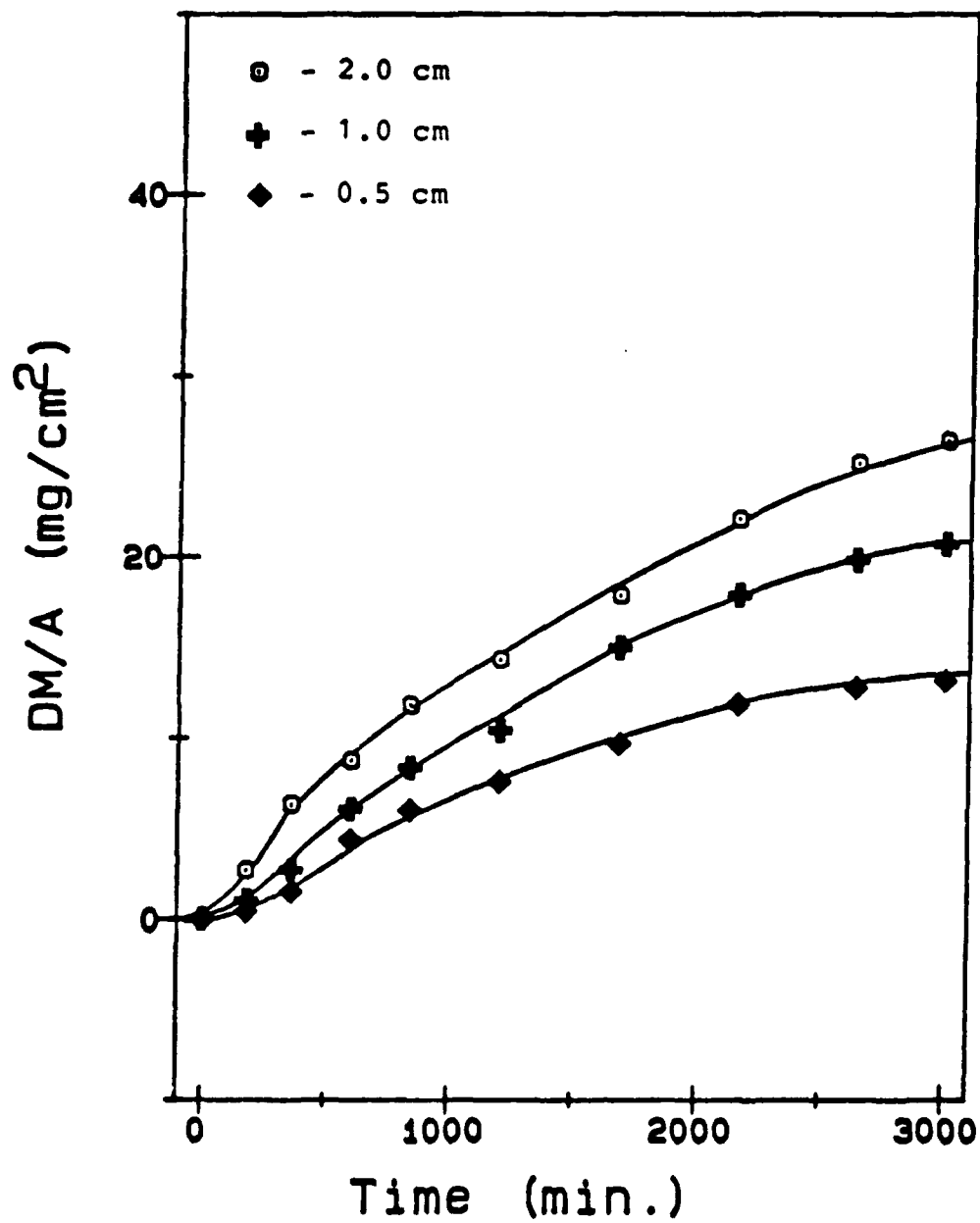
Figure 4 Weight gain per unit area of pure chromium as a function of Na_2SO_4 thickness (900°C and basic fluxing condition, where $a_{Na2O} = 1.0 \times 10^{-14}$).
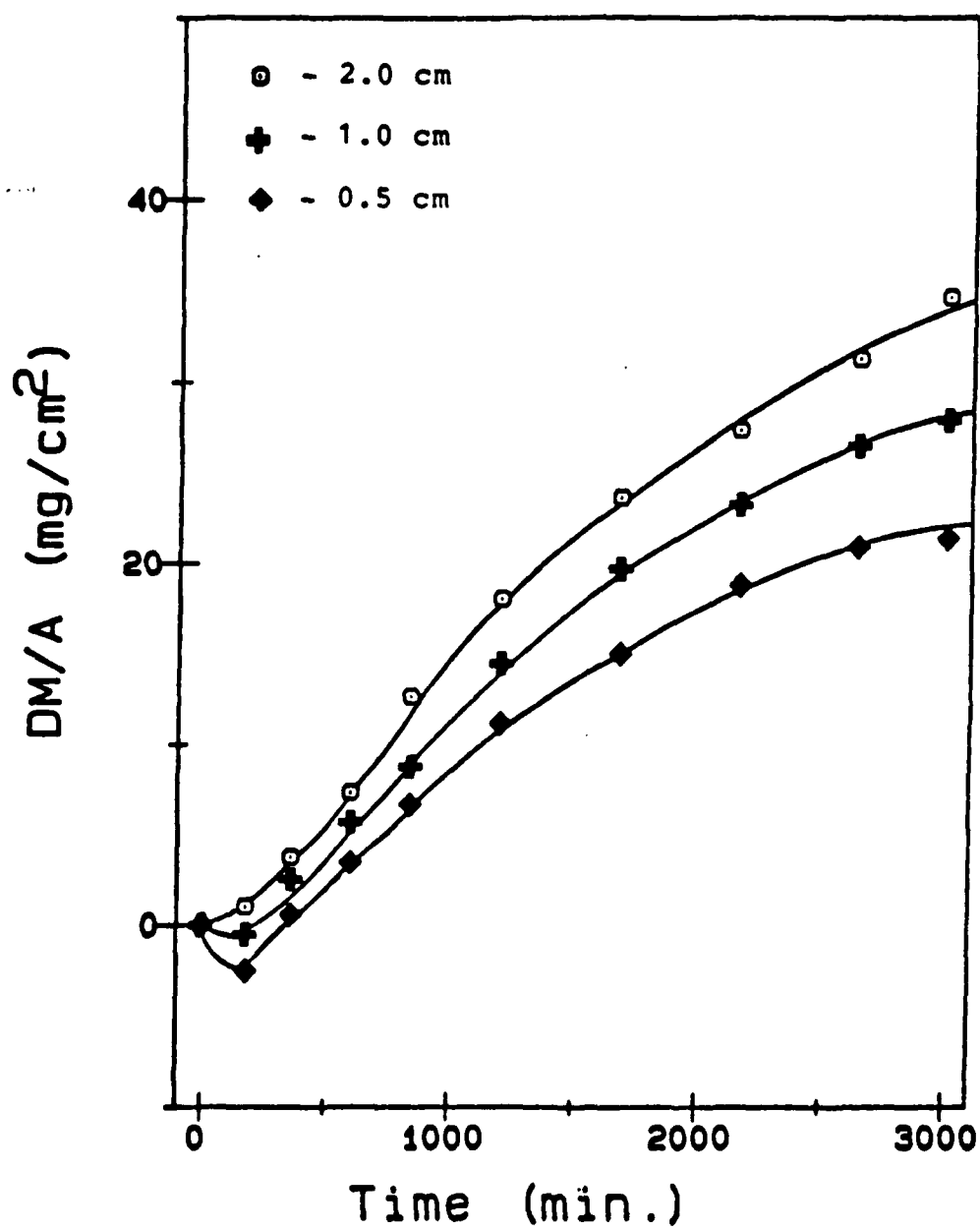
Figure 5   Weight gain per unit area of pure nickel as a function of Na_2SO_4 thickness (900°C at minimum solubility, where $a_{Na2O} = 5.0 \times 10^{-11}$).

13
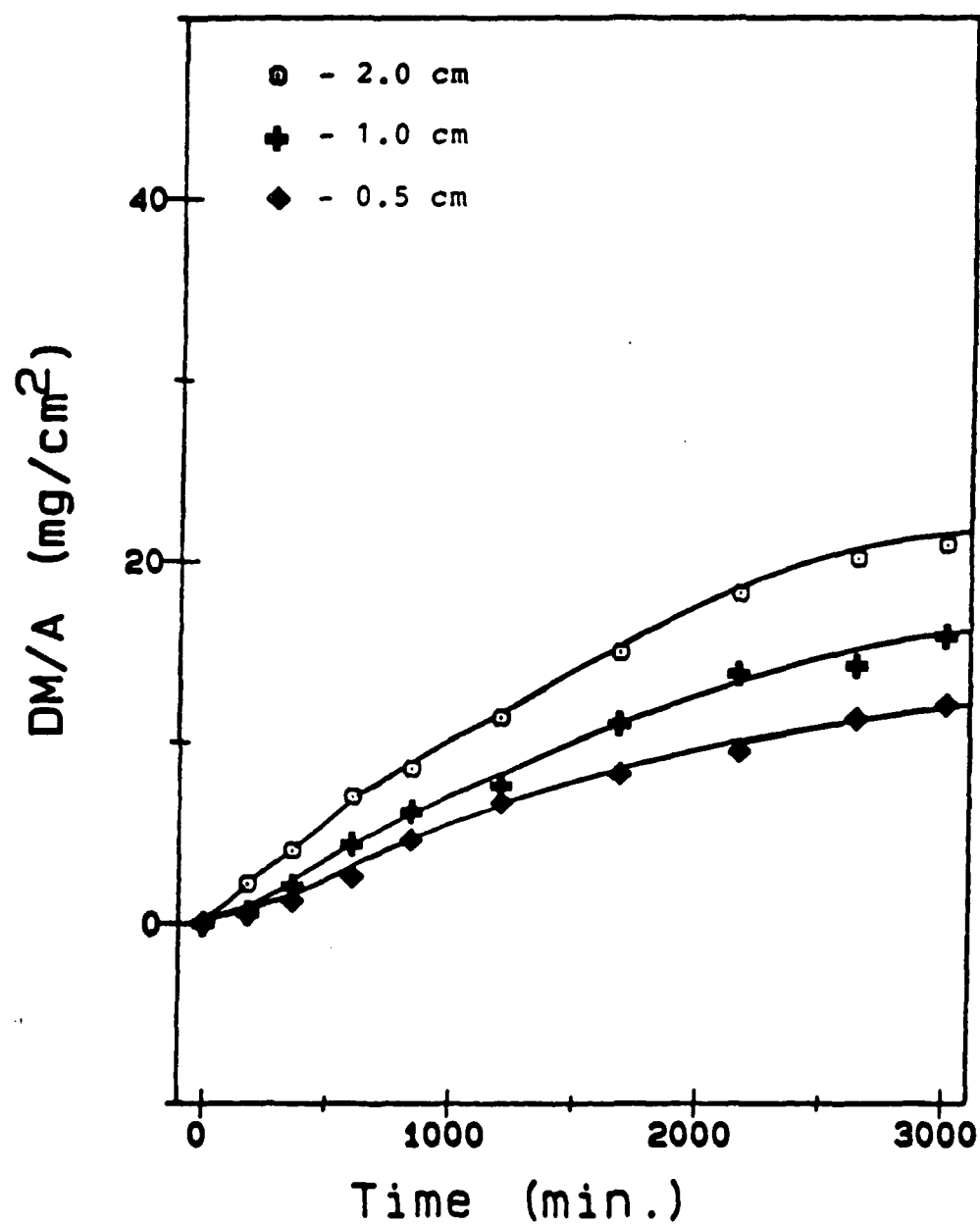
Figure 6 Weight gain per unit area of pure chromium as a function of Na_2SO_4 thickness (900°C at minimum solubility, where $a_{Na2O} = 5.0 \times 10^{-16}$).

14

accelerated attack is a function of the inter-relationship between the magnitudes of the respective oxygen and sulfur activities.

The mechanism involved in the accelerated oxidation or hot corrosion of nickel by Na_2SO_4 was described by Goebel and Pettit (11). Although the work carried out by Goebel and Pettit was done in pure O_2 at 1, it is still applicable. The stability and composition of the salt melt is considered in terms of its thermodynamic equilibrium and the associated activities of sulfur and oxygen. These activities are related to the formation of the reaction products i.e. NiO and NiS. Figure 7 shows the stability diagrams for nickel in the Na_2SO_4 system.(12) Goebel and Pettit found that upon exposure to Na_2SO_4, the formation of NiO forms immediately on the surface with the equation written as follows:

$$Na_2SO_4 + 4Ni = Na_2O + 3NiO + NiS \qquad 2)$$

Thus, as a result of this reaction the oxygen activity in the salt is reduced. This promotes the formation of NiS by diffusion of sulfur to the nickel/oxide interface. Because of this, the formation of NiS causes the sulfur activity to then decrease and the oxide activity (O^{2-}) of the Na_2SO_4 to increase. This results in the formation of a porous non-protective NiO scale and the presence of NiS.

15
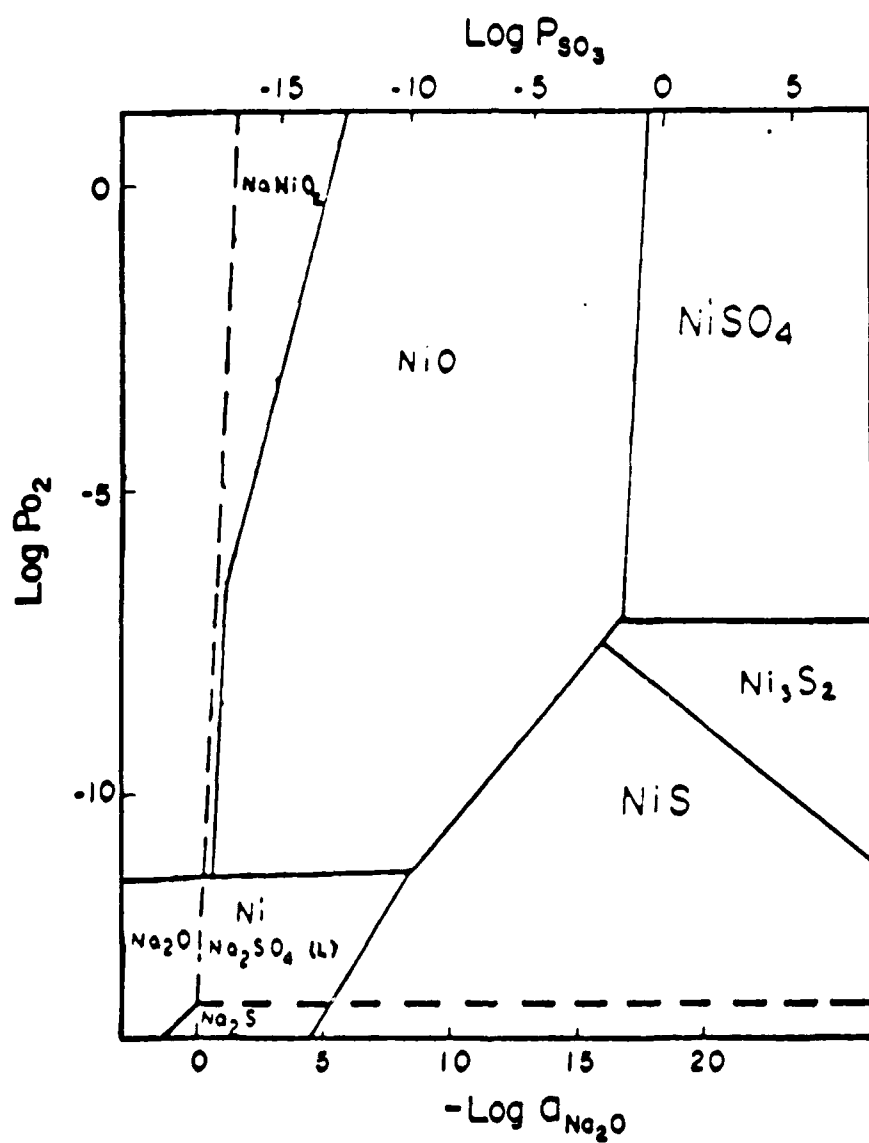
Figure 7 Stability diagram for NiO in Na_2SO_4.(12)

protective NiO scale and the presence of NiS.

From photomicrographic and Debye-Scherrer x-ray diffraction evidence, it appears then that the following sequence of events are taking place:

1. NiO forms initially on the surface of the nickel sample, thereby decreasing the oxygen activity and increasing the sulfur activity.

2. Sulfur is diffusing to the metal/oxide interface forming the compound Ni_3S_2 in the porous NiO.

3. The removal of sulfur from the salt increases the oxygen ion activity.

4. The oxide ions (O^{2-}) then react with nickel to form a porous non-protective oxide layer.

5. Accelerated oxidation (hot corrosion) takes place.

6. The Na_2SO_4 becomes saturated with NiO and a decreasing oxidation rate results.

Since the gas environment contains SO_2 and SO_3, the reaction is continuous. Therefore, the sulfur activity is sufficiently high in order to continuously form Ni_3S_2. It would appear then that the observed results obtained from the hot corrosion experiments on nickel are in agreement with present literature (11).

SEM photographs taken of the chromium samples after being subjected to the hot corrosion experiments indicate that the corrosion of chromium is much less severe than with the pure nickel. This agrees with the results obtained from the weight gain versus time plots in which chromium appeared less affected by the increase in salt thickness than did nickel. Also, no sulfides were

17
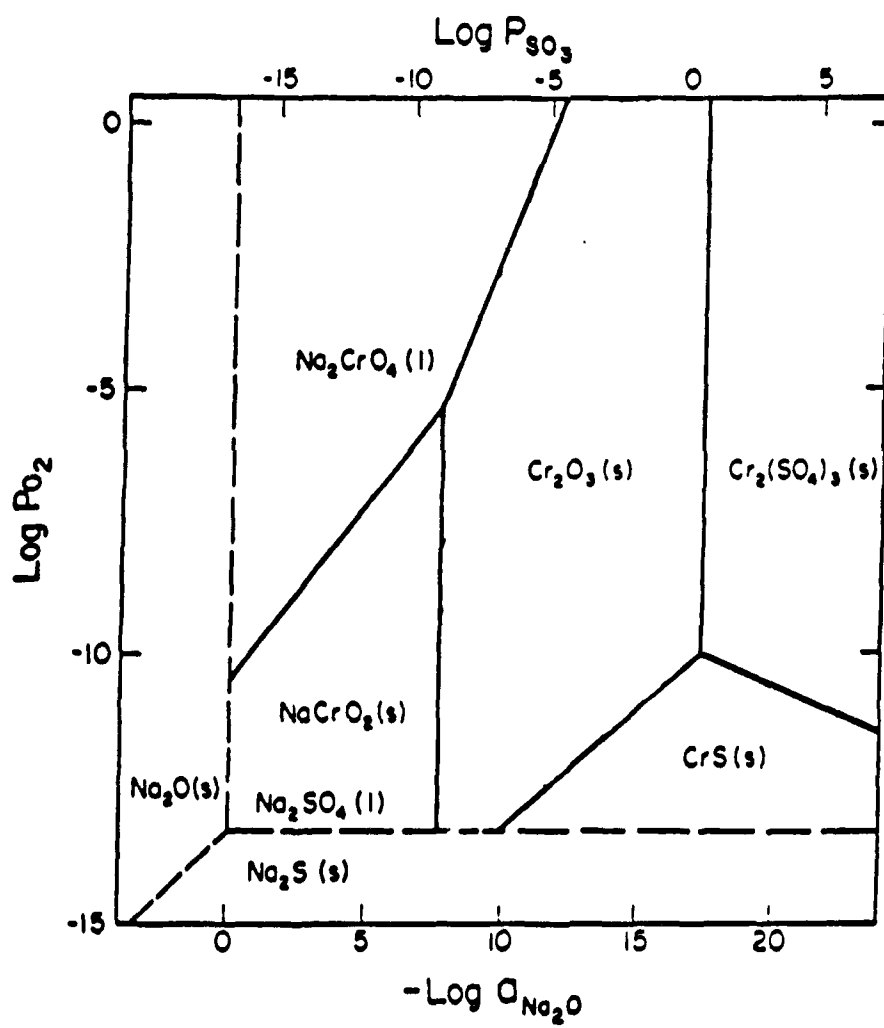
Figure 8 Stability diagram for Cr_2O_3 in Na_2SO_4.(12)

observed in the Cr_2O_3 scale. In addition, the lack of any sulfide phase present seems in agreement with the stability diagram for chromium in Na_2SO_4 shown in Figure 8 based on the Na_2O activities at which the experiments were run.

As a result of these kinetic studies, it may be concluded that, over the range of Na_2O used, an increase in the diffusion path by increasing salt thickness does not decrease the kinetics of the hot corrosion process but rather accelerates the reaction. In addition, it appears that there may be some relation between the Na_2O activity and the kinetics of the reactions occurring during hot corrosion. This relation may be explained from examining the solubility diagrams for both NiO and Cr_2O_3, shown in Figure 7 and 8 respectively. In these diagrams it can be seen that, in the basic fluxing region, the solubility decreases as a function of the Na_2O activity until the minimum solubility is reached. The acidic fluxing regions shows an increase in solubility as a function of Na_2O activity. Corresponding to the activity of Na_2O used in the hot corrosion tests, nickel and chromium show a higher solubility of NiO and Cr_2O_3 in Na_2SO_4 in the acidic fluxing region than either the basic fluxing region and the point of minimum solubility. In addition, nickel and chromium in the acidic fluxing region also exhibited the largest weight gains while the experiments conducted in the basic fluxing region yielded the next largest followed by the tests run at minimum solubility.

Electronic Short-Circuiting of Salt Melt

To further examine the transport through Na_2SO_4, gold wires were added to the samples of nickel and chromium and tests run as a function of Na_2O activity and salt thickness. Gold wires were attached to the samples in an attempt to electronically short-circuit the salt melt. This allowed the study of the other transport species and their effect on the hot corrosion process. In addition, this allowed the study of electronic transport across the gas/salt interface since the gold wire served to electronically short-circuit the gas/melt interface.

Transport through the Na_2SO_4 must occur via the motions of ions and/or electronic species in such a manner as to maintain electrical neutrality. Thus anion motions toward the metal must be accompanied by either cations or electron holes moving in the same directions or by the countermotion of other anions and electrons. Therefore, if the observed reactions, following the addition of the gold wires, shows an increase in the corrosion rate, it may then be concluded that electronic transport through the melt is rate determining. If the rate is unchanged, then it may be concluded that electron transport through the melt is not rate controlling. During the experiments in which the gas/salt interface is short-circuited, if there is an increase in the corrosion rate then electronic transport across this interface is rate controlling. Further, if the corrosion rate observed during experiments does not change, then the gas/melt interface or diffusion across this interface is not rate controlling.

The results from the electronic-short circuiting experiments are shown in

20
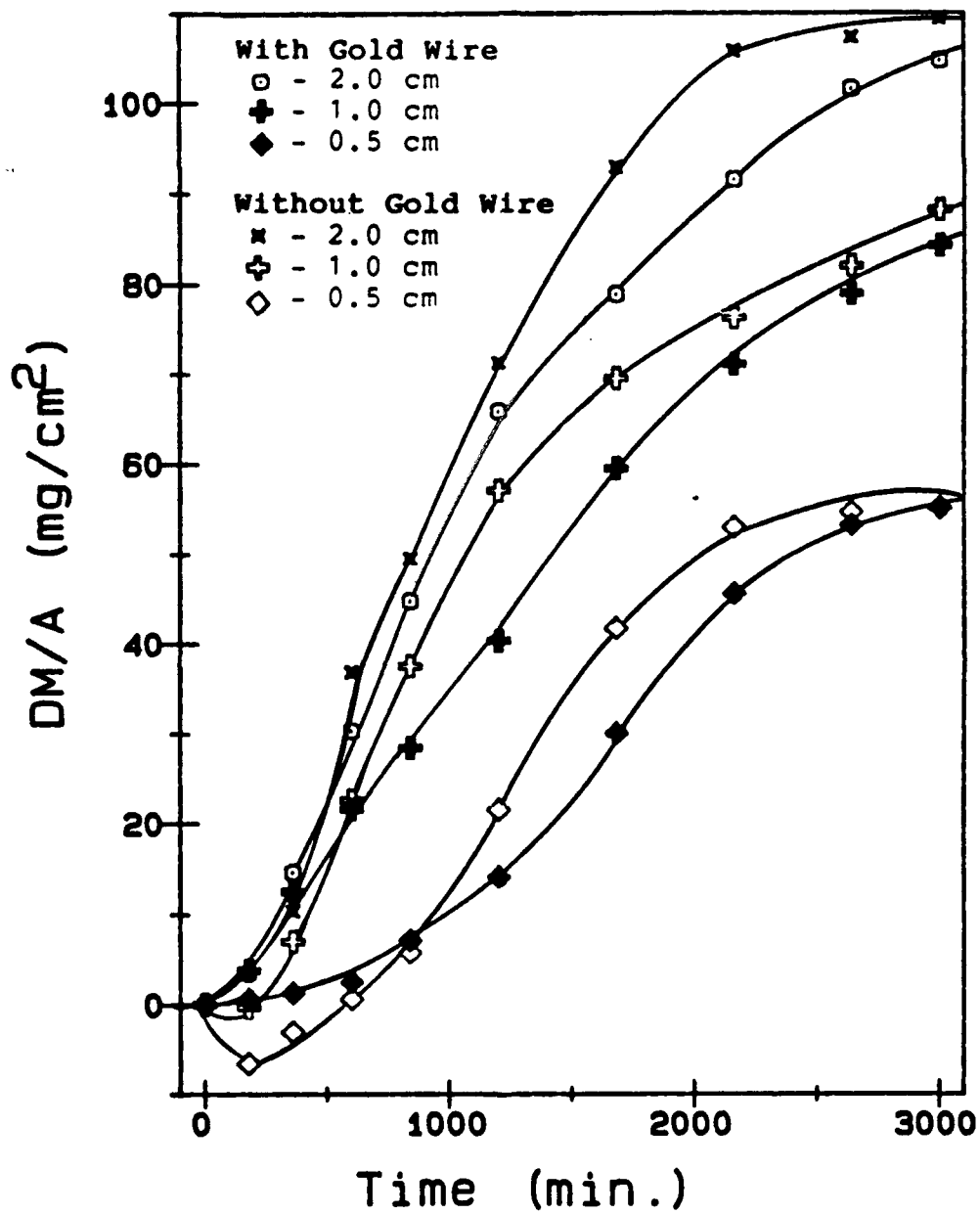
Figure 9 Comparison of weight gains per unit area of pure nickel with and without attached gold wires as a function of salt thickness (900°C and acidic fluxing condition).

Figure 10 Comparison of weight gains per unit area of pure chromium with and without attached gold wires as a function of salt thickness (900°C and acidic fluxing condition).
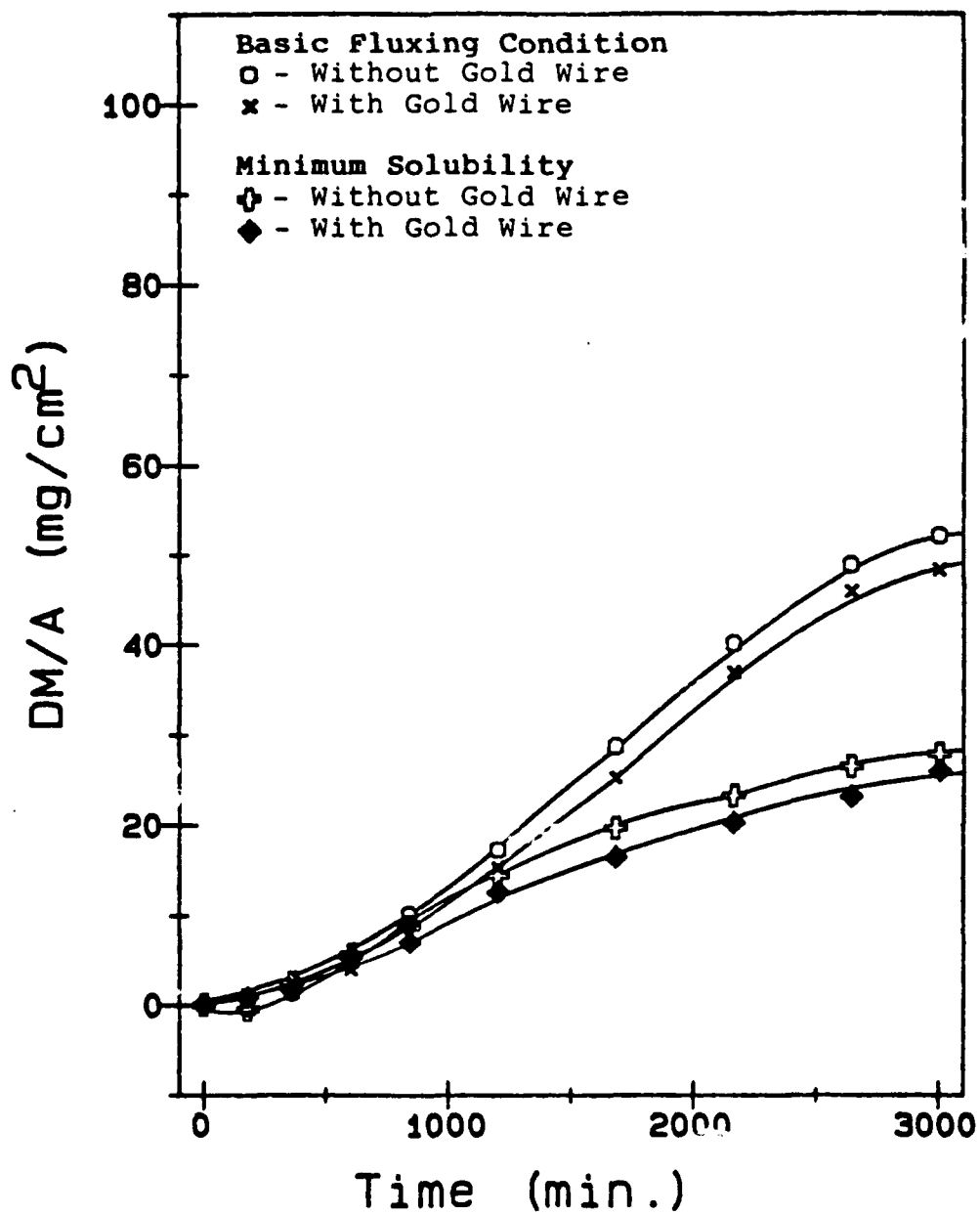
Figure 11 Comparison of weight gains per unit area of pure nickel with and without attached gold wires at a salt thickness of 1 cm (900°C, basic fluxing condition, and minimum solubility).

23
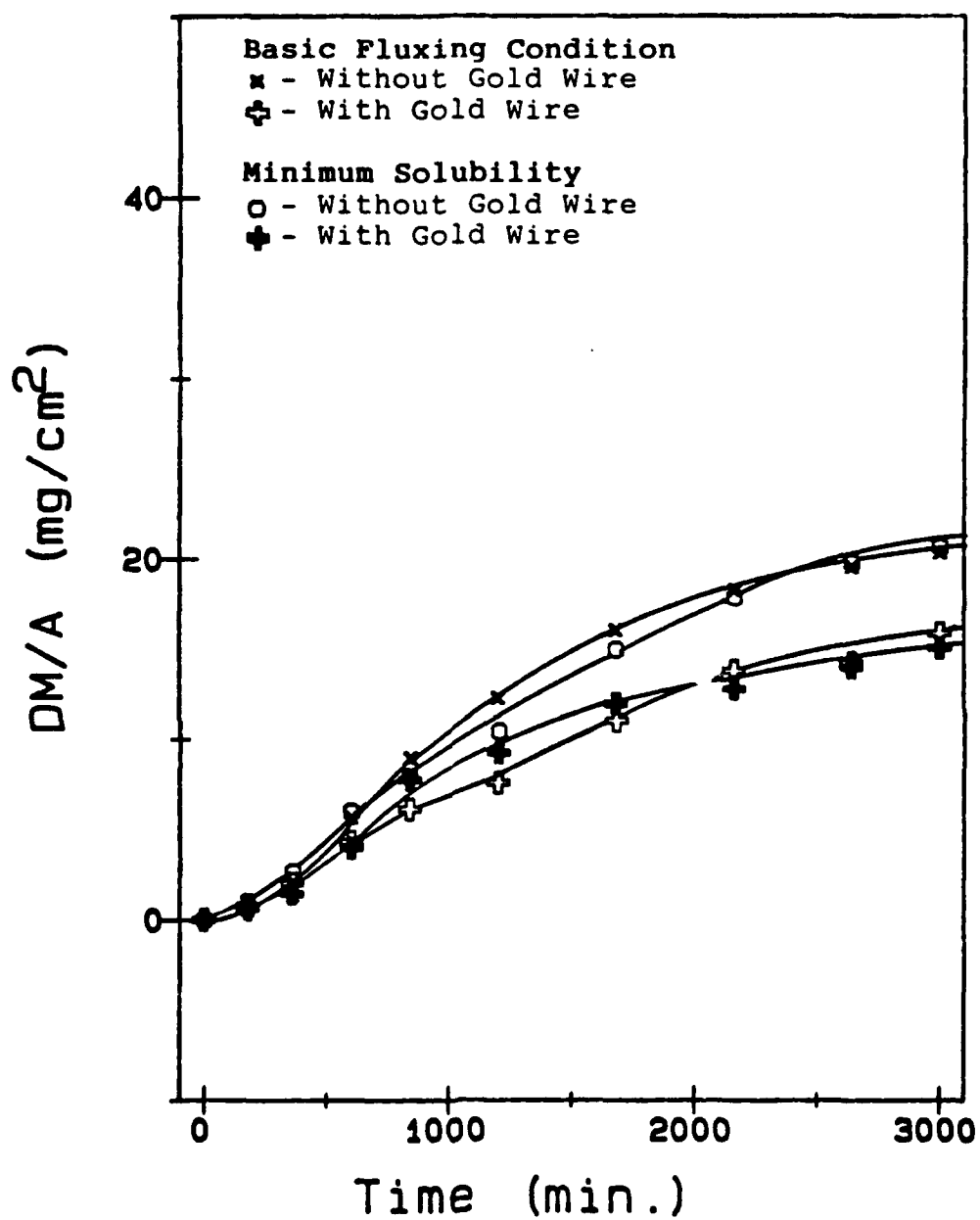
Figure 12 Comparison of weight gains per unit area of pure chromium with and without attached gold wires at a salt thickness of 1 cm (900°C, basic fluxing condition, and minimum solubility).

Figure 9 and 10 for nickel and chromium respectively. These figures show a comparison between experiments run as a function of Na_2SO_4 thickness and a Na_2O activity of 6.1 x 10^{-16} and 1.0 x 10^{-16} for nickel and chromium respectively. It can be seen from these plots that the kinetics of system appear relatively unchanged by the addition of the gold wires. Figures 11 and 12 show results from additional experiments conducted at other Na_2O activities. Again it appears that the kinetics of the system appear unchanged either as a function of Na_2SO_4 or Na_2O activity with or without the addition of the gold wires. Photomicrographs of nickel and chromium samples taken from experiments conducted at the basic fluxing condition as well as at the minimum solubility point for NiO and Cr_2O_3 were consistent with the results found in the previous section.

The combination of the findings from this series of experiments and of previous work demonstrate that transport, electronic or otherwise, through the melt is not rate determining. In addition, these results together with the salt thickness results seem to imply that the gas/salt interface has very little control over the hot corrosion process.

Presaturation of Oxide Melts

Results from previous experiments show the kinetics of the system increase with salt thickness and transport through the bulk molten salt and the gas/salt

25

interface has little or no effect on the reaction. However, it does appears that the hot corrosion process may be a function of the Na_2O activity of the salt melt and the solubility of the reaction product in Na_2SO_4. Therefore, the possible role of the dissolution of the scale must be considered. When considering the increase in weight gain per unit as the amount of salt increases, it may be as a result of the capacity of the Na_2SO_4 and its ability to accept the soluble product. Hence, once the molten salt has been completely saturated, the hot corrosion process should be slowed significantly.

A series of experiments were conducted using nickel and chromium samples in hot corrosion studies with Na_2SO_4 saturated with their respective oxides. As before, these experiments were conducted as a function of salt thickness and Na_2O activity. By use of the solubility curves for NiO and Cr_2O_3 in Na_2SO_4, the maximum solubility for a given amount of Na_2SO_4 can be determined. Therefore, hot corrosion experiments can be conducted using salt melts saturated with the correct amounts of oxide equal to their maximum solubility. In this way, the effect of presaturated Na_2SO_4 on the hot corrosion process can be evaluated.

The results for experiments carried out in the acidic fluxing region for nickel and chromium are given in Figure 13 and 14. A comparison of results from tests without presaturated oxide salt melts for nickel and chromium is shown in Figure 15. It can be seen from this comparison that the kinetics of the system for nickel appear to be slowed drastically while chromium is relatively

26
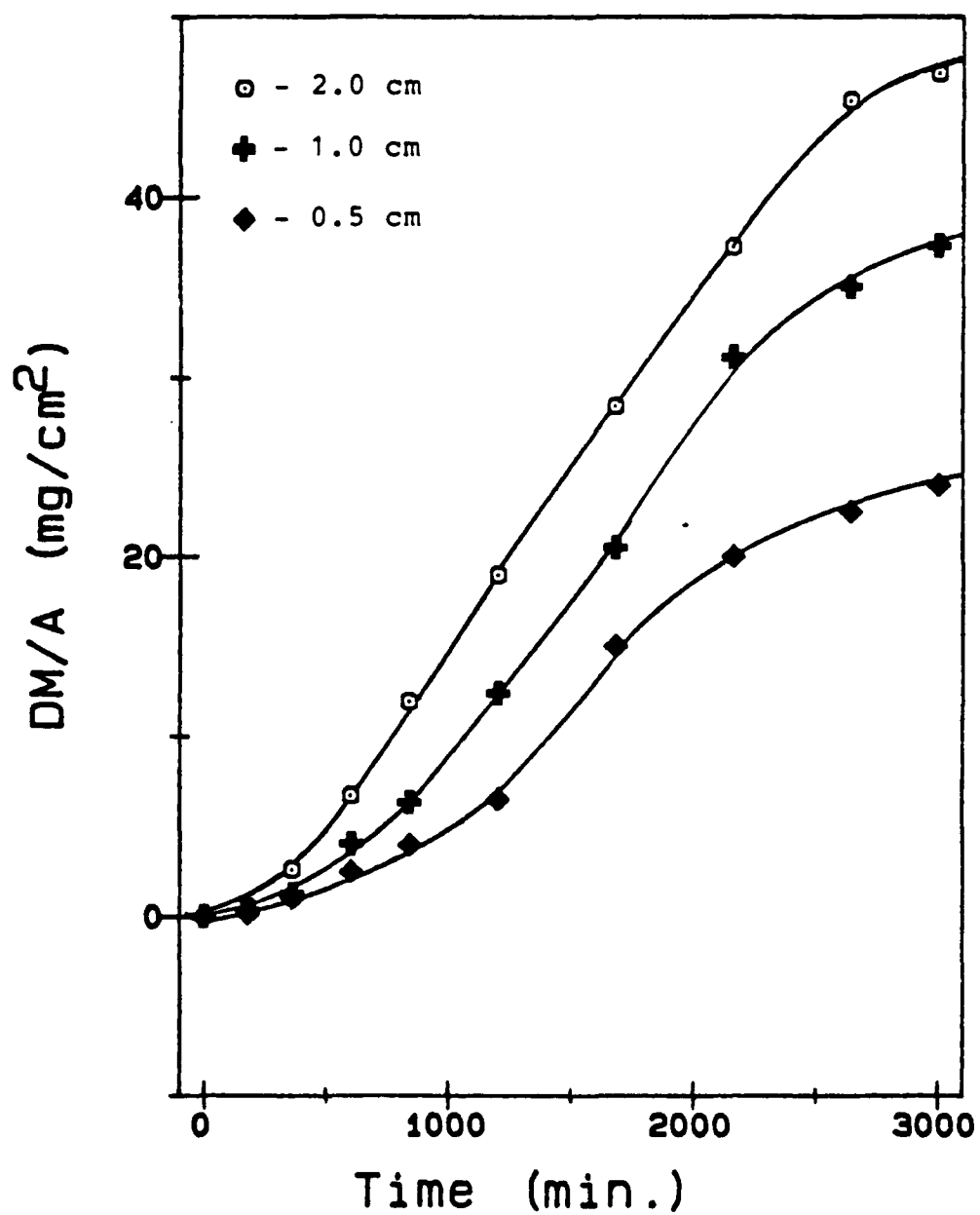
Figure 13 Weight gain per unit area of pure nickel in Na_2SO_4 saturated with NiO as a function of salt thickness (900°C and acidic fluxing condition).
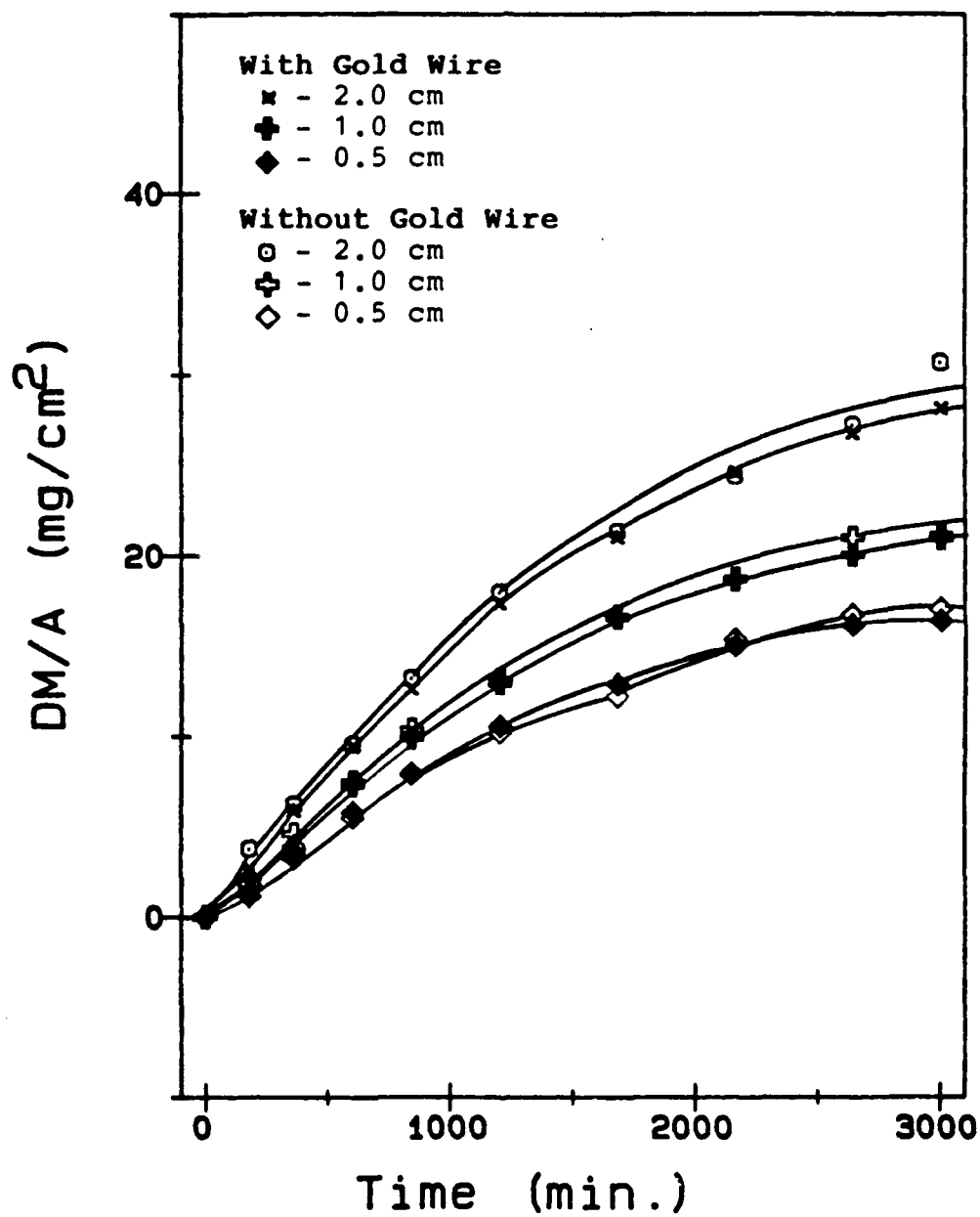
27
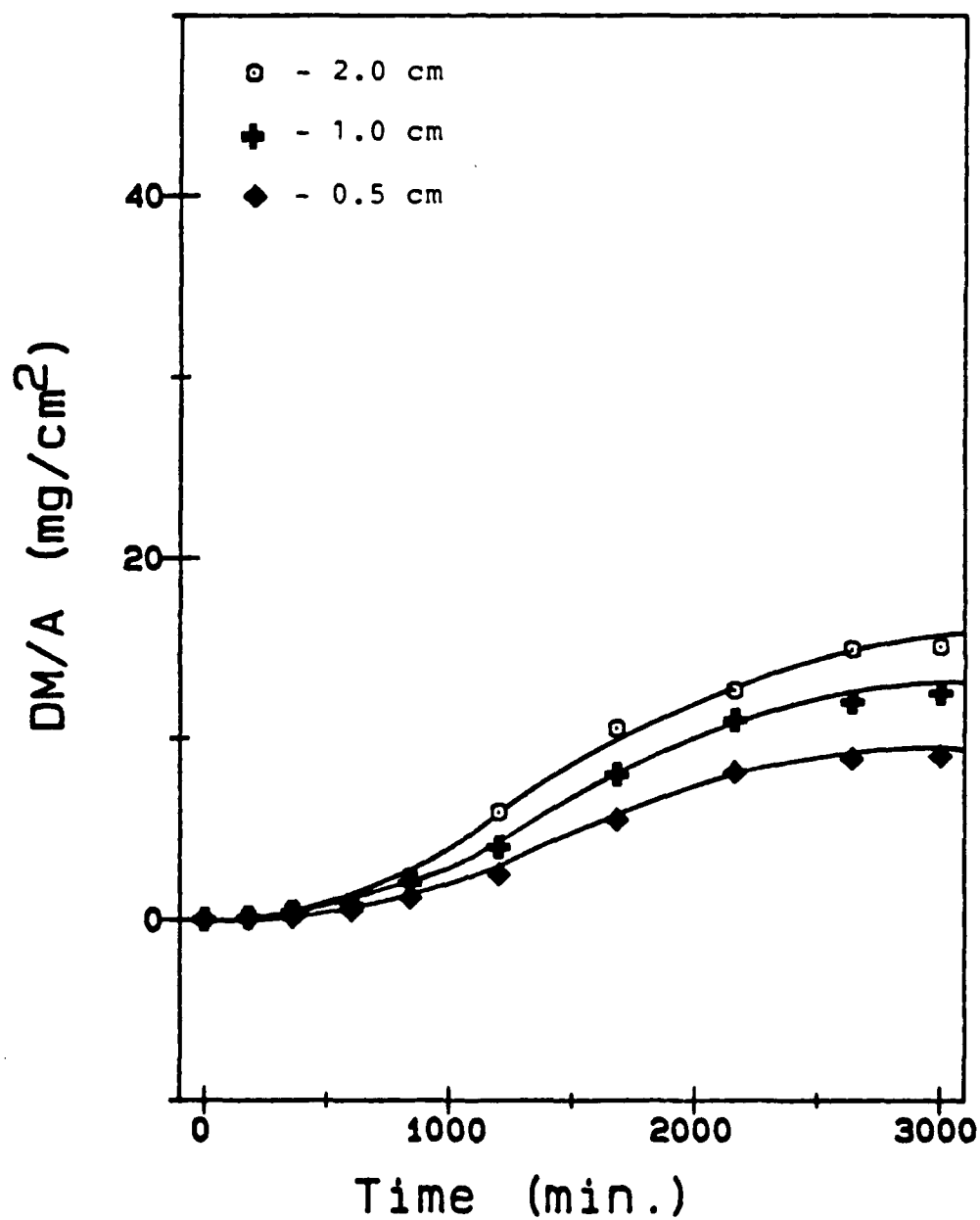
Figure 14 Weight gain per unit area of pure chromium in Na_2SO_4 saturated with Cr_2O_3 as a function of salt thickness (900°C and acidic fluxing condition).
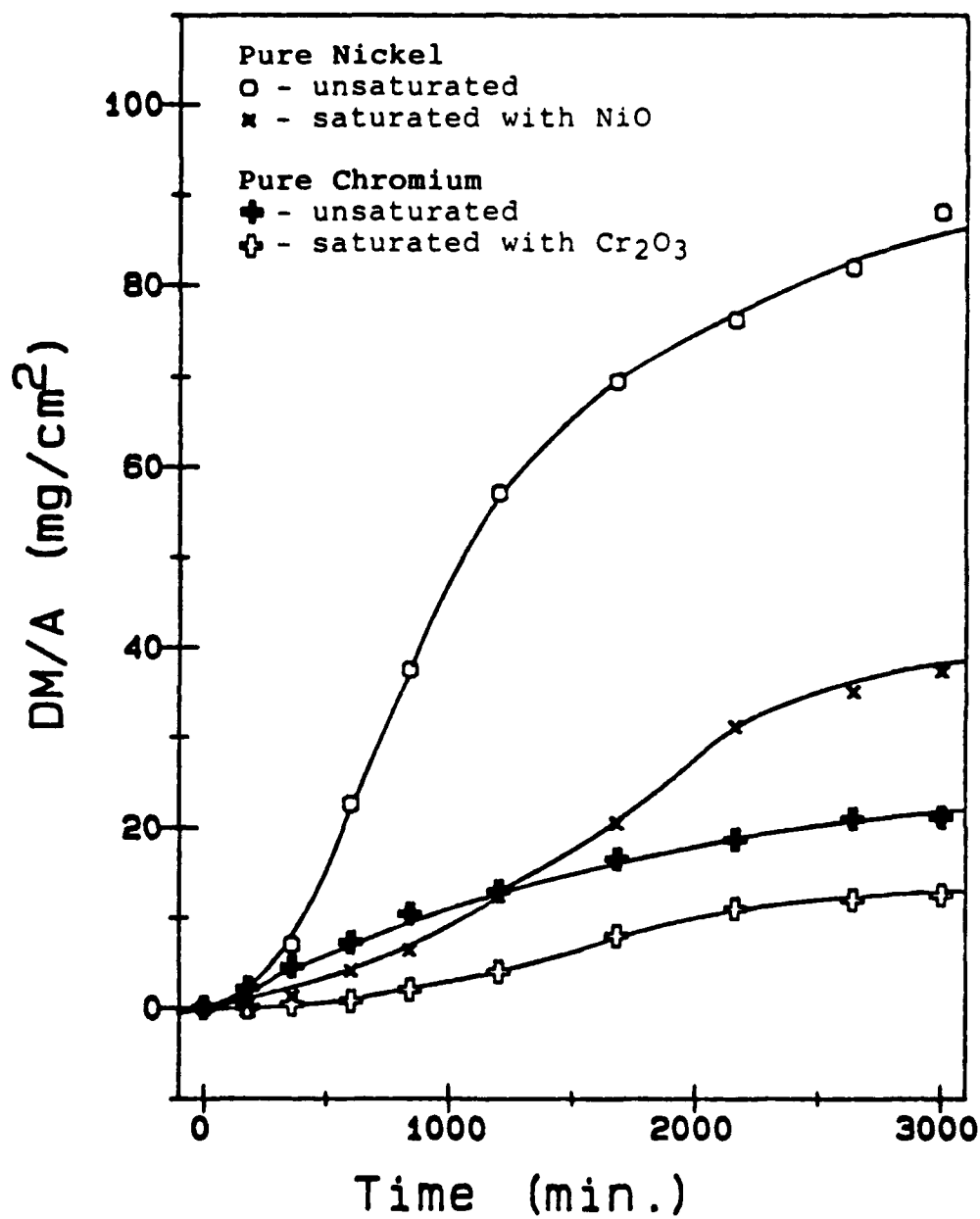
Figure 15 Comparison of weight gains for pure nickel and chromium in Na_2SO_4 unsaturated and saturated with their respective oxides at a salt thickness of 1 cm (900°C and acidic fluxing condition).
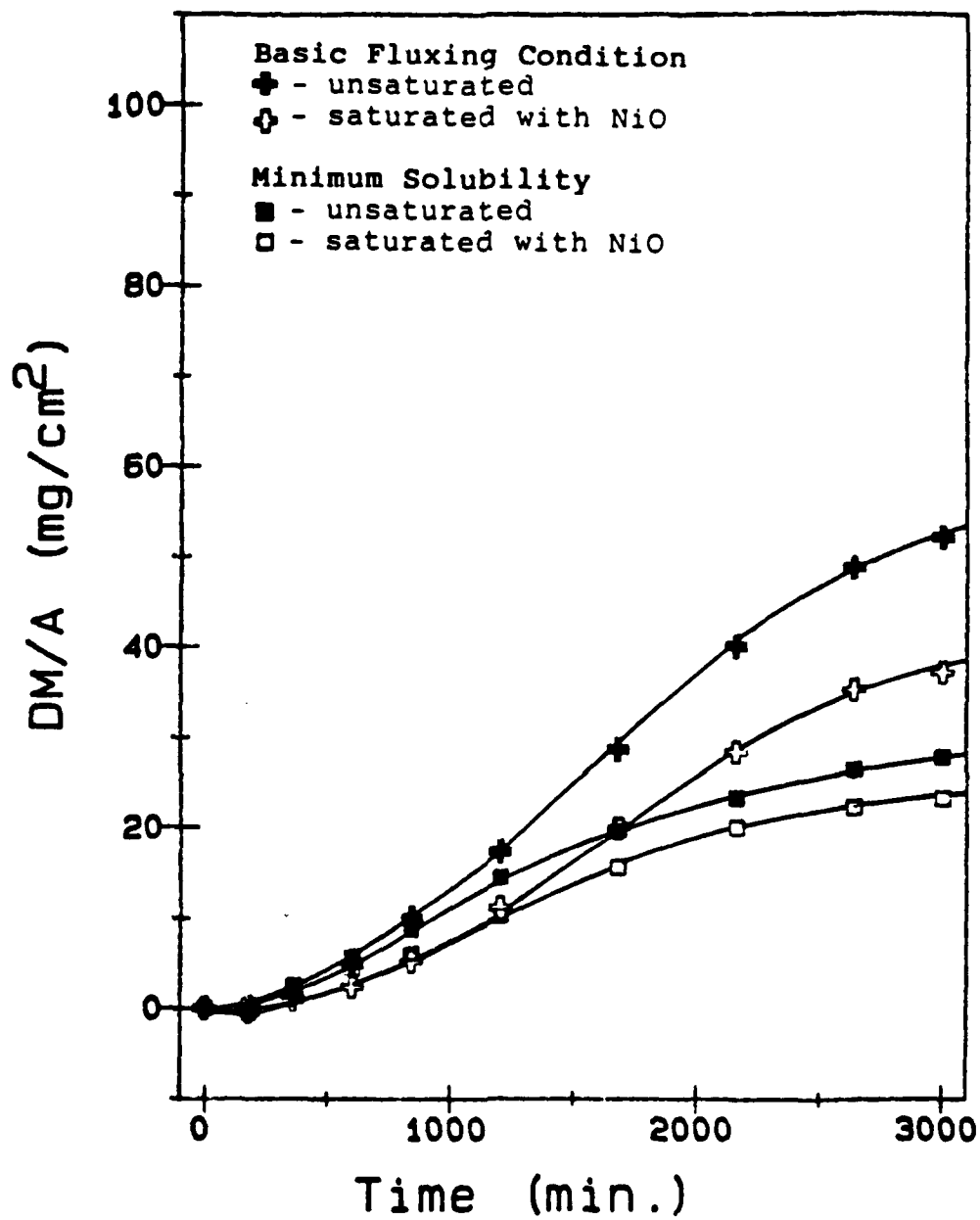
Figure 16 Comparison of weight gains for pure nickel in Na_2SO_4 unsaturated and saturated with NiO at a salt thickness of 1 cm (900°C, basic fluxing condition, and minimum solubility).
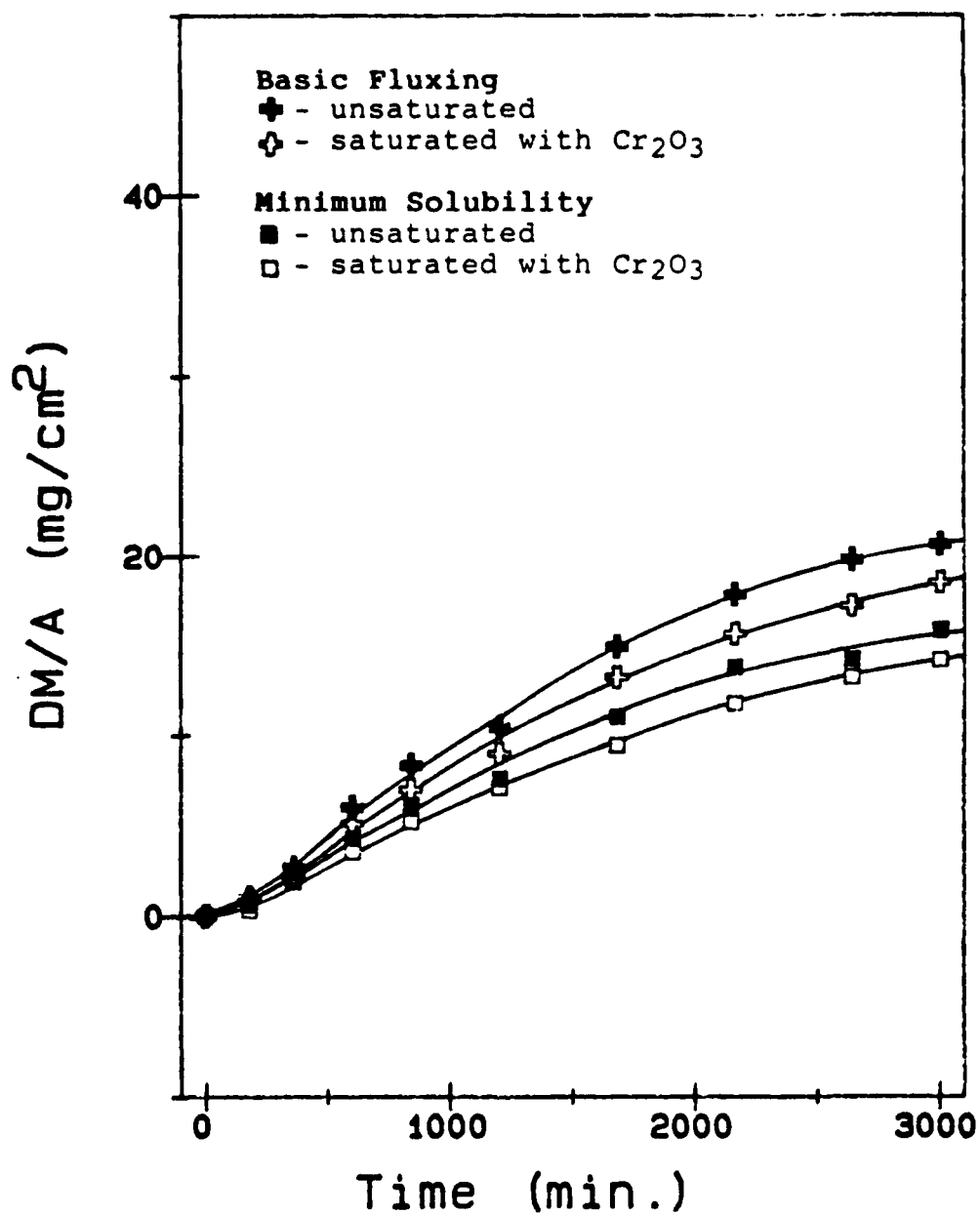
Figure 17   Comparison of weight gains for pure chromium in Na_2SO_4 unsaturated and saturated with Cr_2O_3 at a salt thickness of 1 cm (900°C, basic fluxing condition, and minimum solubility).

unchanged. Results from experiments conducted at the basic fluxing condition and the minimum solubility are shown in Figures 16 and 17. The kinetics for the basic fluxing condition have been also been slowed considerable for nickel while the minimum solubility shows very little change. Chromium shows little change at either the basic fluxing condition or at minimum solubility. SEM pictures taken of nickel samples used in experiments involving presaturated salt melts vary considerably from samples taken from unsaturated Na_2SO_4. The NiO shows sign of hot corrosion attack but the normal protective scale is still intact. The same was found for samples at the basic fluxing condition as well as at minimum solubility. SEM photographs of chromium samples show the protective Cr_2O_3 present and no change from samples tested in unsaturated salt melts.

These results appear to indicate that the hot corrosion process may be a function of the amount of Na_2SO_4 present and thus, its ability to accept a soluble product. In addition, it can be seen that the effect of varying salt thickness as well as the effect of saturating the salt melt with the appropriate oxides is still manifested in a decrease in kinetics.

Na$_2$SO$_4$ STUDIES

A large thrust of this experimental program was to obtain the transport properties in the aggressive molten salt Na$_2$SO$_4$. Table I list such information obtained from this study. The total electrical conductivity determined by utilizing an A.C. impedance technique indicates that pure Na$_2$SO$_4$ melt had a somewhat low total conductivity as compared to most ionic melts.

The cationic transport numbers of a pure Na$_2$SO$_4$ melt were obtained by utilizing the potentiostatic polarization technique. The results indicate that a pure Na$_2$SO$_4$ melt is a cationic conductor over a wide range of Na$_2$O activities at 1173 K. From the above results, the diffusivity of cations, one of the important kinetic parameters, can be estimated as 8.1 x 10^{-6} cm^2/sec.

The Wagner-Hebb type polarization experiments provided the electron and electron hole conductivities in a pure Na$_2$SO$_4$ melt at 1173 K. From these measurements along with total electrical conductivity data, the transport numbers of electrons, t$_e$, and electron holes, t$_\bullet$, were calculated. Such experimental investigations show that the electronic conduction occurs primarily via the transport of electrons as indicated in Table I.

Table 1 Transport Properties of a Pure Na_2SO_4 Melt

Ionic Transport Properties

$\sigma_{total} = 0.232 \ (\Omega\text{-cm})^{-1}$

$t_{Na+} = 0.9838$

$D_{Na+} = 8.083 \times 10^{-6} \ (cm^2/sec)$

$\mu_{Na+} = 7.996 \times 10^{-5} \ (cm^2/volt\text{-sec})$

$C_{Na+} = 0.0294 \ (mole/cm^3)$

Electronic Transport Properties

$\sigma_e = 1.638 \times 10^{-3} \ (\Omega\text{-cm})^{-1}$

$\sigma_\bullet = 1.337 \times 10^{-5} \ (\Omega\text{-cm})^{-1}$

$t_e = 7.055 \times 10^{-3}$

$t_\bullet = 5.76 \times 10^{-5}$

$D_e = 3.15 \times 10^{-3} \ (cm^2/sec)$

$\mu_e = 0.031 \ (cm^2/volt\text{-sec})$

$C_e = 5.462 \times 10^{-7} \ (mole/cm^3)$

The diffusion coefficient of electrons which are the predominant minor defects in a Na_2SO_4 melt, was determined by the voltage relaxation method suggested by Weiss (13). Its average value is 3.15 ($\pm$0.17) $\times 10^{-3}$ cm^2/sec. The corresponding drift mobility of electrons is 0.031 cm^2/volt-sec which is identical to that in Na-NaCl melts at 1166 K with 0.81 mole percent of sodium.

The effects of Cr_2O_3, Al_2O_3, and SiO_2 on total conductivity as well as the electronic conductivity were examined by the A.C. impedance technique and Wagner-Hebb type polarization experiments. The introduction of Cr_2O_3 at concentration levels of 10^{-3}, 10^{-2}, 10^{-1}, and 1 mole percent has significant effects on the total electrical conductivity i.e., as the amount of Cr_2O_3 in the melt

increases the total electrical conductivity decreases. Additionally, the dissolved chromia decreases electron conductivities and increases electron hole conductivities. The addition of Al_2O_3 into the melt does not produce significant changes in total electrical conductivities. However, the Al_2O_3 lowers electron conductivities tremendously and increases electron hole conductivities slightly. The melts containing silica show small changes in total electrical conductivities but massive decrements in electron conductivities.

The oxidation and/or hot corrosion rate is often considered as a product of total conductivity, sum of ionic transport numbers, and the transport number of major electronic species. The results observed in the present investigation indicate the sum of ionic transport numbers is nearly unity; therefore, the product of total conductivity and the transport number of the major electronic species is considered. Such considerations are described in Figure 18 as a function of mole percent of oxides in the melt. The value of total conductivity x transport number of major electronic species for a pure Na_2SO_4 is 1.64 x 10^{-3}. As indicated in this figure the reaction rate is decreased as a function of mole percent of each oxide in the melt. For Cr_2O_3 and Al_2O_3 melts, it levels off at about 10^{-1} mole percent while SiO_2 melts do not level off even in supersaturated melts. It is clear from this figure that the addition of silica has the utmost effect on decreasing reaction rates among those protective oxides tested.

35
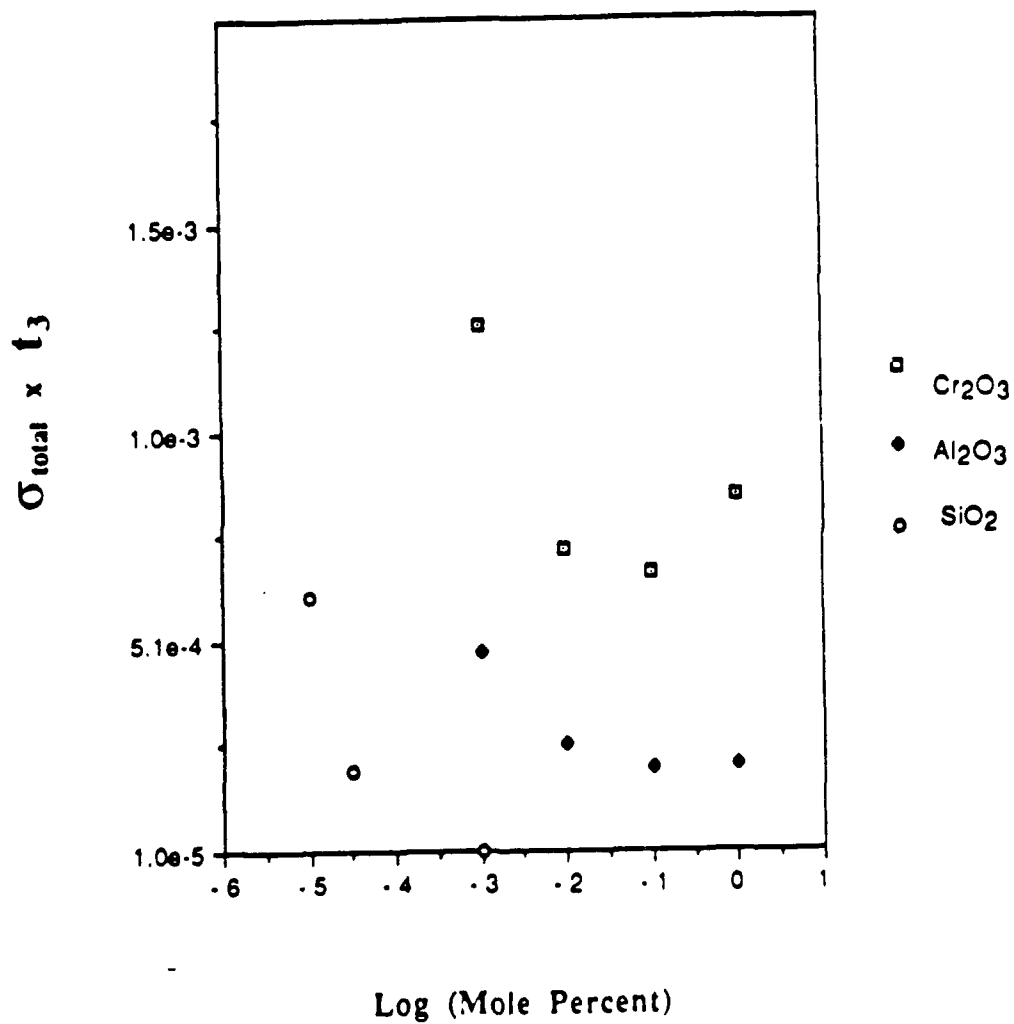
Figure 18 The product of the average value of the total conductivity and the transport number of the electronic species as a function of mole% of the oxides added in the melt at 1173K.

ELECTRONIC AND DEFECT BEHAVIOR IN CERIA-STABILIZED ZIRCONIA

In this work, electrical conductivity, ionic transport numbers, and x-ray diffraction patterns of ceria-stabilized zirconia have been studied as a function of temperature, oxygen partial pressure, and composition. From these experimental results, a point defect model has been proposed which resolves several experimental considerations. Kroger-Vink diagrams have been constructed for two cases of this model.

Electrical Conductivity as a Function of Oxygen Activity

In order to examine the defect structure of an oxide, electrical properties are often measured as a function of oxygen activity and dopant concentration. By altering either the oxygen activity or the dopant concentration, one may change the concentration or the identity of the point defects in the system.

Using CO/CO_2 and O_2/CO_2 gas mixtures to control oxygen activity, the electrical conductivities of 12, 15, and 20 mole percent CeO_2 samples were measured at two or three temperatures (Figures 19-21). In Figure 19, the 12m/o ceria specimen displayed remarkably consistent behavior. Two distinct regions were clearly evident: a domain independent of oxygen activity and a range dependent on oxygen partial pressure. As temperature increased, the electrical conductivity and the threshold oxygen activity for P_{O2} dependence correspondingly increased. The negative slope of the oxygen dependent region strongly suggested n-type semi-conductive behavior. Further, the
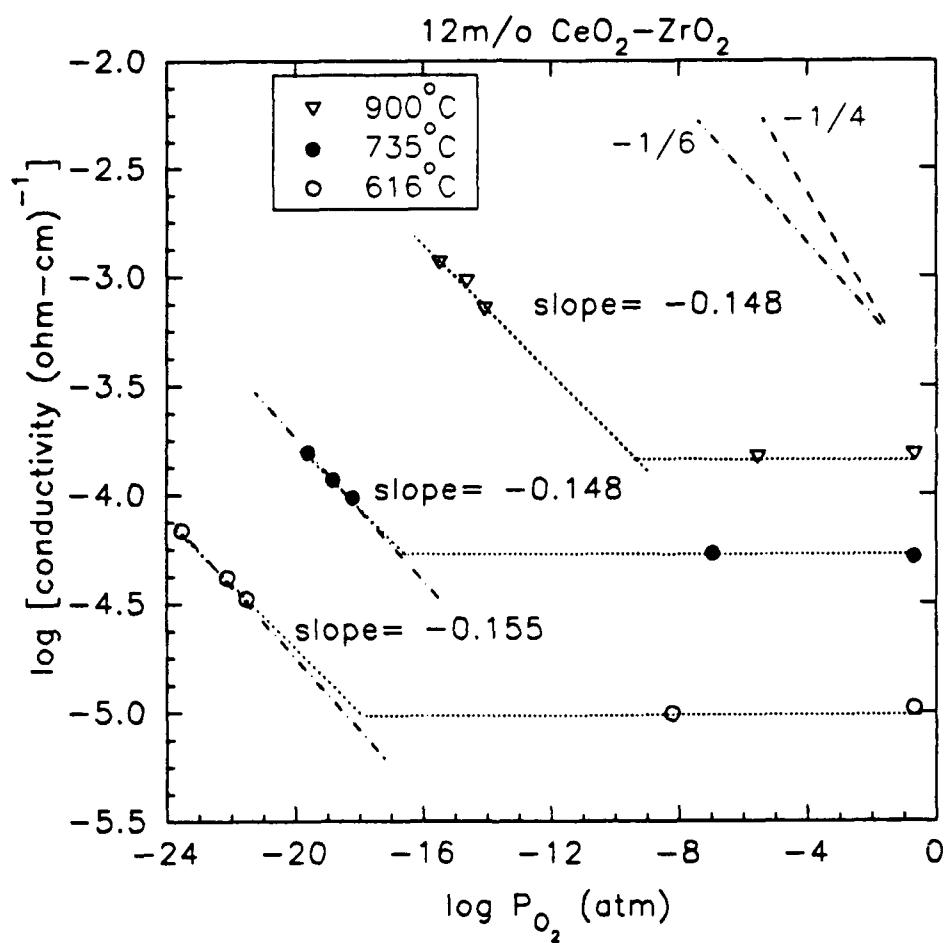
Figure 19 Electrical conductivity as a function of oxygen partial pressure for 12 mole percent CeO_2-ZrO_2.

38
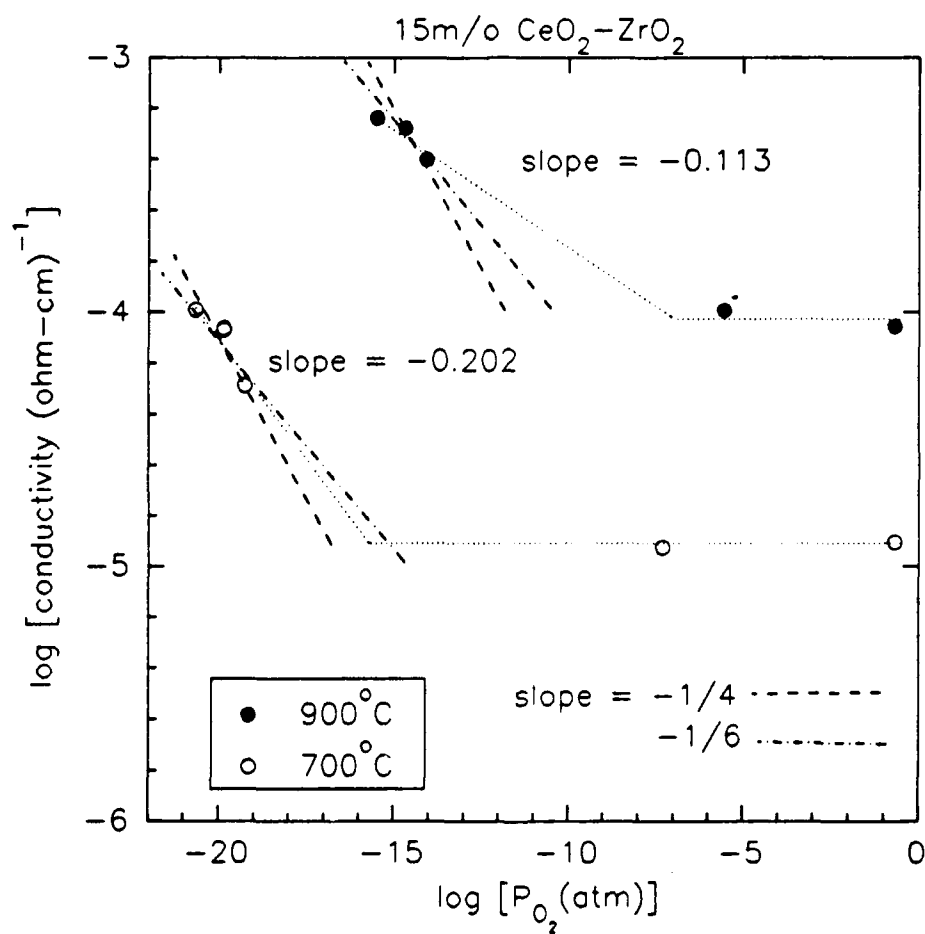
Figure 20 Electrical conductivity as a function of oxygen partial pressure for 15 mole percent CeO_2-ZrO_2.
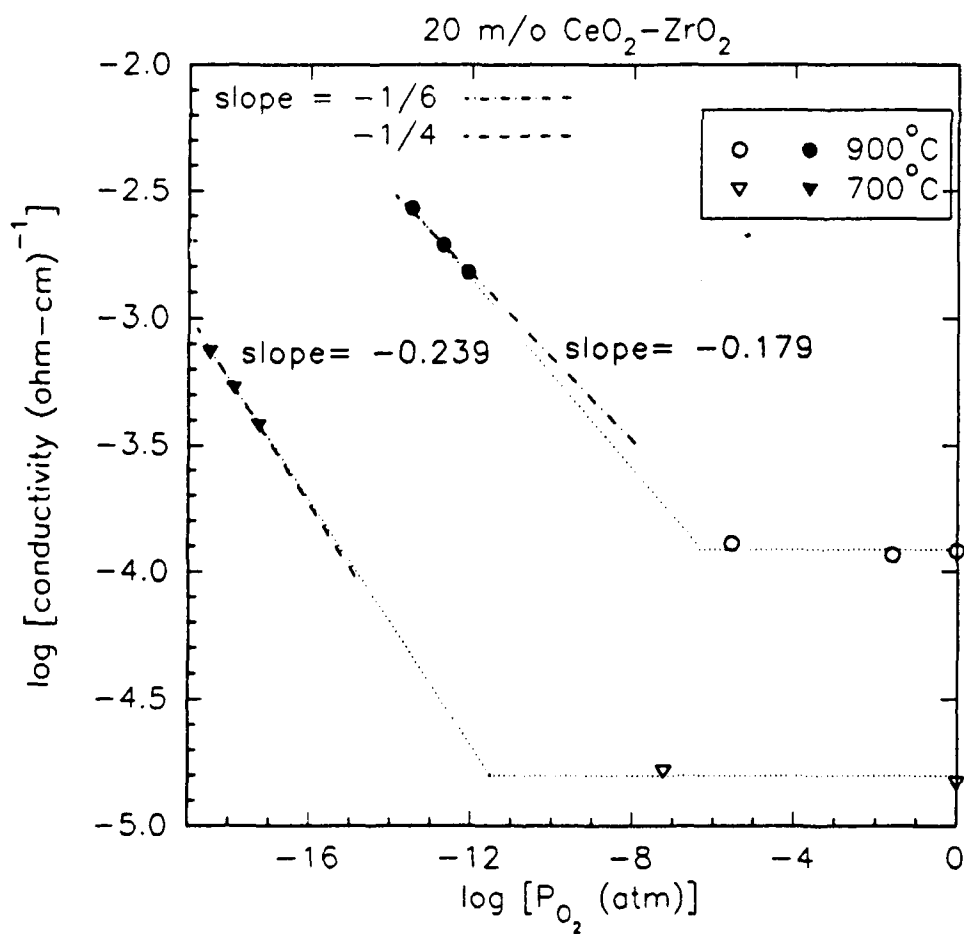
Figure 21 Electrical conductivity as a function of oxygen partial pressure for 20 mole percent CeO_2-ZrO_2.

slopes at all experimental temperatures were quite close to -1/6 which Casselton (14) proposed as evidence of cerium ion reduction. The oxygen independent domain may be indicative of oxygen vacancy conduction.

Although the same two distinct oxygen dependencies appeared in Figure 20, the 15m/o ceria material displayed different slopes in the n-type region. Unlike the previous case where the slope standard deviations were less than five percent, the slopes in Figure 20 were not as definitive: -0.202 ± 0.065 and -0.113 ± 0.044 at 700 and 900°C, respectively. However, these values were within their standard deviations of a -1/6 slope. While these measurements were reproducible, time constraints prevented further experiments at neighboring oxygen activities.

In Figure 21, the 20 mole percent ceria specimen also evidences two regions of oxygen dependence; however, the slopes are not close to -1/6. Further, the slope standard deviations are less than one percent which precludes any loose fit to that paradigm. At 700°C, the departure from anticipated behavior is too large to be the result of experimental errors; therefore, three possible conclusions exist:

1) Another oxygen dependent mechanism occurs singularly or in combination with the Casselton model (e.g., univalent cerium interstitials).

2) Electrons become trapped by oxygen vacancies forming F^+ centers, and, as temperature increases, electrons escape from these potential wells.

3) Ce^{3+} ions form associates with oxygen vacancies. This can be described using a modification of the Casselton model. Instead of

$$2Ce_{Zr}{}^{x} + O_{O}{}^{x} = 2Ce_{Zr}{}' + V_{O}{}^{\bullet\bullet} + 1/2O_{2}(g) \qquad 3)$$
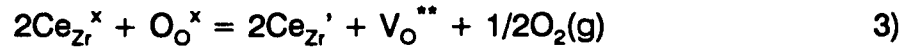
where

$$\log \sigma \propto -1/6 \log P_{O2}, \qquad 4)$$

the association of reduced ions and vacancies can be written as

$$2Ce_{Zr}{}^{x} + O_{O}{}^{x} = Ce_{Zr}{}' + (Ce_{Zr}{}'V_{O}{}^{\bullet\bullet})^{\bullet} + 1/2O_{2}(g). \qquad 5)$$

Using the equilibrium constant, K,

$$K = [Ce_{Zr}{}'][(Ce_{Zr}{}'V_{O}{}^{\bullet\bullet})^{\bullet}] P_{O2}{}^{1/2} \qquad 6)$$

the electroneutrality condition,

$$[Ce_{Zr}{}'] = [(CeZr'VO^{\bullet\bullet})^{\bullet}], \qquad 7)$$

and the manipulations found in section 2.2.3,

$$[Ce_{Zr}{}'] \propto P_{O2}{}^{-1/4}. \qquad 8)$$

At 900°C, a slope of -0.1793 ± .0004 suggests that reduced cerium ions generated in equation 1) are the dominant contributors to conduction and one of the aforementioned mechanisms plays a lesser role.

A reasonable explanation for this deviation from the Casselton model must resolve three questions from experimental results:

1) Why do the slopes deviate from -1/6?

2) Why does this effect occur at increasing ceria contents?

3) Why do the slopes increase as a function of temperature?

Kofstad and Hed (15) have proposed that univalent cerium interstitial ions

significantly affected conductivity and calculated an oxygen dependence slope

of -1/2. If such a species did exist, the concentration of interstitial ions would

increase as a function of ceria content. However, as temperature increased,

one would expect a greater interstitial contribution due to enhanced mobility;

consequently, the slope would not increase at higher temperatures. In addition,

the ionic radius of the cerium interstitial (1.20 Å) may prevent any significant

contribution to conduction due to its low mobility.(14)

The reduction of cerium 4+ ions creates oxygen vacancies and cerium

3+ ions.

$$2Ce_{Zr}^x + O_O^x = 2Ce_{Zr}' + V_O^{\bullet\bullet} \ 1/2O_2 \qquad\qquad 3)$$
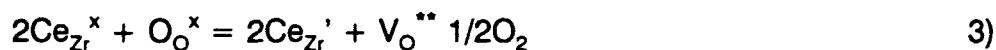
Under reducing conditions, as cerium concentrations increase, the production

of reduced cerium ions and, correspondingly, oxygen vacancies increases.

Since the formation of F^+ centers depends directly on the concentration of

oxygen vacancies, the number of trapped electrons is a function of the ceria

content. The capture of electrons by oxygen vacancies depletes the number of

hopping electrons and, consequently, changes the oxygen dependence of the

electrical conductivity. As temperature increases, more electrons have sufficient

energy to escape these potential wells, thus, lessening the impact of F^+ centers

on conductivity. The generation of F^+ centers answers all three concerns, but

the absorption energy of a F^+ or F center in zirconia is quite high (2.5-3.0

eV).(16) The activation energy for these electrons to escape these potential

wells would be unusually large.

The creation of Ce^{3+} ion-oxygen vacancy associates is the most sound

explanation i... ...he experimental observations. Equations 5-8 predict a -1/4

slope which closely matches the -0.239 value at 700°C. The generation of

associated defects are a direct function of ceria concentration at a single

temperature. As temperature increases, the associates dissociate thus

decreasing the slope in the n-type region. This prediction corresponds to the

reduction of the slope from -0.239 to -0.179 as temperature increased from 700

to 900°C. Similar association behavior has been observed in the calcia- (17)

and yttria-stabilized (18) zirconia systems. This model may also describe the

erratic behavior in the 15m/o ceria sample, but further experiments with

intermediate compositions are required to confirm this case.

Additional evidence supporting a modified Casselton model lies in the

threshold P_{O2} for n-type behavior. As the ceria content increased, the oxygen

partial pressure at the P_{O2}-independent-n-type transition decreased. At a

constant oxygen potential, greater cerium concentrations generate more

reduced cerium ions, and concomitantly, more electrons. Therefore, the

electronic conductivity exceeds the P_{O2}-independent charge carrier conductivity

at a lower oxygen activity for a larger ceria mole fraction.

In Figures 19-21, a large region exists where conductivity is independent

of oxygen activity. Further, the conductivities in these regions are

approximately the same for all three compositions; consequently, the dominant

defect is not a function of dopant concentration. Therefore, the principal

44

charge carrier must be unaffected by oxygen activity and dopant concentration.

The defect equations of pure and ceria-stabilized zirconia are written as:

$$ZrO_2 = Zr_{Zr}^x + 2V_O^{\bullet\bullet} + 2O_i''\qquad 9)$$

$$CeO_2 = Ce_{Zr}^x + 2V_O^{\bullet\bullet} + 2O_i''\qquad 10)$$

where the addition of ceria does not contribute any additional charge species

and the defect equation is not dependent on oxygen partial pressure. Since

oxygen interstitials are the less mobile entity, oxygen vacancies dominate

conduction in the low oxygen activity region.

Electrical Conductivity as a Function of Temperature

Electrical conductivity is often measured as a function of temperature to

detect changes in physical or chemical structure. Such alterations can be

manifested in unusual cyclic behavior or abrupt changes in slope. For

example, non-linear cyclic behavior may suggest a phase transformation which

does not occur at the same temperature during heating as cooling. The slope

of the log conductivity as a function of temperature can be used to calculate

the activation energy of the conducting species.[+]

In the preceding section, two conduction mechanisms have been

---

[+] The rigorous form of the equation is :

$$\sigma = \sigma_o/T \,{}^*e^{-\Delta E/kT}$$

where σ is the conductivity, σ_o is absolute conductivity (constant), k is the Boltzmann constant, T is the temperature (K) and ΔE is the activation energy; however, the simplified equation

$$\sigma = \sigma_o{}^*e^{-\Delta E/kT}$$

is more commonly used.

proposed for ceria-stabilized zirconia: oxygen vacancy motion and electron hopping via cerium ions (or $(Ce_{Zr}'V_O^{\bullet\bullet})^{\bullet}$ associates). Conductivity as a function of temperature measurements have been performed to characterize the activation energies of these conduction modes and to determine the causes of unusual thermal expansion behavior cited by Duwez and Odell.(19)

Figures 22-24 describe the thermal cycling results for 12, 15, and 20 mole percent ceria. Two salient points should be noted about the cyclic behavior of the 12 and 15m/o samples. First, the conductivities during the initial heating cycles are lower than the subsequent heating cycle values while the cooling curve conductivities are reproducible over two cycles. Secondly, the conductivity curves during heating and cooling do not match. This hysteresis-like behavior is reproducible over two cycles. This phenomenon may suggest ordering and disordering of the oxygen vacancies (the presence of an ordered phase) or a repeating monoclinic-tetragonal transformation. In contrast to this aberrant behavior, the 20m/o CeO_2-ZrO_2 curve (Figure 24) contains a single slope through two heating and cooling cycles. This decidedly regular behavior suggests that no structural changes occur for this composition within this temperature range. Using thermal expansion experiments, Duwez and Odell have described similar behavior although only compositions below 15 mole percent ceria have evidenced non-linear thermal expansion curves. These authors concluded that a monoclinic-tetragonal transformation caused this effect. High temperature x-ray diffraction measurements test this conclusion.
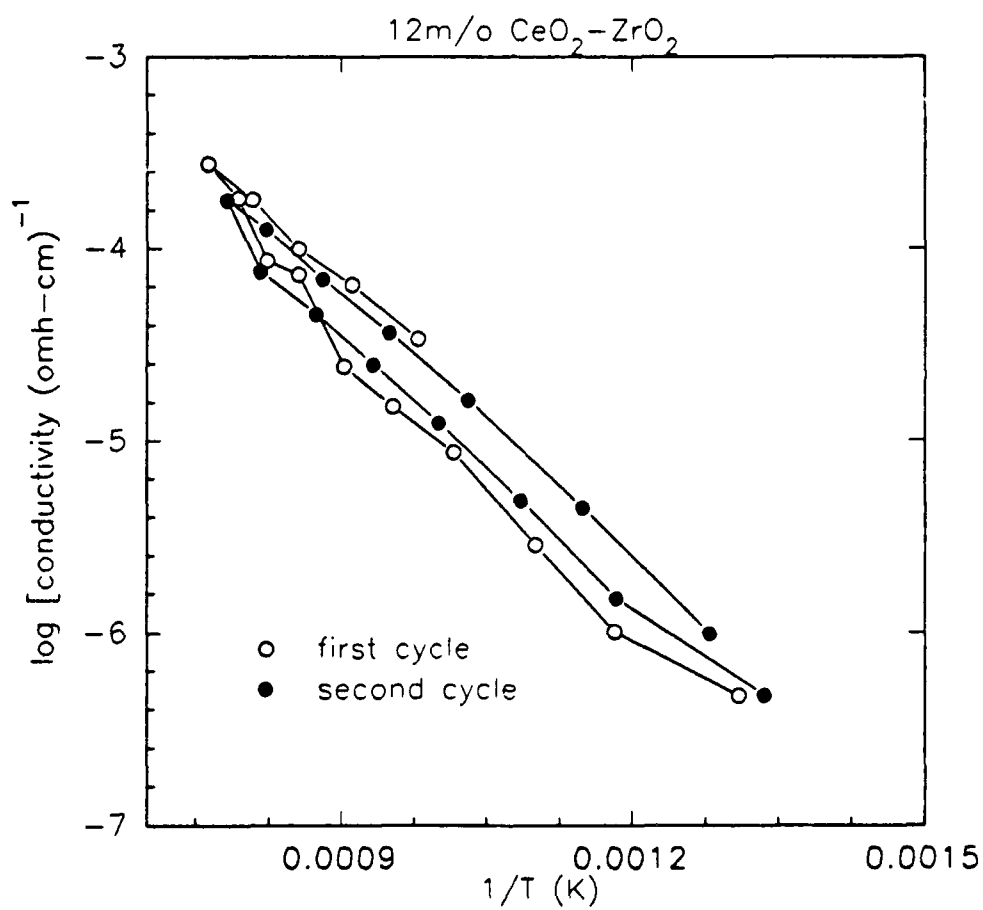
46

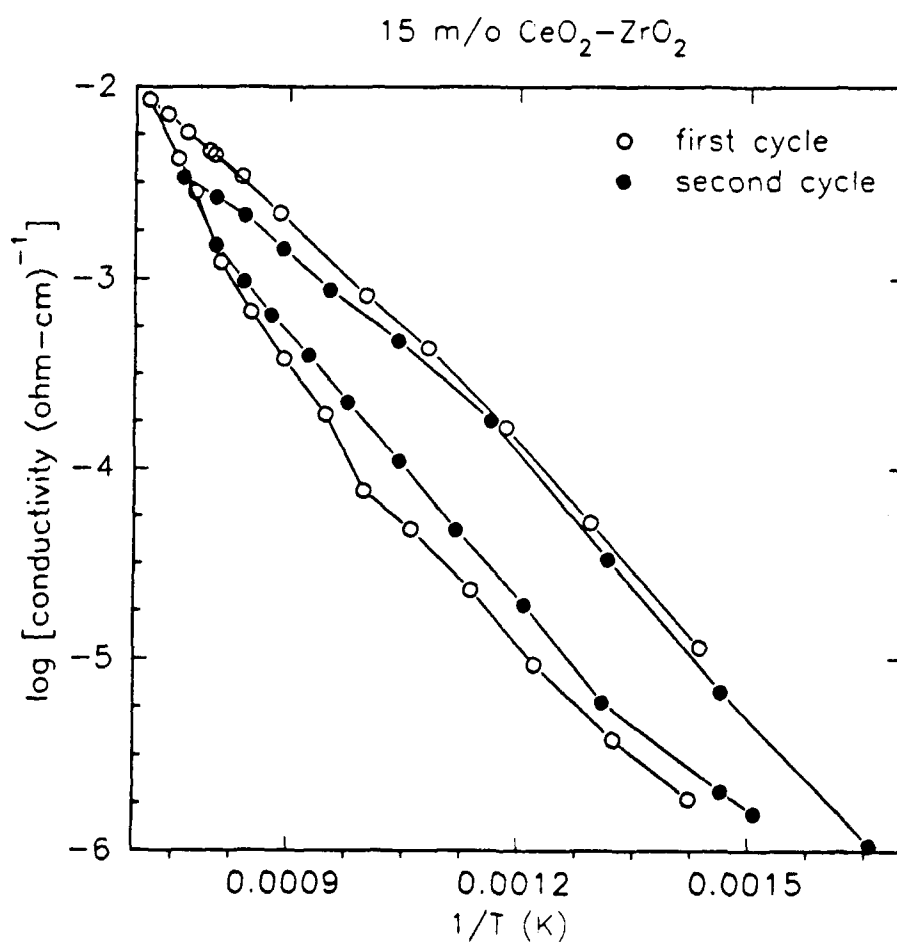Figure 22 Conductivity of 12m/o CeO$_2$-ZrO$_2$ as a function of temperature for two heating and cooling cycles.

47

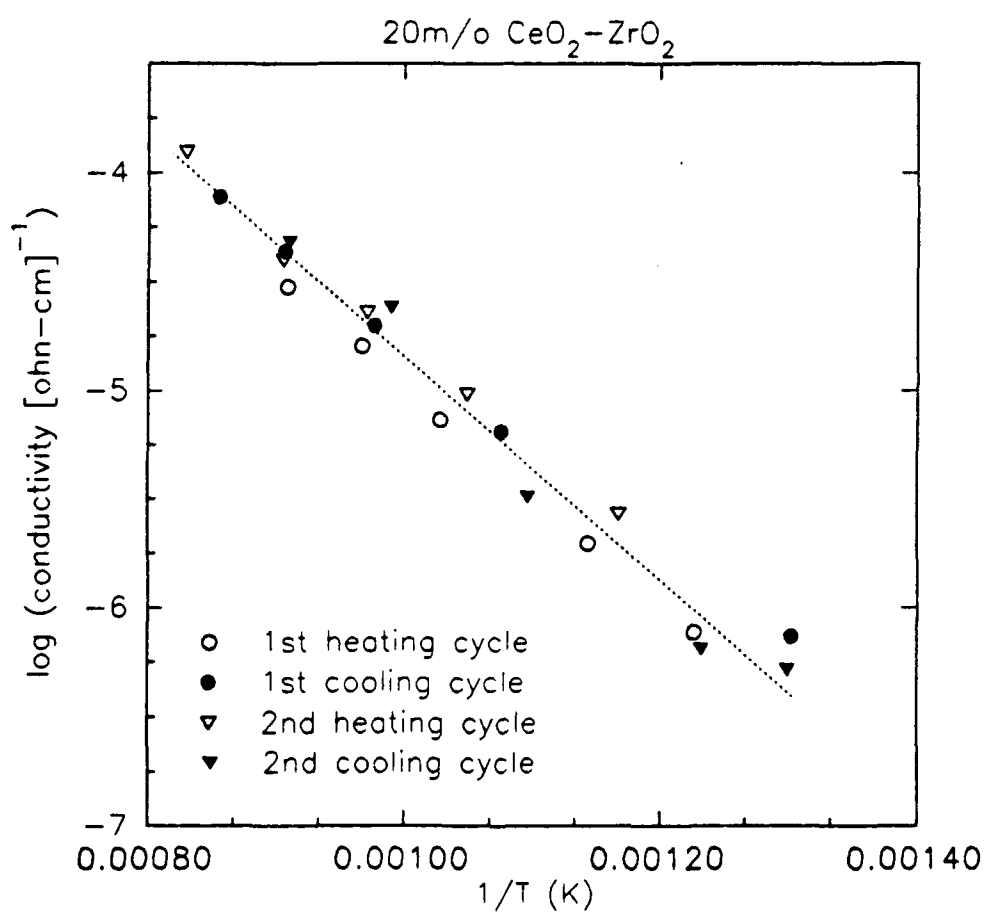Figure 23 Conductivity of 15m/o CeO$_2$-ZrO$_2$ as a function of temperature for two heating and cooling cycles.

48

Figure 24 Conductivity of 20m/o CeO_2-ZrO_2 as a function of temperature for two heating and cooling cycles.

To elucidate the mechanisms which are responsible for the oxygen independent and n-type regions in Figure 19-21, electrical conductivity has been measured as a function of temperature at $P_{O_2}= 0.21$ atm and $3x10^{-14}$atm. The slopes of these curves have been used to calculate the conduction activation energies. Because the assignment of slopes to curve segments can be contentious, an exacting effort has been made to discriminate between experimental fluctuations and genuine changes in slope by comparing the correlation coefficients of the proposed line divisions.

Figures 25-27 illustrate the effect of temperature on the conduction activation energies. A summary of these results is given in Table 2. In air, all three sample compositions evidence single activation energies for the entire temperature range. Further, these values increase slightly as function of ceria content. These results are consistent with the activation energies for oxygen vacancy conduction in yttria-stabilized zirconia (20). Consequently, these data support the analysis in an earlier section which contends that anti-Frenkel behavior dominates the oxygen independent region in Figures 19-21.

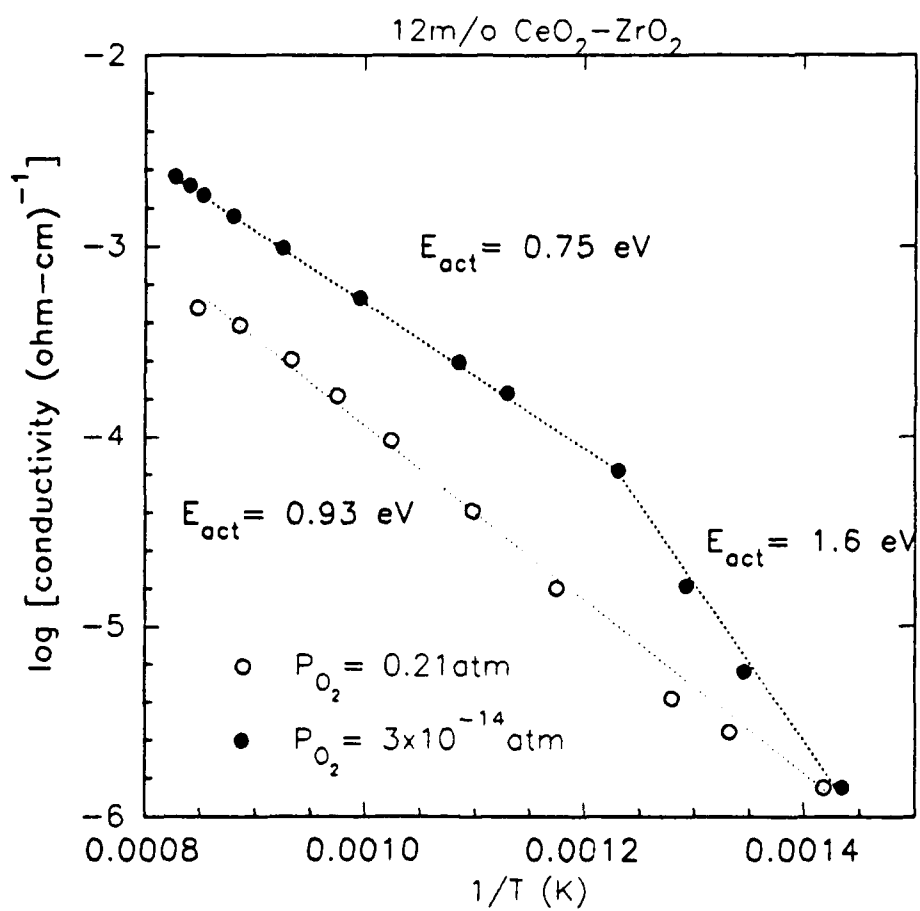Figure 25 Electrical conductivity versus temperature for 12m/o CeO_2-ZrO_2 at two oxygen partial pressures.

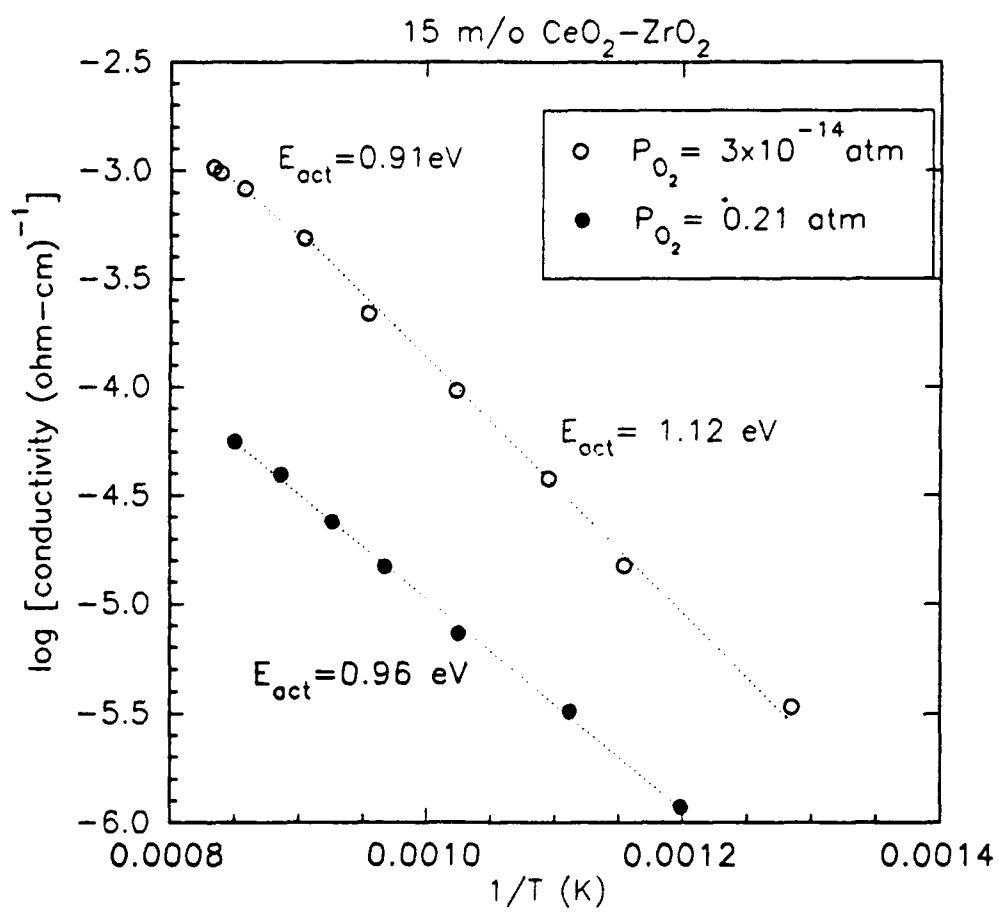Figure 26 Electrical conductivity versus temperature for 15m/o CeO_2-ZrO_2 at two oxygen partial pressures.
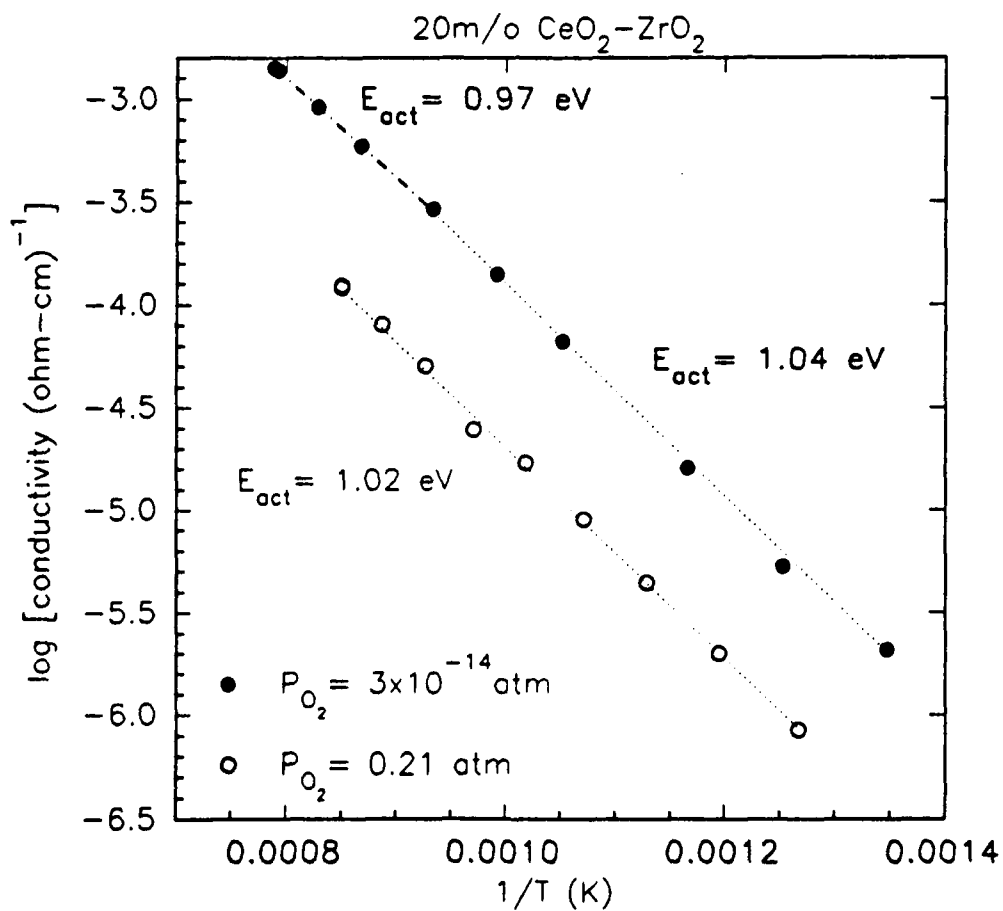
Figure 27 Electrical conductivity versus temperature for 20m/o CeO$_2$-ZrO$_2$ at two oxygen partial pressures.

Table 2 A summary of the activation energies calculate from Figures 25-27.

mole % CeO_2	E_{act} (eV) P_{O2} =0.21 atm	Temperature Range (°C)	E_{act} (eV) P_{O2} =3x10^{-14} atm	Temperature Range (°C)
12	0.93 ± 0.02	440-900	1.60 ± 0.10	440-525
12			0.75 ± 0.01	525-900
15	0.96 ± 0.01	560-900	1.12 ± 0.03	500-838
15			0.91 ± 0.01	838-900
20	1.02 ± 0.01	550-900	1.04 ± 0.02	470-798
20			0.97 ± 0.01	798-1000

At P_{O2}= 3x10^{-14} atm, each composition exhibits two activation energies. At 700°C, the E_{act} of 12 mole percent ceria is 0.75 ± 0.01 eV. For the same temperature (Table 2), the 15 and 20m/o samples have activation energies of 1.12 and 1.04 eV, respectively. This difference (between 0.75 eV and, 1.02 and 1.12 eV) of about 0.3 eV corresponds remarkably well with association energies calculated by Cormack and Catlow for dopant-vacancy pairs in tetragonal zirconia.(21) Although these calculations used yttrium, galodinium, and lanthanum as dopants, their ionic radii and valence compare well with the Ce^{3+} ion. These greater activation energies in 15 and 20m/o ceria suggest the

formation of reduced cerium ion-oxygen vacancy associates. At about 800°C,

the activation energies of the 15 and 20m/o samples decrease to 0.91 and

0.97eV, respectively. These changes correspond to the predicted dissociation

of the reduced ion-vacancy associates. The electrical conductivity-temperature

results provide additional evidence for the modified Casselton model.

Ionic Transport Number Measurements

Electronic contributions to electrical conductivity in ceria-stabilized

zirconia are not clearly defined in the literature. The nature of potentiostatic

polarization measurements is responsible for much of the difficulty in

ascertaining electronic contributions. The basic experimental procedure places

a sample between two oxygen partial pressures and measures the subsequent

voltage. This potential gradient forces the sample to equilibrate at each end. If

the material is an ionic conductor, then the resulting electrical potential relates

directly to the chemical potential difference. However, if electronic species

contribute significantly to conduction ($t_{electronic} > 0.001^+$), then the measured

potential will not equal the calculated value. The ionic fraction of the total

conductivity (ionic transport number) is the ratio of the measured and

calculated potentials.

Difficulties arise from the electrical potential measurement and the

---

$^+$ The sum of the transport numbers equals unity,
$t_{ionic} + t_{electronic} = 1$.

55

selection of the measurement temperature. Magnetic and electrical fields

generated from neighboring equipment must be considered in the experimental

design. To eliminate these fields, the measurement cells and apparatus must

be shielded and grounded. The measurement temperature should be

consistent with reasonable diffusion rates, so that stable and reproducible

measurements can be obtained. Low measurement temperatures are often

impractical.

The preceding caveats account for the literature inconsistencies

concerning the relative ionic and electronic contributions in ceria-stabilized

zirconia. Since Ni/NiO and Cu/Cu$_2$O couples were used in this study to set

oxygen activities, the resulting P$_{O2}$'s were a function of temperature. The

oxygen activities for these couples was calculated as a function of temperature

(Figure 28). The experimental temperatures were maintained above 800°C in

order to generate oxygen partial pressures greater than the incipient P$_{O2}$ in the

nitrogen carrier gas and to insure rapid equilibration.

In Figures 29-31, the ionic transport numbers are plotted as a function of

temperature. Although the oxygen activities are constant only for a given

temperature, these figures describe trends and specific t$_{ionic}$ values which aid in

the characterization of the n-type and ionic conduction regions. In Figure 4.29,

the 12 mole percent sample displays unexpected behavior-- the ionic transport

number increases as a function of temperature. However, a closer examination

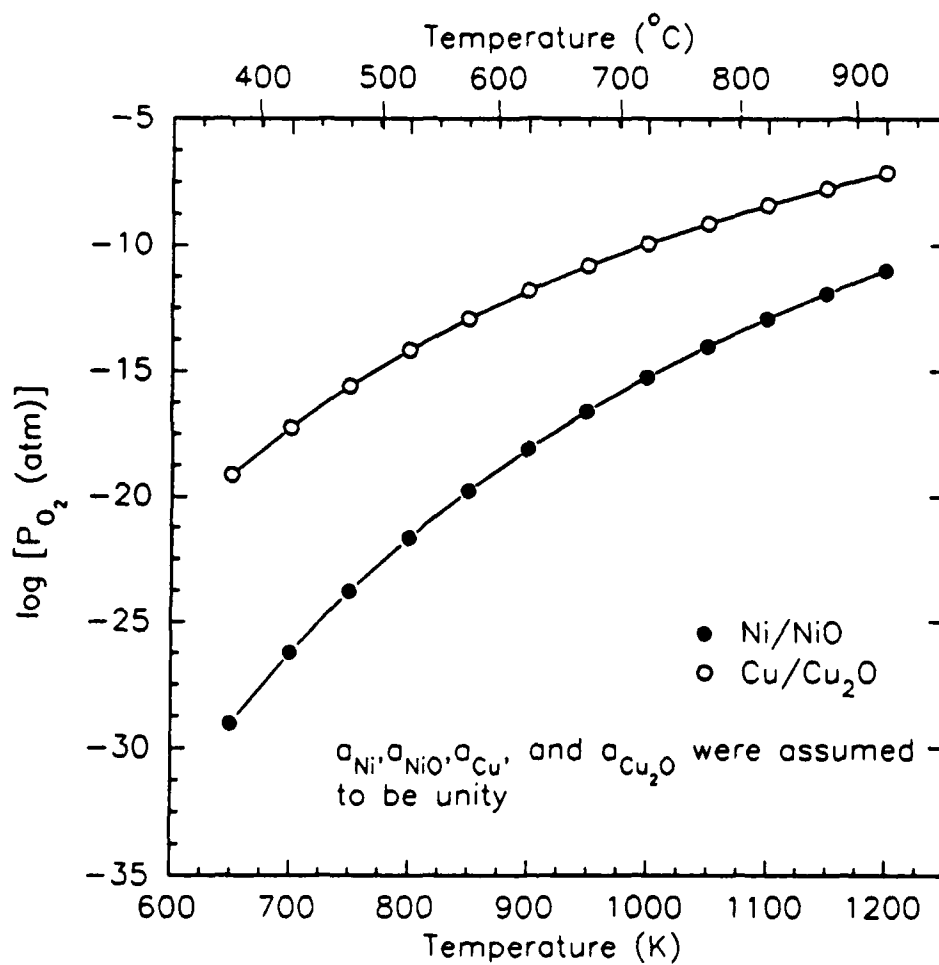of the data in Figures 28, 29, and 19 suggests that the experimental oxygen

Figure 28 Oxygen activity as a function of temperature for Cu/Cu₂O and Ni/NiO couples used the ionic transport number measurements.

partial pressures occur in an ionic-electronic transition region: in Figure 19, the 900°C threshold P_{O_2} is approximately 10^{-9}atm, and in Figure 29, the partial pressure range at 900°C is 3.4×10^{-8}- 3.2×10^{-12}atm. Within this range, the ionic transport number is 0.078.

Figure 30 describes the ionic conduction behavior of 15 mole percent ceria as a function of temperature. At 900°C, the electronic contribution is approximately 98%. This datum corresponds to the n-type behavior in Figure 20 at the same temperature and oxygen partial pressure. At 800°C, electronic species are less dominant, conducting only 80% of the charge.

The 20m/o CeO_2-ZrO_2 material behaves similarly to the 15m/o sample. Figure 31 shows a decrease in ionic contribution from about 9% at 800° to 4% at 900°C. A 96% electronic contribution at 910°C and a P_{O_2} range of 4×10^{-8}- 5×10^{-8} atm (Figure 28) corresponds to the n-type behavior found in Figure 21.

The ionic conductivity results support the model proposed earlier. Amid an electronic-ionic transition region, the 12m/o sample shows an increase in the t_{ionic} as temperature increases. In the n-type conduction realm, 15 and 20m/o specimens display an increasing electronic contribution as a function of temperature.
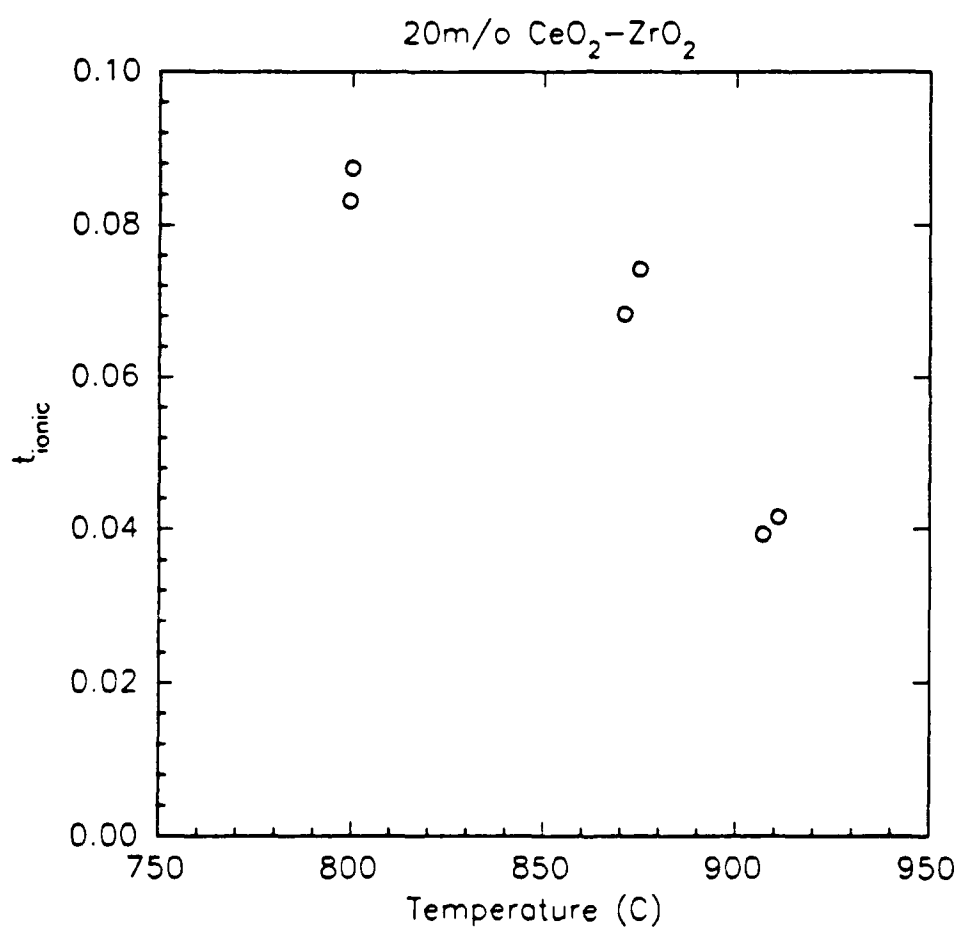
Figure 29 Ionic transport number as a function of temperature for 12m/o CeO$_2$-ZrO$_2$.
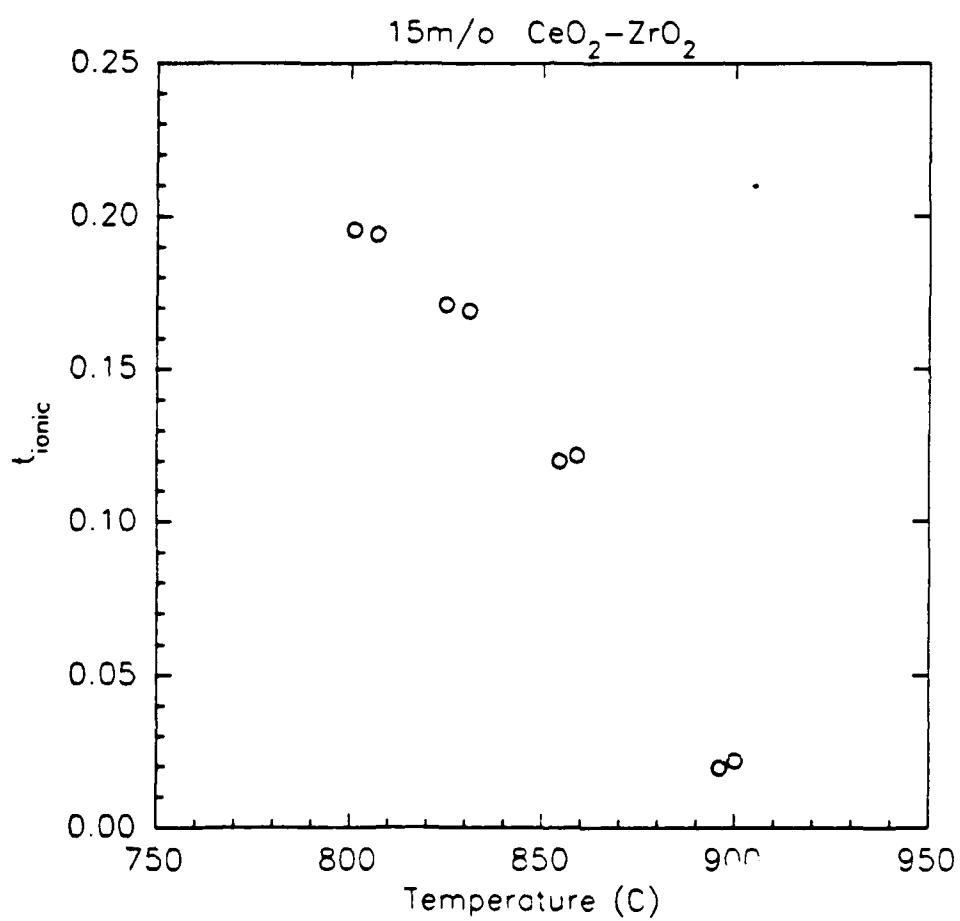
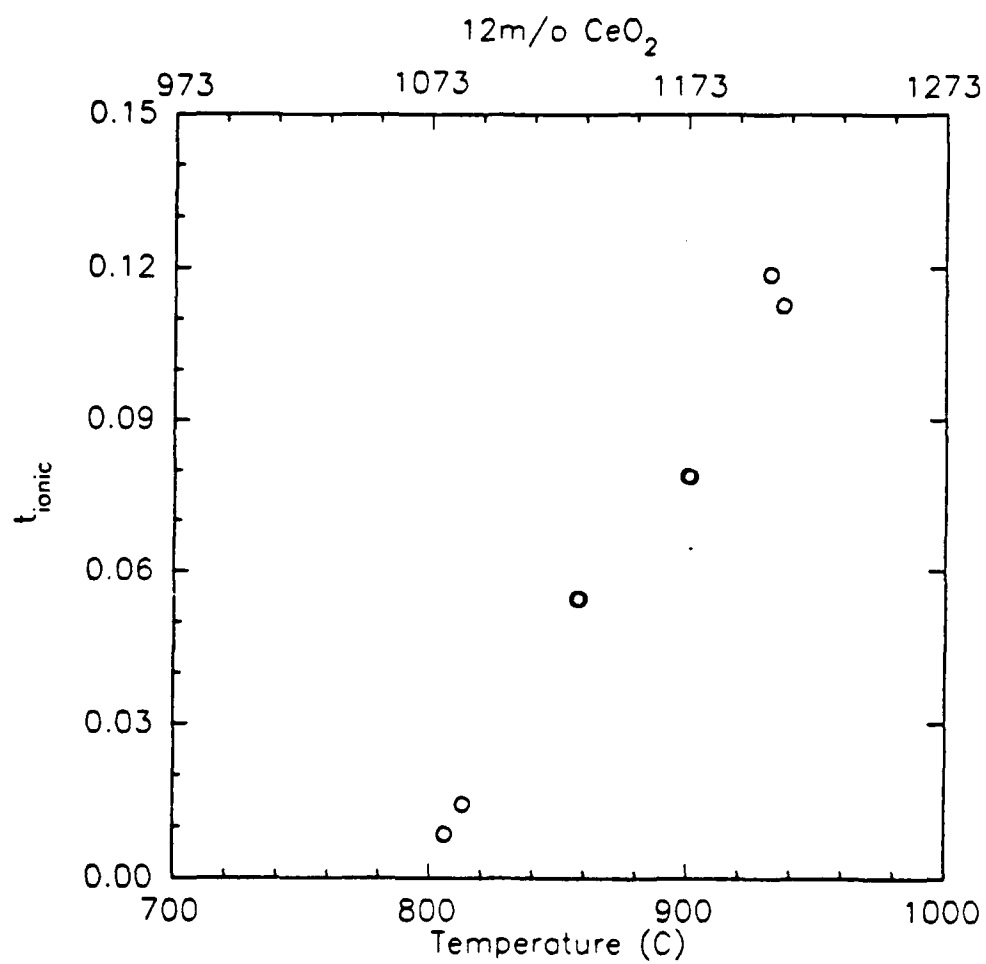Figure 30 Ionic transport number as a function of temperature for
15m/o CeO_2-ZrO_2.

Figure 31 Ionic transport number as a function of temperature for 20m/o CeO_2-ZrO_2.

61

High Temperature X-ray Diffraction Experiments

The literature is awash in controversy over the low temperature phase

behavior in the zirconia-ceria system. In summary, three different interpretations

of the zirconia-rich region exist:

1) Duwez and Odell suggest a tetragonal phase region (12-18 mole%

ceria) and a cubic and tetragonal phase field (18-90% ceria).(19)

2) Tani and coworkers propose that the equilibrium phases below

1000°C are monoclinic and cubic for almost the entire breadth of the

phase diagram.(22)

3) Duran et al. submit that the tetragonal phase is stable well below

1000°C up to 18% CeO_2 and that an ordered compound, $Ce_2Zr_3O_{10}$, exists at

room temperature.(23) It is not the design of this research to resolve this

debate; however, it is critical to be cognizant of these differing phase diagrams.

The signature patterns and diffraction information for the three stable

polymorphs of pure zirconia (monoclinic, tetragonal, and cubic), 16 mole

percent CeO_2-ZrO_2, and $Ce_2Zr_3O_{10}$ are detailed in Figures 31-32. These data

are powder diffraction spectra using CuK_α radiation. Recognition of a few

salient features is required for an effective phase determination. The monoclinic

phase which is represented in Figure 31a has two large peaks at 28.18 and

31.49°. No other zirconia-based phase has any significant reflections at these

angles. The pure and ceria-stabilized tetragonal patterns (Figure 32b and c)

are characterized by a very large peak slightly less than 30° and moderately

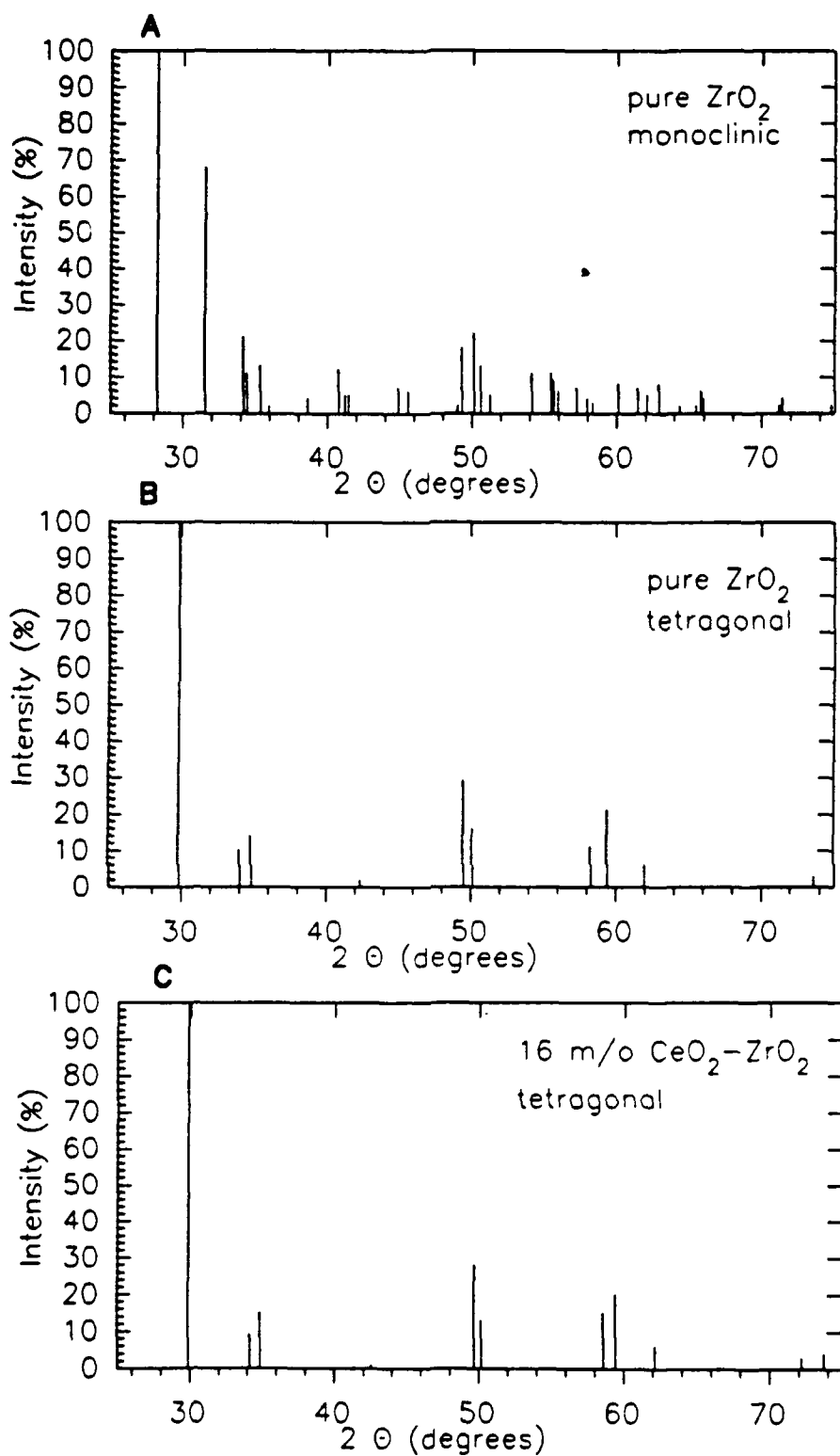Figure 32 Standard x-ray diffraction patterns for (a) monoclinic (24), (b) pure tetragonal ZrO_2 (25), and (c) 16m/o CeO_2-ZrO_2 (26).

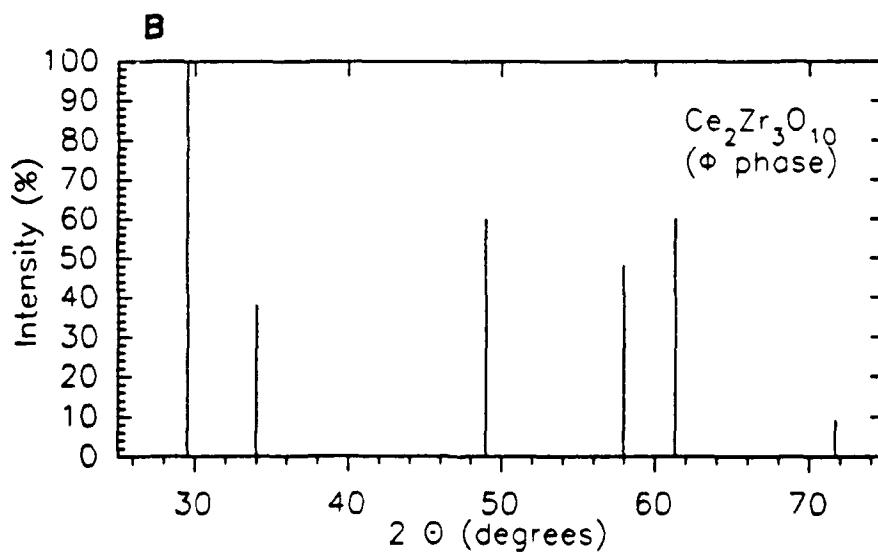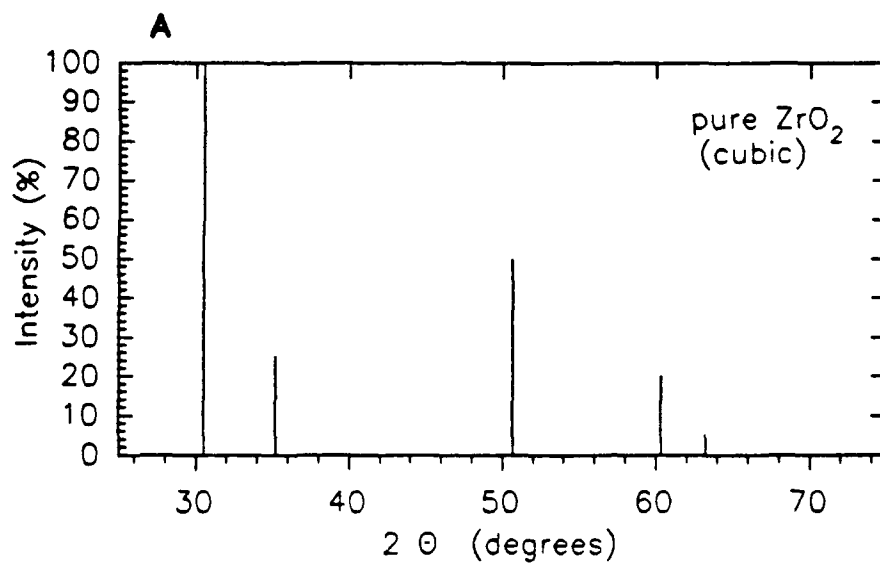Figure 33 Standard x-ray diffraction patterns for (a) cubic pure ZrO_2 (27) and (b) $Ce_2Zr_3O_{10}$ (28).

large peak pairs located near 35, 50, and 59°. The cubic pattern is distinguished by a dominant reflection at 30.51° and three major peaks at angles slightly greater than 35, 50, and 60 degrees. Recognition of the ϕ phase can be quite troublesome hence the debate regarding its existence. When comparing Figures 32c and 33b, the cause for this difficulty is quite clear- - all of the major peaks of the tetragonal and ϕ phases almost exactly coincide. If $Ce_2Zr_3O_{10}$ is a low temperature equilibrium phase, only careful experimentation could lead to definitive identification.

Phase Identification of Powders and Sample Pellets

In order to discern the phase composition of the sample powders, diffraction patterns have been obtained for 12, 15, and 20 m/o $CeO-ZrO_2$ compositions. These spectra are found in Figure 34. Upon inspection, the 12 mole percent specimen contains both monoclinic and tetragonal phases. Using a method first proposed by Toraya et al. (29) which compares the intensities of the $(\underline{1}11)_m$ and $(111)_m$ reflections with the $(101)_t$, the 12m/o samples have been determined to contain 40 ± 1.5 weight percent monoclinic phase. The 15 and 20 mole percent compositions are comprised of only the tetragonal phase.

These powders were pressed into thin pellets and sintered at 1550°C for three hours. The diffraction patterns from these samples are described in Figure 35. The 12 mole percent pellet was composed of 80 ± 2.0 weight percent monoclinic and 20 percent tetragonal species. The 15 and 20m/o
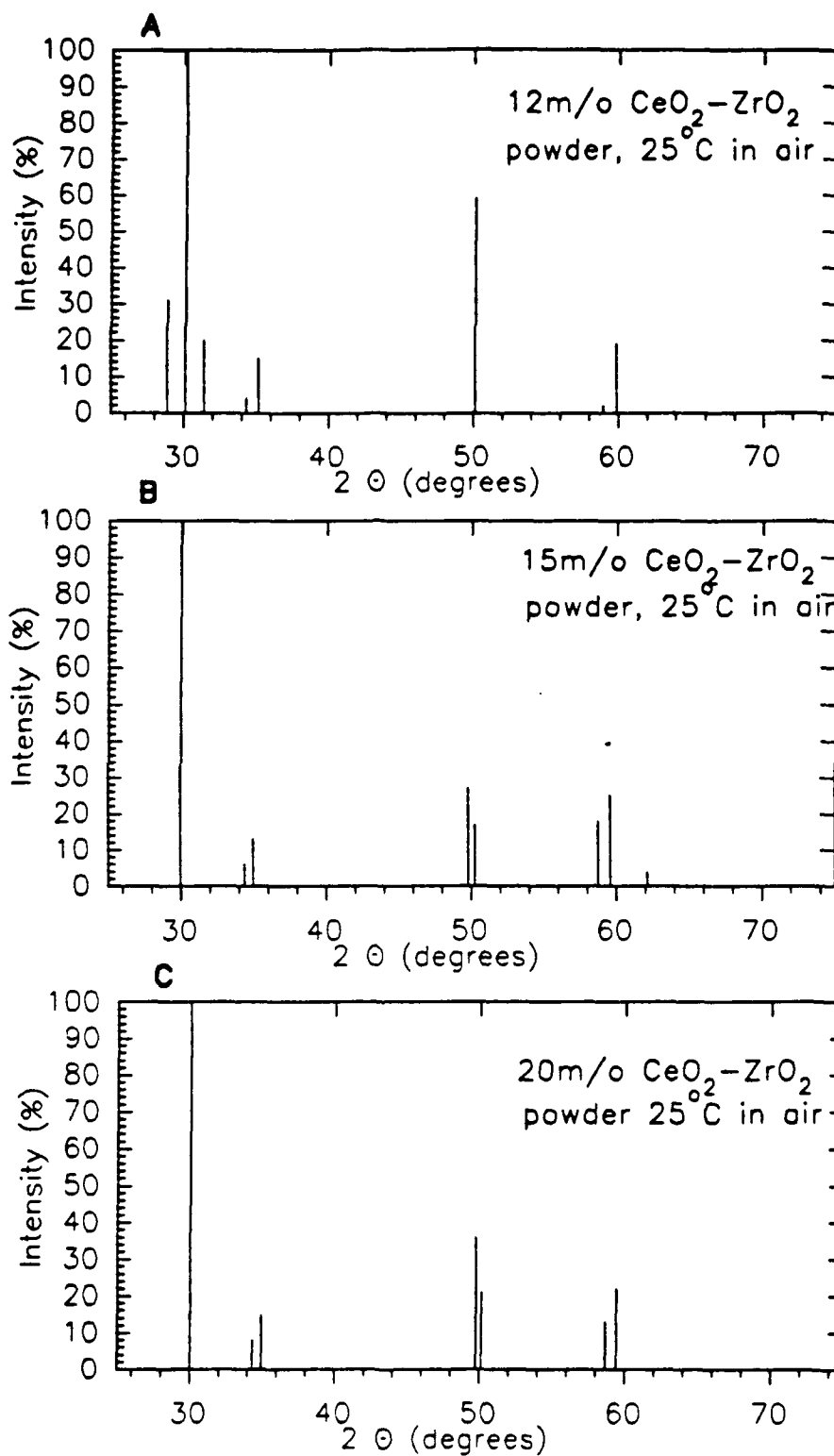
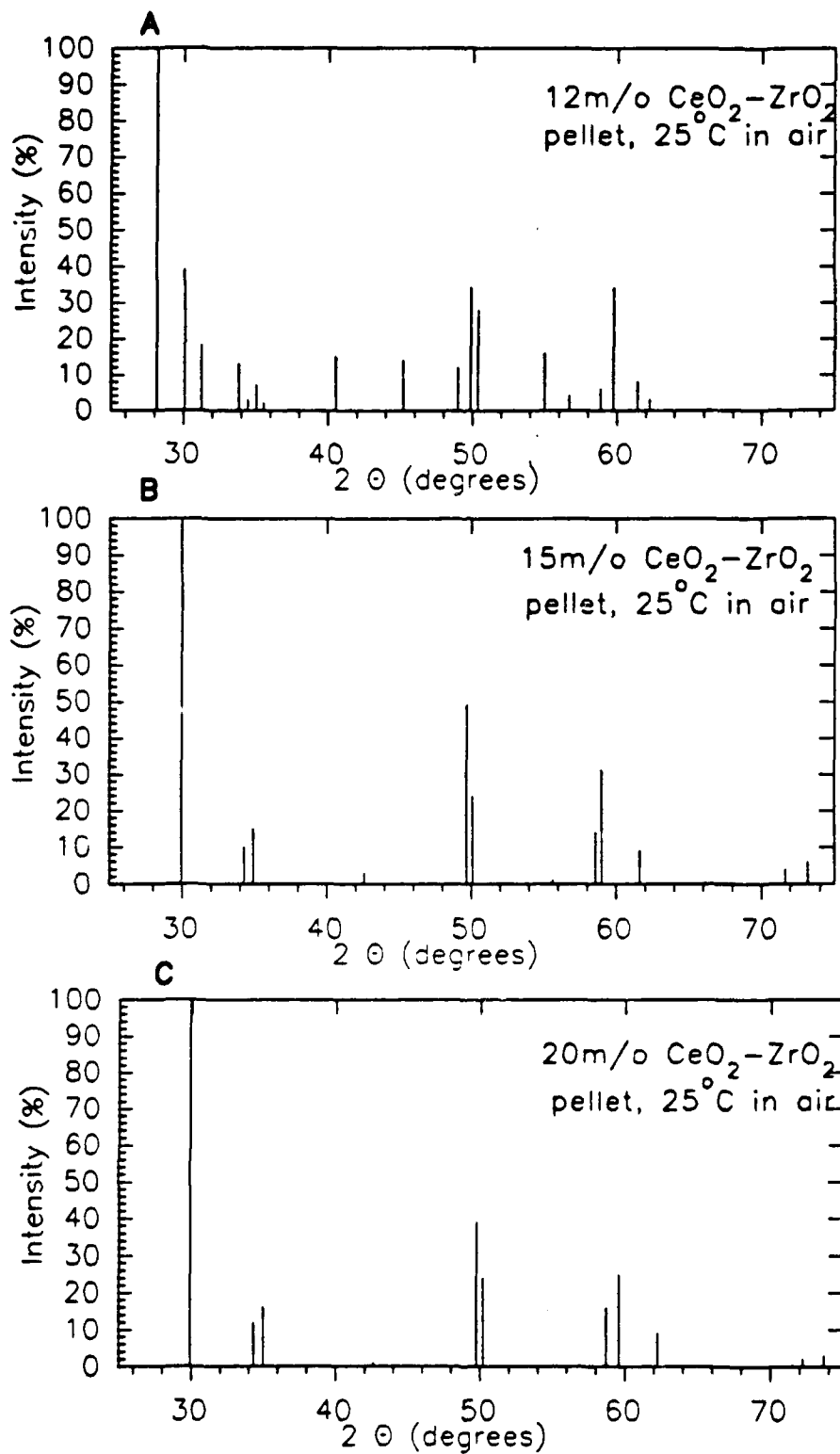Figure 34 X-ray diffraction results for (a) 12, (b) 15, and (c) 20m/o ceria-zirconia powders.

Figure 35 X-ray diffraction results for the (a) 12, (b) 15, and (c) 20m/o CeO₂-ZrO₂ sample pellets.

specimens displayed only tetragonal reflection patterns.

High Temperature X-ray Diffraction in Air

Previously, the electrical conductivity measurements displayed some anomalies at elevated temperatures. Specifically, the hysteresis-like behavior of 12 and 15 mole percent ceria suggested either a phase transformation or the existence of an ordered phase (e.g., the ϕ compound proposed by Duran and others). *In situ* high temperature x-ray diffraction can monitor changes in crystal structure and may explain the causes for this behavior.

Prior to heating, the 12m/o sintered pellet contained 80% monoclinic phase. At 735°C, there is no evidence of the signature $(\underline{1}11)_m$ peak; however, there are several reflections which are not tetragonal (2θ = 31, 35, 39, 45, and 67°).(Figure 36) This pattern persists at 900°C, and the 31, 35, and 39° 2θ peak intensities increase. When the sample cools, the intensities diminish, but do not disappear. At room temperature, seven unidentifiable peaks remain. These reflections do not match any pattern from a zirconia polymorph or an ordered phase. From thermal expansion data, other research efforts have proposed that a monoclinic-tetragonal transformation causes the anomalous electrical behavior; these results suggest that no monoclinic phase exists above 735°C.

Before the experiment, the sintered 15 mole percent sample was comprised entirely of tetragonal phase. While Figure 39 differs marginally from Figure 36, the 12m/o pattern exhibits three peaks at 65, 67, and 68°
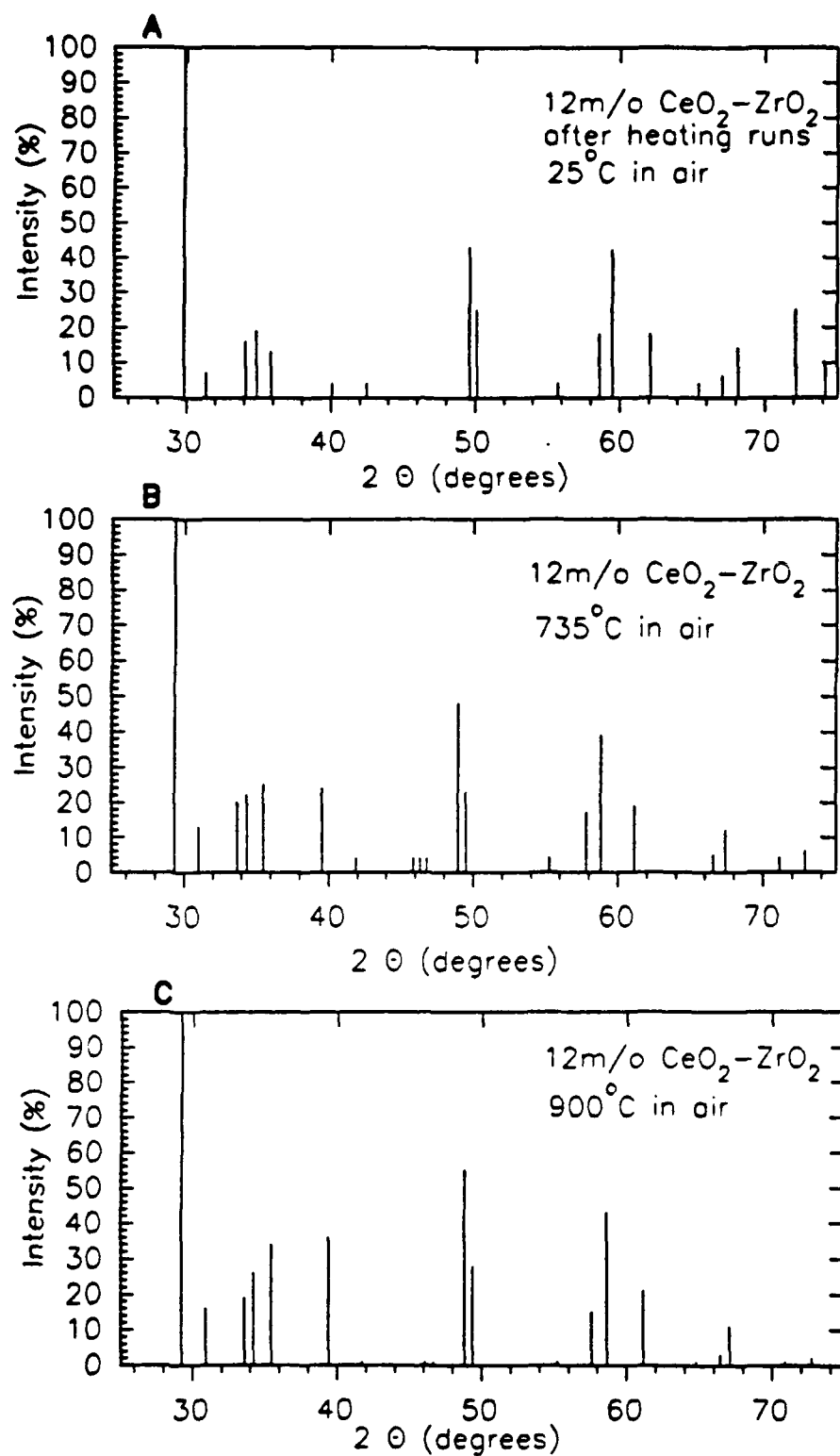
68

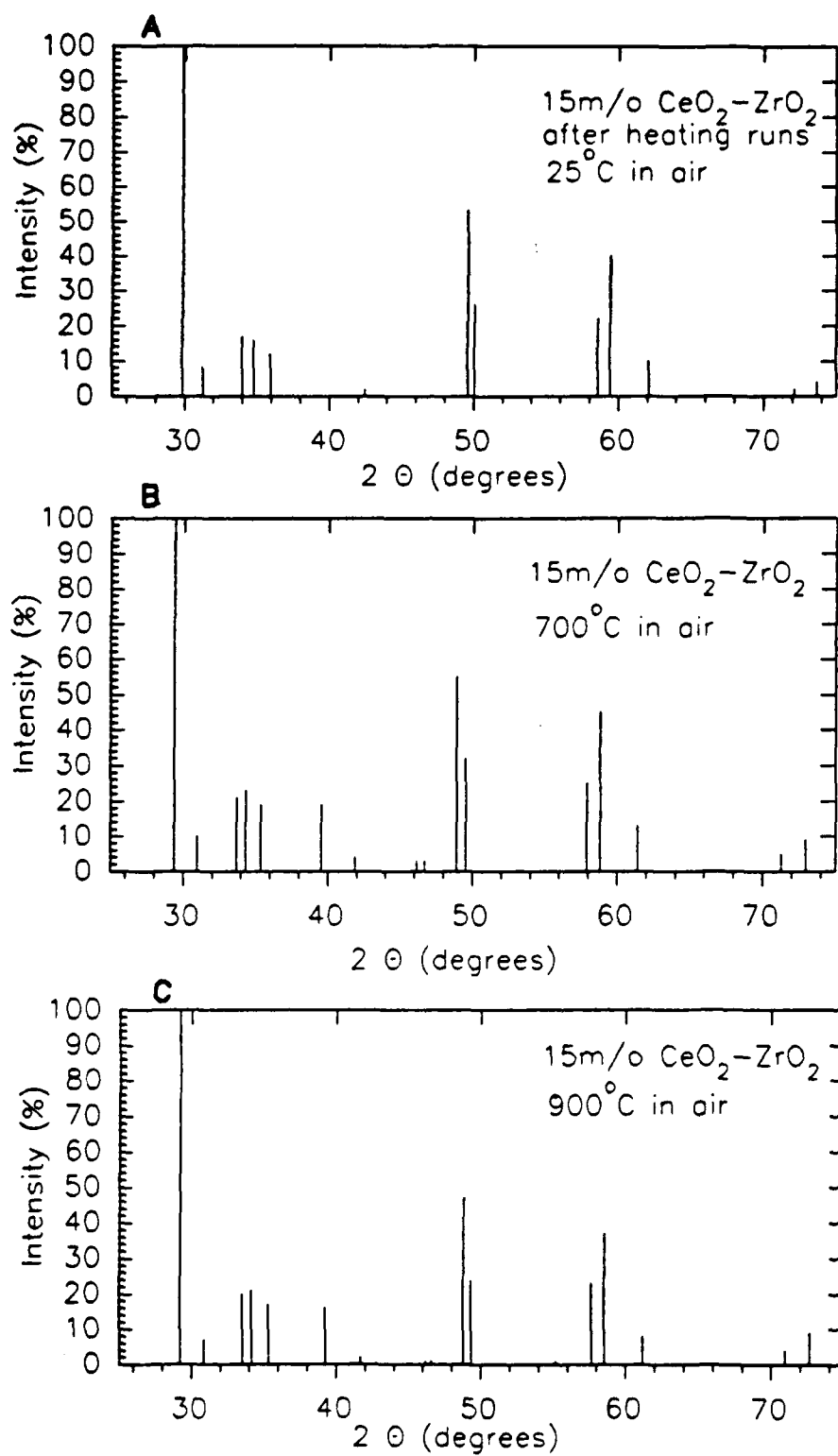Figure 36 High temperature x-ray diffraction results for 12m/o CeO_2-ZrO_2 in air.

Figure 37 High temperature x-ray diffraction results for 12m/o CeO$_2$-ZrO$_2$ in air.

which are absent in the 15m/o pattern. In addition, the 31, 35, and 39° reflection intensities do not increase as a function of temperature.

Hysteresis-like behavior has been reported for the 12 and 15m/o conductivity versus temperature experiments. Two potential causes have been cited: a repeating monoclinic-tetragonal phase transformation and the presence of an ordered phase. These results do not indicate that the monoclinic-tetragonal transformation is responsible for the aberrant conductivity versus temperature behavior. Although an ordered phase can not be dismissed, the only reported (low temperature) ordered phase, $Ce_2Zr_3O_{10}$, does not correspond to the unknown reflections.

The 20m/o sample evidenced linear electrical behavior as a function of temperature, and the sintered pellet showed only tetragonal reflections. At 700° 900°, and 25°C after heating, this specimen displayed tetragonal behavior.(Figure 38) The absence of the unidentified peaks suggests that the phase or phases responsible for these reflections contribute to the conductivity-temperature behavior in only 12 and 15 mole percent ceria.

High Temperature X-ray Diffraction at Low Oxygen Activities

Few studies have been undertaken to examine the phase behavior of the ceria-zirconia system at low oxygen partial pressures; therefore, the structural conditions which induce the n-type behavior found in Figures 19-21 are poorly understood. To test the modified Casselton model, cerium reduction is induced
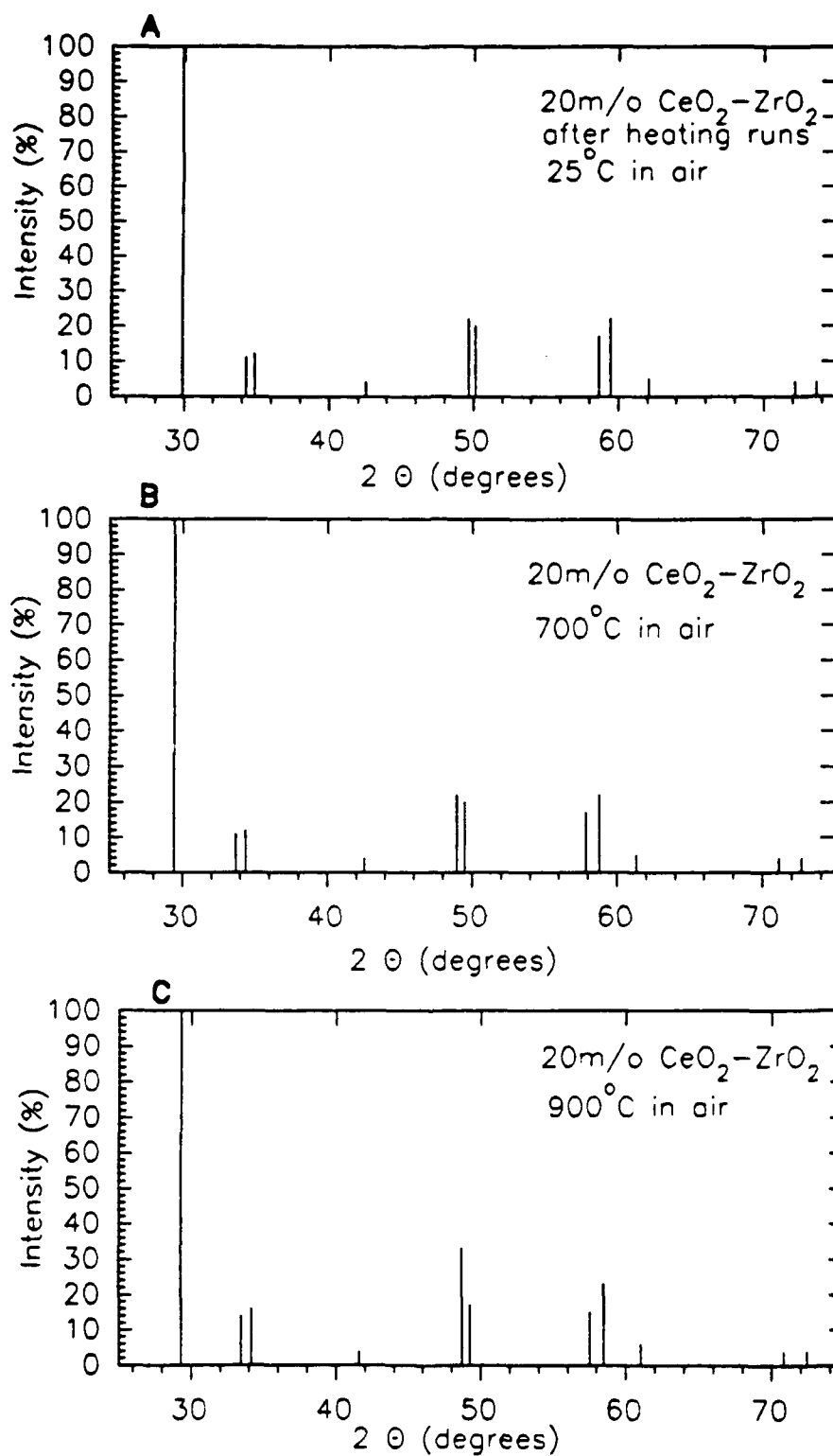
Figure 38 High temperature x-ray diffraction results for 20m/o CeO_2-ZrO_2 in air.

72

by long term exposure to low oxygen activities. Following a rapid quench, x-ray diffraction experiments are conducted on the samples immediately after quenching at 700, 800, and 900°C, and after the experiment. The high temperature measurements are carried out under an inert atmosphere ($P_{O2} \approx 10^{-15}$atm).

Figure 39 details the diffraction patterns for the quenched samples at 25°C. An initial inspection of these data prompts two conclusions:

1) The dominant reflections result from the tetragonal phase.

2) Several lesser but significant peaks occur at 31, 33, 39, 46, and 68°.

These peaks occupy positions which are almost identical to those observed in Figures 36-37. Although the patterns found in the quenched samples vary slightly in intensity from the reflections in Figures 36-37, the spectra are more distinct and are independent of composition.

Figures 40-42 demonstrate that this unknown phase or phases remain within the measurement temperature range. Upon rapid cooling, this species remains at room temperature (Figure 43).

Prior to reduction, all of the samples are a yellowish-white. After quenching, the samples darken in color. The 12 and 15m/o are a gray-brown and the 20m/o sample is almost black. These variations in color correspond to the ceria content. Since the oxygen partial pressure (3×10^{-14}atm) at which

Figure 39 X-ray diffraction results for samples held at 800°C for 6 weeks at P_{O2}=3x10^{-14}(atm), quenched, and measured immediately at 25°C.
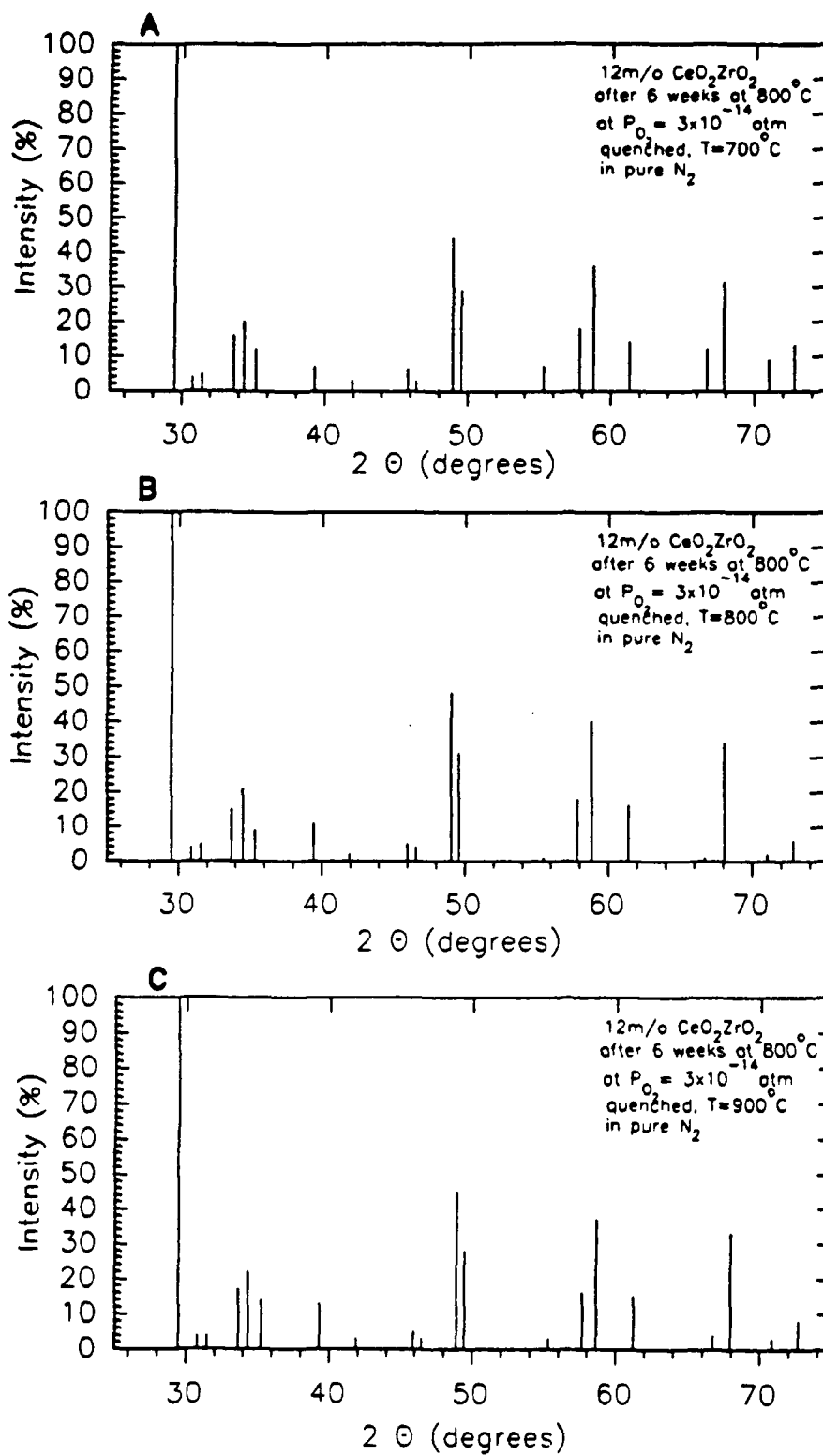
Figure 40   X-ray diffraction results for 12m/o CeO_2-ZrO_2 held at 800°C for 6 weeks at P_{O2}=3x10^{-14}(atm), and heated in pure N_2 to 735, 800, and 900°C.
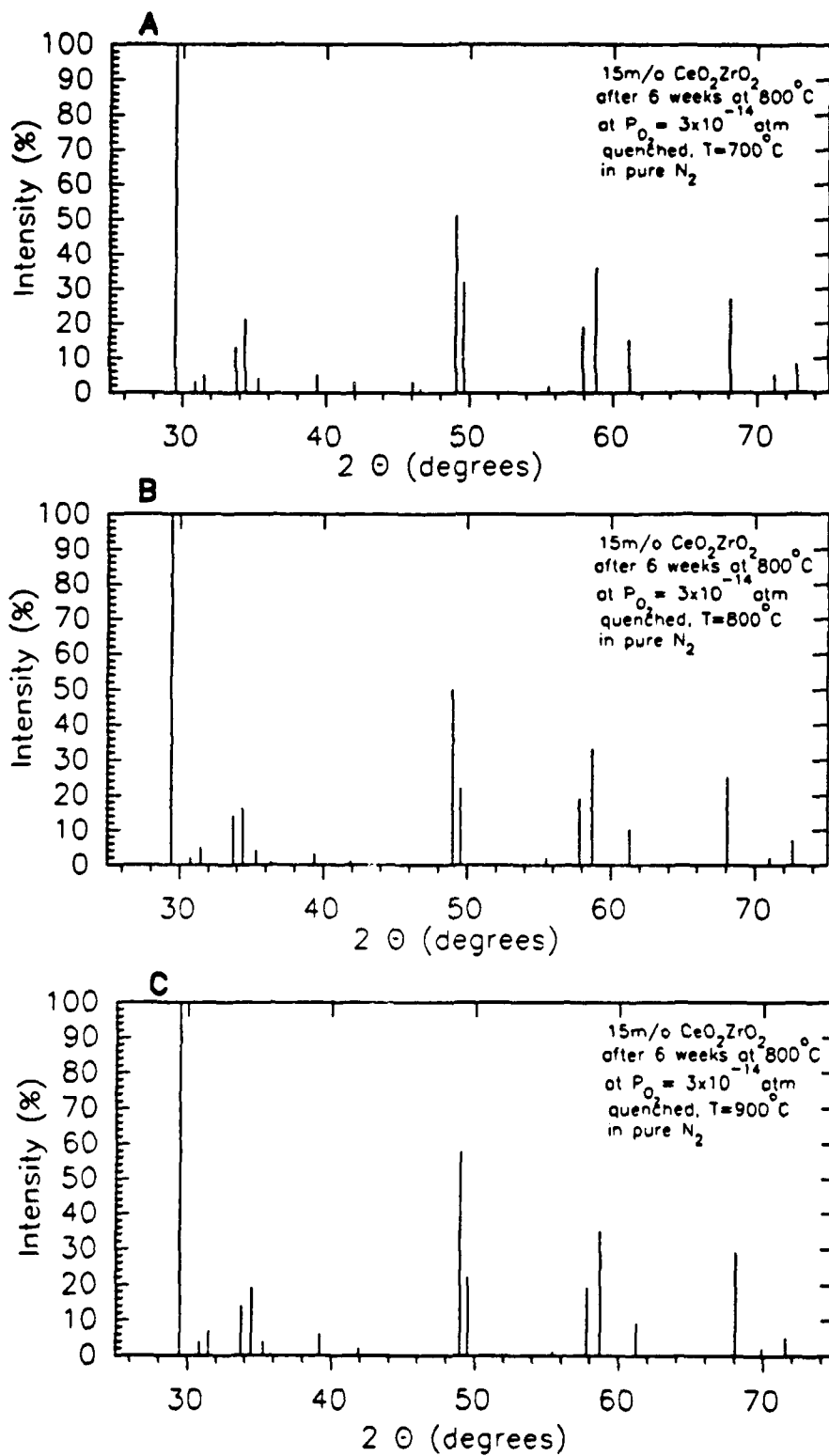
Figure 41 X-ray diffraction results for 15m/o CeO₂-ZrO₂ held at 800°C for 6 weeks at $P_{O2}=3\times10^{-14}$(atm), and heated in pure N_2 to 700, 800, and 900°C.

76

Figure 42 X-ray diffraction results for 20m/o CeO_2-ZrO_2 held at 800°C for 6 weeks at P_{O2}=3x10^{-14}(atm), and heated in pure N_2 to 700, 800, and 900°C.

77
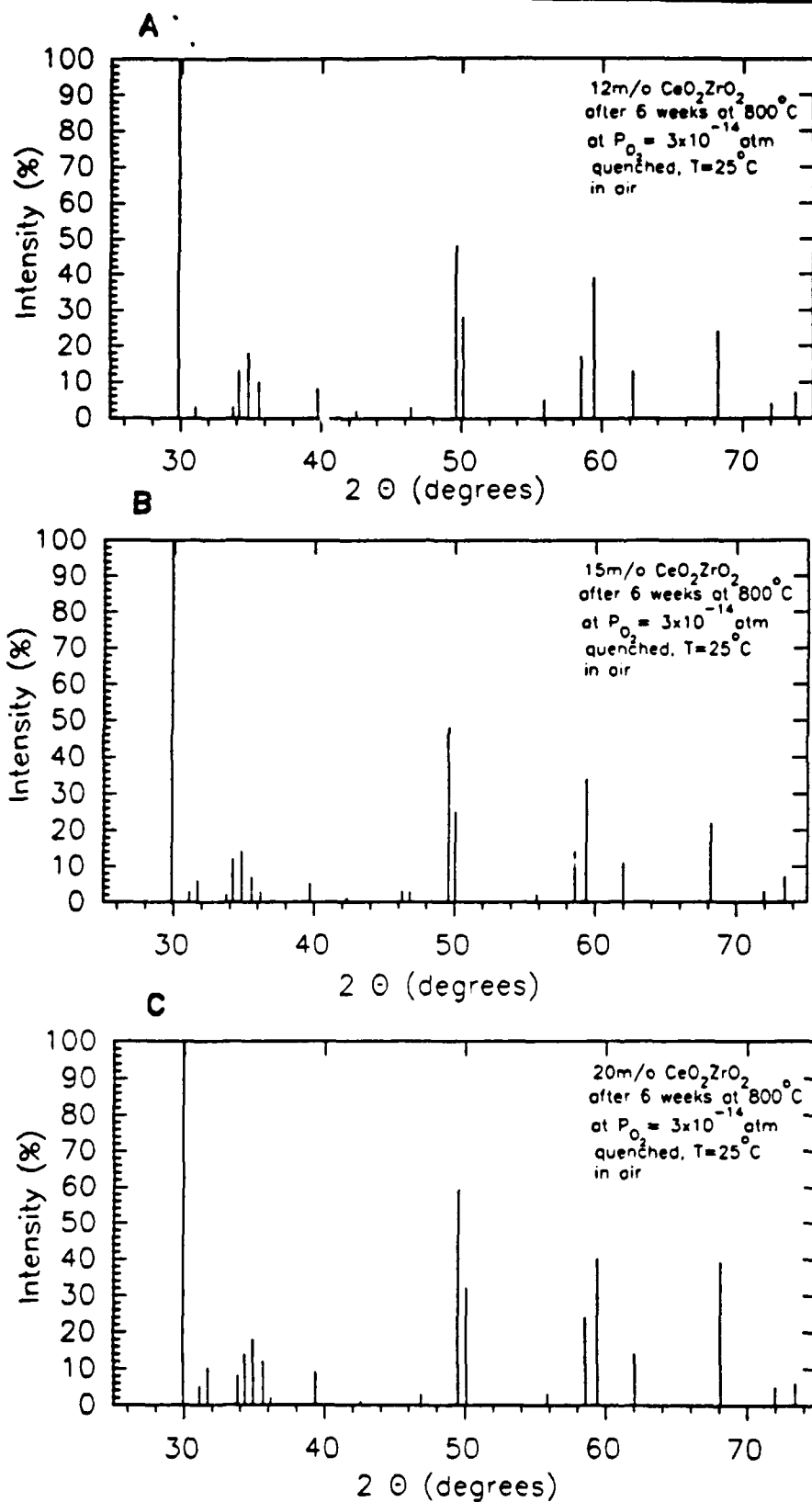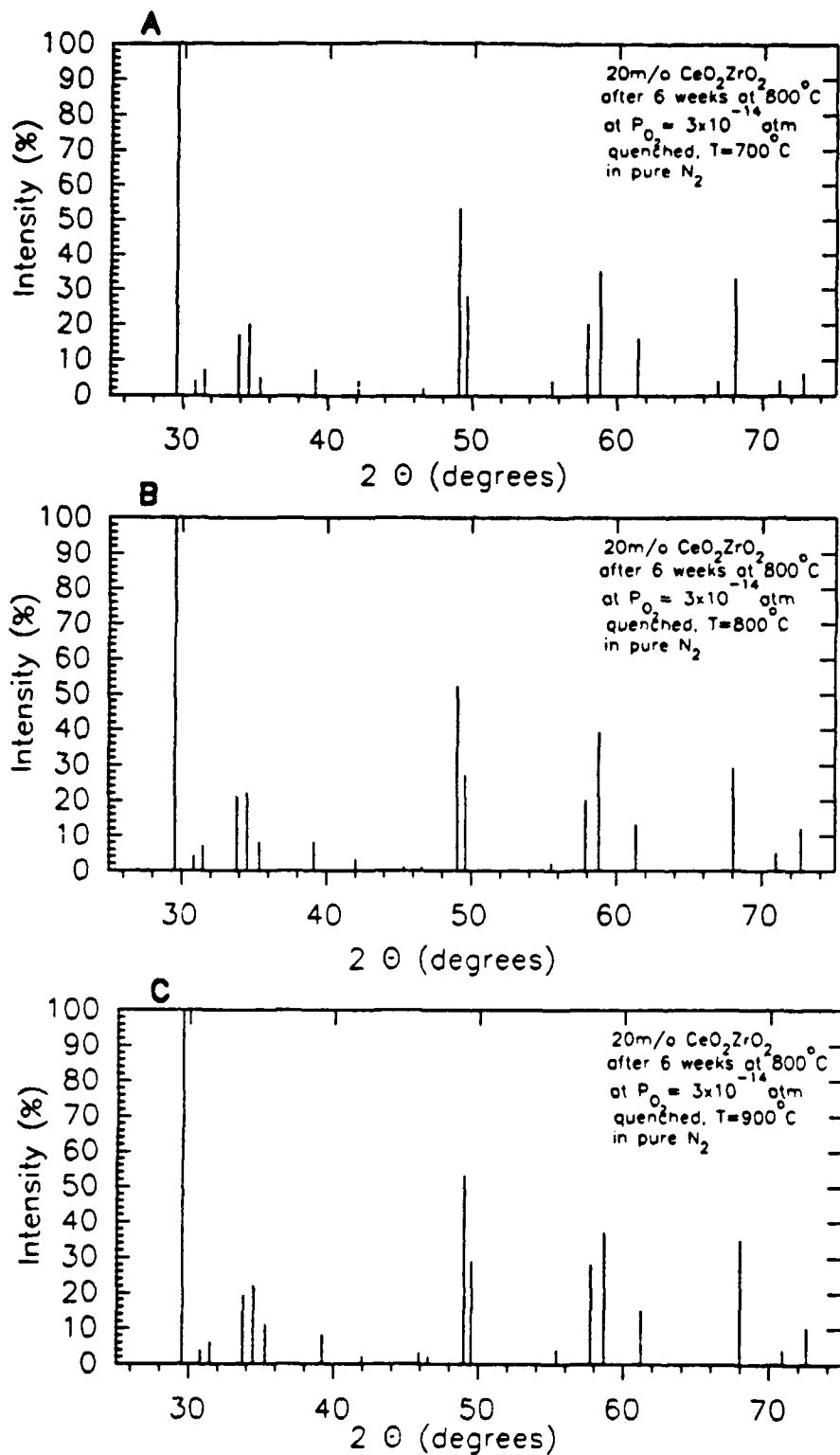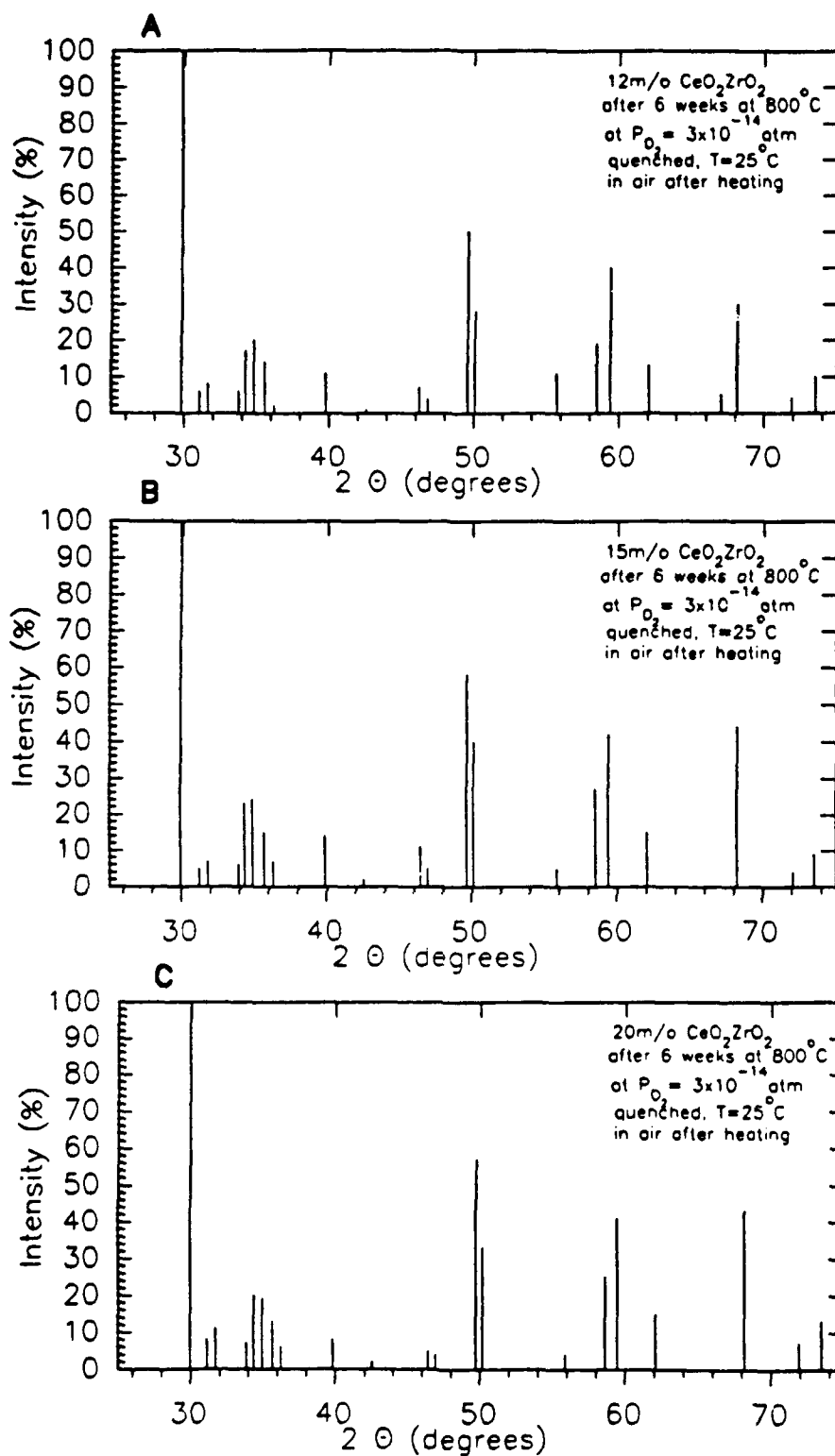
Figure 43 X-ray diffraction results for samples held at 800°C for 6 weeks at $P_{O2}=3\times10^{-14}$(atm), quenched, heated in pure N_2, cooled to 25°C.

these samples were reduced lies in the n-type region for all three sample compositions (Figures 19-21), it is logical to conclude that large concentrations of cerium ions are being reduced in this oxygen dependent region.

Point Defect Models

Before constructing a point defect model for ceria-stabilized zirconia, it is necessary to discuss the Kroger-Vink diagram for pure zirconia. Equation 8) illustrates the anti-Frenkel defect structure of ceria-doped zirconia. While this defect equation specifically applies to ι .e cubic fluorite structure, its application to tetragonal zirconia is well accepted.

$$CeO_2 = Ce_{Zr}^x + 2V_O^{\bullet\bullet} + 2O_i'' \qquad 10)$$

The equilibrium constant, K,

$$K_1 = [V_O^{\bullet\bullet}][O_i''] \qquad 11)$$

and the generalized electroneutrality condition,

$$null = [V_O^{\bullet\bullet}] + [O_i''] + [e'] + [h^+] \qquad 12)$$

$$= [V_O^{\bullet\bullet}] + [O_i''] \quad where \ [V_O\ ],\ [O_i''] >> [e'],\ [l\ ] \qquad 13)$$

demonstrates an oxygen independence in the region where these two species are the dominant charge carriers. Electrons and electron holes are minority species, but can become significant at extremes in oxygen activity. At low P_{O2}'s, electrons are produced:

$$O_O^x = V_O^{\bullet\bullet} + 2e' + 1/2O_2(g). \qquad 14)$$

Using algebraic manipulations from section 4.1.1 to determine the equilibrium

constant,

$$K_2 = [V_O^{\bullet\bullet}][e^-]^2 * P_{O2}^{1/2} \qquad 15)$$

and from electroneutrality,

$$2[V_O^{\bullet\bullet}] = [e^-] \qquad 16)$$

the electron concentration dependence on oxygen partial pressure can be

calculated

$$K_2' = [e^-]^3 * P_{O2}^{1/2} \qquad 17)$$

$$\log[e^-] \propto -1/6 \log P_{O2}. \qquad 18)$$

At high oxygen activities, the same procedure can be used for electron holes.

$$1/2 O_2 = O_i'' + 2\oplus \qquad 19)$$

$$K_3 = [O_i''][\oplus]^2 * P_{O2}^{-1/2} \qquad 20)$$

$$2[O_i''] = [\oplus] \qquad 21)$$

$$K_3' = [\oplus]^3 * P_{O2}^{-1/2} \qquad 22)$$

$$\log[\oplus] \propto 1/6 \log P_{O2}. \qquad 23)$$

These equations hold in the extremes of oxygen partial pressures, but, in the

a, ...nkel dominated realm, the concentrations of oxygen vacancies and

interstitials are constant for constant temperature. Therefore, equations 15) and

20) become

$$K_4 = [e^-]^2 * P_{O2}^{1/2} \qquad 24)$$

$$\log[e^-] \propto -1/4 \log P_{O2} \qquad 25)$$

$$K_5 = [\oplus]^2 * P_{O2}^{-1/2} \qquad 26)$$

$$\log[\oplus] \propto 1/4 \log P_{O2}. \qquad 27)$$

80

Lastly, the equilibrium between electrons and holes should not be ignored.

$$null = e^- + \oplus \qquad \qquad 28)$$

$$K_6 = [e^-][\oplus] \qquad \qquad 29)$$

To simplify description, the diagram can be divided into three regions: low oxygen activity (I), anti-Frenkel (II), and high oxygen activity (III).

In region I, the following electroneutrality and equilibrium constant equations must be met:

$$K_1 = [V_O^{\bullet\bullet}][O_i''] \qquad \qquad 11)$$

$$K_2 = [V_O^{\bullet\bullet}][e^-]^{2}*P_{O2}^{1/2} \qquad \qquad 15)$$

$$[V_O^{\bullet\bullet}] = 1/2[e^-] \qquad >> [\oplus],[O_i''] \qquad 16)$$

$$K_6 = [e^-][\oplus] \ . \qquad \qquad 29)$$

These equations are rewritten in terms of concentration.

$$[V_O^{\bullet\bullet}] = K_2^{-3}*P_{O2}^{-1/6} \qquad \qquad 30)$$

$$[O_i''] = K_1*K_3^{3}*P_{O2}^{1/6} \qquad \qquad 31)$$

$$[\oplus] = K_6*K_3^{3}*P_{O2}^{1/6} \qquad \qquad 32)$$

In region II, the same procedure is followed.

$$K_4 = [e^-]^{2}*P_{O2}^{1/2} \qquad \qquad 24)$$

$$K_5 = [\oplus]^{2}*P_{O2}^{-1/2} \qquad \qquad 26)$$

$$[V_O^{\bullet\bullet}] = [O_i''] \qquad \qquad 33)$$

$$[e^-] = K4^{-1/2}*P_{O2}^{-1/4} \qquad \qquad 34)$$

$$[\oplus] = K_5^{-1/2}*P_{O2}^{1/4} \qquad \qquad 35)$$

For region III, the method remains the same.

$$K_1 = [V_O^{\bullet\bullet}][O_i''] \qquad\qquad 11)$$

$$K_3 = [O_i''][\oplus]^2 * P_{O2}^{-1/2} \qquad\qquad 20)$$

$$[O_i''] = 1/2[\oplus] \qquad\qquad 21)$$

$$K_6 = [e'][\oplus]. \qquad\qquad 29)$$

$$[O_i''] = K_3^{-1/3} * P_{O2}^{1/6} \qquad\qquad 36)$$

$$[V_O^{\bullet\bullet}] = K_1 * K_3^{1/3} * P_{O2}^{-1/6} \qquad\qquad 37)$$

The logarithms of the concentrations are plotted as a function of the logarithm of oxygen activity. Due to the high temperatures required, definitive values for the three regions are not available; consequently, Figure 44 is only a qualitative description of the defect structure of cubic zirconia. However, the transition P_{O2} between regions I and II for calcia- and yttria-stabilized zirconia have been reported to be $< 10^{-23}$ atm.(30)

In a previous section, the electronic conductivity model proposed by Casselton (14) has been thoroughly detailed. To summarize, Ce^{4+} ions are reduced to Ce^{3+} creating oxygen vacancies to maintain electroneutrality. Electronic conduction occurs by electrons hopping between cerium ions.[+] The bulk of the experimental evidence in this work supports this model; however, the data in Figure 21 necessitate a modification of this paradigm. The inclusion of reduced cerium ion-oxygen vacancy associates extends the scope and flexibility of the model.

[+] If the ceria content is sufficiently high, localized hopping can become band conduction. Since the ionic bonding character of zirconia is large, the cerium concentration required for the localized states to overlap sufficiently to form bands may be exceedingly high.
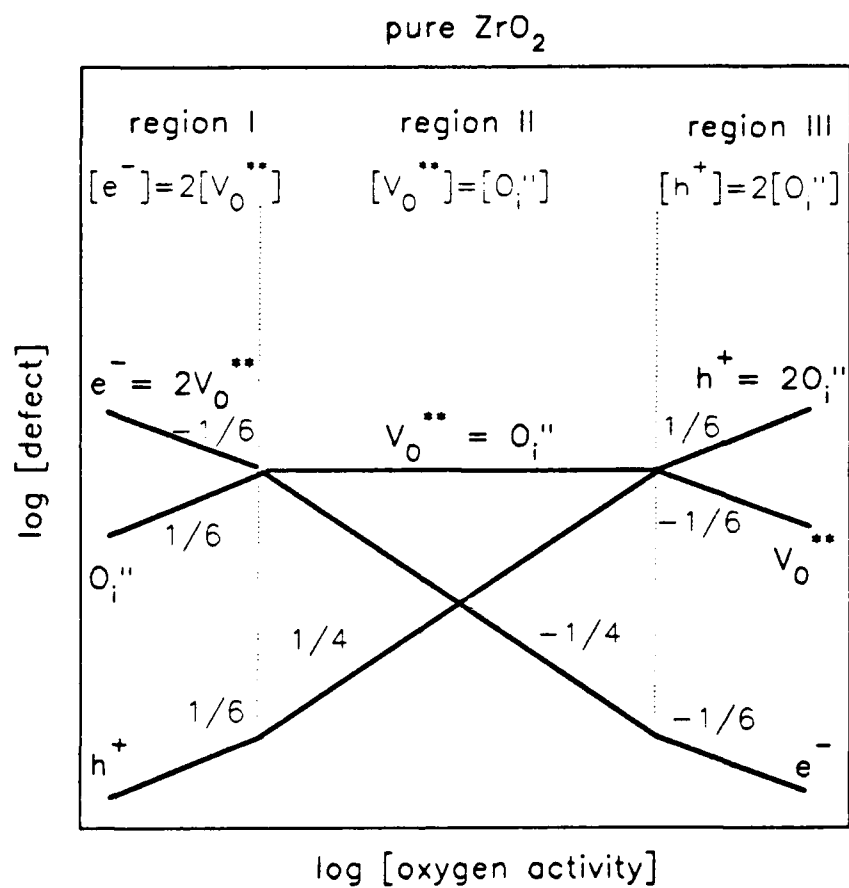
pure ZrO_2

region I   region II   region III

$[e^-]=2[V_O^{\bullet\bullet}]$ $[V_O^{\bullet\bullet}]=[O_i'']$ $[h^+]=2[O_i'']$

log [defect]

$e^- = 2V_O^{\bullet\bullet}$

$-1/6$

$V_O^{\bullet\bullet} = O_i''$

$h^+ = 2O_i''$

$1/6$

$1/6$

O_i''

$-1/6$

$V_O^{\bullet\bullet}$

$1/4$

$-1/4$

$1/6$

$-1/6$

h^+

e^-

log [oxygen activity]

Figure 44 A Kroger-Vink diagram depicting the oxygen dependence of defect concentraticns in cubic zirconia.

83

The construction of a defect model for ceria-doped zirconia requires the same approach as pure zirconia. The high oxygen activity regime is omitted due to a dearth of experimental evidence. In region I, reduced cerium ions are added to the list of defect species. Therefore, the following defect equations, equilibrium constants and electroneutrality conditions must be met:

$$2Ce_{Zr}^x + 4O_O^x = 2Ce_{Zr}' + V_O^{\bullet\bullet} + 3O_O^x + 1/2O_2 \qquad 38)$$
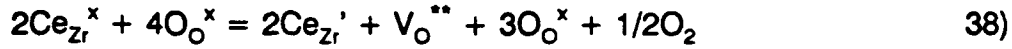
$$K_7 = [Ce_{Zr}']^2[V_O^{\bullet\bullet}]*P_{O2}^{1/2} \qquad 39)$$

$$[Ce_{Zr}'] = 2[V_O^{\bullet\bullet}] \quad >> [O_i''],[e'],[\oplus] \qquad 40)$$

$$K_1 = [V_O^{\bullet\bullet}][O_i''] \qquad 11)$$

$$K_2 = [V_O^{\bullet\bullet}][e']^2*P_{O2}^{1/2} \qquad 15)$$

$$K_3 = [O_i''][\oplus]^2*P_{O2}^{-1/2} \qquad 20)$$

$$K_6 = [e'][\oplus]. \qquad 29)$$

These equations are rewritten in terms of concentration.

$$[V_O^{\bullet\bullet}] = K_7^{1/3}*P_{O2}^{-1/6} \qquad 41)$$

$$[O_i''] = K_1*K_3^{-1/3}*P_{O2}^{1/6} \qquad 42)$$

$$[\oplus] = K_1^{1/2}*K_3^{1/2}*K_7^{-1/6}*P_{O2}^{1/3} \qquad 43)$$

$$[e'] = K_2^{1/2}*K_7^{1/6}*P_{O2}^{-1/3} \qquad 44)$$

In region II, the vacancy and interstitial concentrations are equivalent and constant.

$$[V_O^{\bullet\bullet}] = [O_i''] \quad >> [Ce_{Zr}'],[e'],[\oplus] \qquad 33)$$

The concentration equations are rewritten:

$$K_7 = [Ce_{Zr}']^2[V_O^{\bullet\bullet}]*P_{O2}^{1/2} \qquad 39)$$

$$[Ce_{Zr}{}'] = K_{7'}{}^{1/2}*P_{O2}{}^{-1/4} \qquad 45)$$

$$[e^-] = K_4{}^{1/2}*P_{O2}{}^{-1/4} \qquad 46)$$

$$[\oplus] = K_5{}^{-1/2}*P_{O2}{}^{1/4} \qquad 47)$$

Figure 45 illustrates the defect behavior for regions I and II as defined by the concentration constraints.

Electrical conductivity results provide convincing evidence for the association of cerium ions and oxygen vacancies. These associates would be formed by the following defect reaction:

$$2Ce_{Zr}{}^x + 4O_O{}^x = Ce_{Zr}{}' + (Ce_{Zr}{}'V_O{}^{\bullet\bullet})^\bullet + 3O_O{}^x + 1/2O_2 \qquad 48)$$
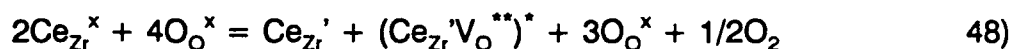
If the dopant-vacancy associate becomes the conduction controlling defect, the ensuing concentration relations pertain to region I.

$$K_8 = [Ce_{Zr}{}'][(Ce_{Zr}{}'V_O{}^{\bullet\bullet})^\bullet]*P_{O2}{}^{1/2} \qquad 49)$$

$$[Ce_{Zr}{}'] = [(Ce_{Zr}{}'V_O{}^{\bullet\bullet})^\bullet] = [V_O{}^{\bullet\bullet}] = K_8{}^{1/2}*P_{O2}{}^{-1/4} \qquad 50)$$

$$[O_i{}''] = K_1*K_8{}^{-1/2}*P_{O2}{}^{1/4} \qquad 51)$$

$$[e^-] = K_2{}^{1/2}*K_8{}^{-1/4}*P_{O2}{}^{-3/8} \qquad 52)$$

$$[\oplus] = K_3{}^{1/2}*K_8{}^{1/4}*P_{O2}{}^{3/8} \qquad 53)$$

In region II, the vacancy and interstitial concentrations are constant;

$$[V_O{}^{\bullet\bullet}] = [O_i{}''] \qquad 33)$$

therefore, the associate concentration is equivalent to the reduced cerium concentration.

$$[(Ce_{Zr}{}'V_O{}^{\bullet\bullet})^\bullet] = [Ce_{Zr}{}'] \qquad 54)$$
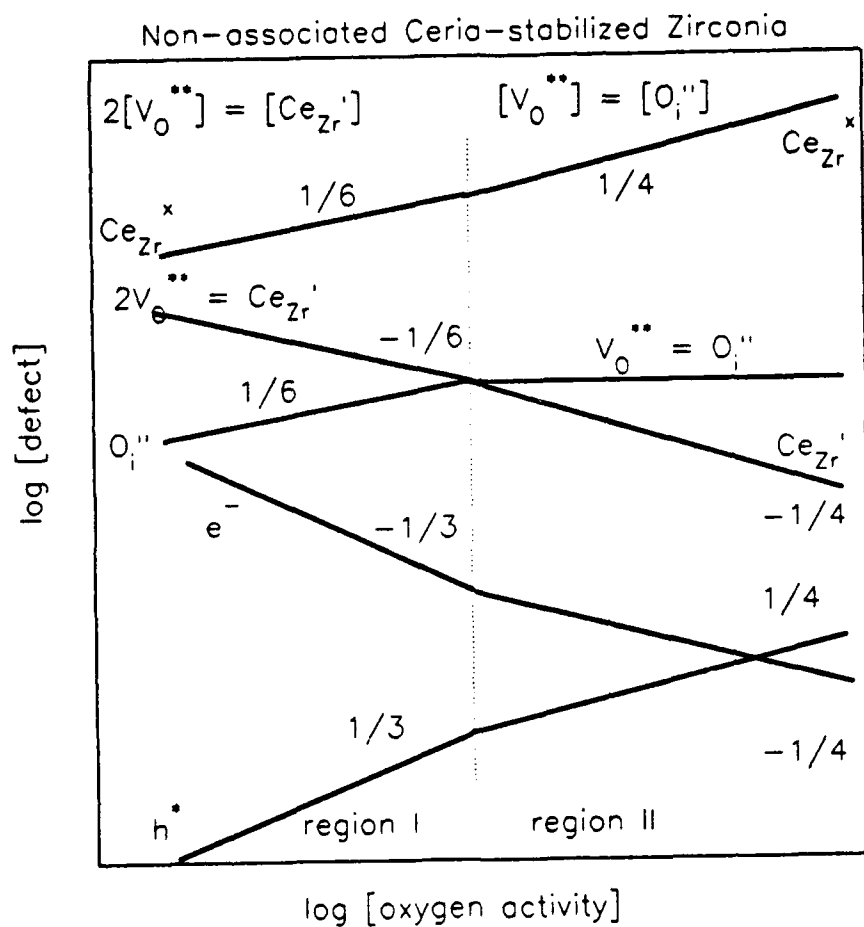
$$[Ce_{Zr}{}'] = K_8{}^{1/2}*P_{O2}{}^{-1/4} \qquad 55)$$

Figure 45 A Kroger-Vink diagram illustrating the oxygen dependence of defect concentrations in ZrO_2-CeO_2 without associates.

$$[e^-] = K_4^{1/2} * P_{O2}^{-1/4} \qquad \qquad 46)$$

$$[\oplus] = K_5^{-1/2} * P_{O2}^{1/4} \qquad \qquad 47)$$

Figure 46 illustrates the oxygen dependence of point defects in ceria-stabilized zirconia for the associate model. The creation of associated defects not only alters the oxygen dependence of the dominant point defect, but affects the dependence of the minority species. In region I (low P_{O2}), the influence of oxygen activity on defect concentration is enhanced. This difference in behavior is reflected in increased slope severity. The slope of the cerium ion, vacancy, and interstitial concentration changes from -1/6 to -1/4 while the electron and hole slopes are altered from -1/3 to -3/8. The effects of association are limited to region I because the region II (anti-Frenkel) oxygen dependencies are unaffected by associate formation. This conclusion compares favorably with the conductivity versus temperature results in Figure 22-24. When the P_{O2} equals 0.21 atm, all three sample compositions have similar activation energies. It is only in the n-type region that changes occur in oxygen dependence and activation energies. Figure 45 corresponds well with the experimental results for 12 and 15m/o ceria although the 15 mole percent oxygen dependence is much less definitive. In Figure 21, the conductivity behavior at 700°C is in good agreement with the associate model (Figure 46). At 900°C, the data do not conform to either model; a more accurate description would be a combination of both paradigms.
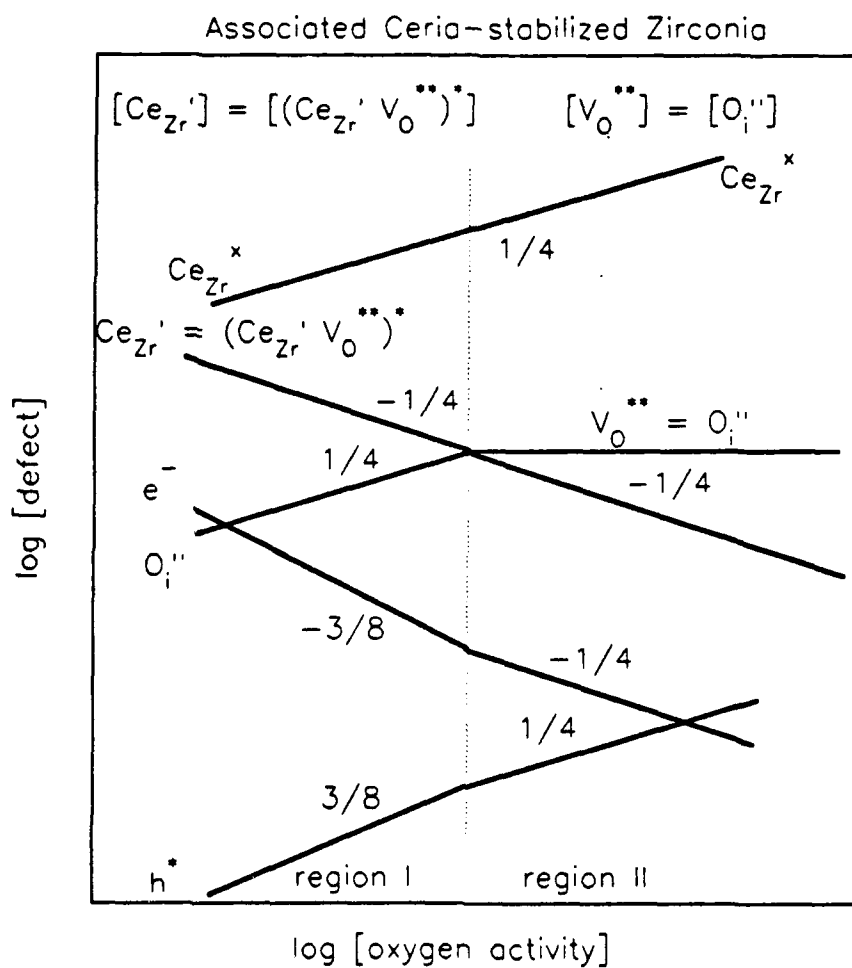
Figure 46 A Kroger-Vink diagram illustrating the oxygen dependence of defect concentrations in ZrO_2-CeO_2 with $(Ce_{Zr}'V_O^{\bullet\bullet})^{\bullet}$ associates.

CONCLUSIONS

HOT CORROSION OF NICKEL AND CHROMIUM-BASED ALLOYS

The results attained collectively provide a clarification of the hot corrosion process. The following conclusions about hot corrosion have been reached:

1) The gas-Na_2SO_4 melt interface is not rate controlling.

2) Diffusion in the boundary layers at the gas-melt interface is not rate controlling.

3) Electronic transport through the bulk melt is not rate controlling.

4) An increasing amount of Na_2SO_4 result in a greater weight gain per unit area for a given activity of Na_2O in the Na_2SO_4. This indicates that the capacity of Na_2SO_4 , prior to precipitation of products, to accommodate the products of the hot corrosion does influence the rate of reaction.

5) The above points appear to indicate that the processes occurring at or near the metal-salt interface seem to be of prime importance.

Na_2SO_4 STUDIES

It was observed that the total electrical conductivity of pure Na_2SO_4 was of the order of 2.32×10^{-1} (ohm-cm)$^{-1}$ and varied only slightly with changes in the activities of Na_2O. The cationic transport number of a pure Na_2SO_4 melt was found to be about 0.984 at 1173 K and was almost a constant as a

function of Na_2O. The partial conductivity of electrons in Na_2SO_4 was about two orders of magnitude less than the total electrical conductivity. Thus, the transport number of electrons, t_e is of the order of 10^{-3} in a pure Na_2SO_4 melt at 1173 K. The self-diffusion coefficient of Na^+ ions was estimated utilizing the above experimental data and its average value was 8.1 x 10^{-6} cm^2/sec.

The transient relaxation method was employed to determine the diffusion coefficient of electrons in a pure Na_2SO_4 melt and its value was about 3.15 x $10^{-3}$$cm^2$/sec at 1173 K.

The introduction of the protective oxides such as Cr_2O_3, Al_2O_3, and SiO_2 into a Na_2SO_4 melt has significant changes in transport-properties of the melt. These oxides decrease the electron conductivities and increase the electron hole conductivities as compared to pure Na_2SO_4.

ELECTRONIC AND DEFECT BEHAVIOR IN CERIA-STABILIZED ZIRCONIA

1) As a function of oxygen activity, 12, 15, and 20m/o ceria-stabilized zirconia conductivities exhibit two regions of electrical behavior:

i) at moderate partial pressures $(1 > P_{O2} > 10^{-9} - 10^{-15}$ atm), an oxygen independent domain has been observed which follows anti-Frenkel behavior, and

ii) at low P_{O2}'s, an oxygen dependent range has been discovered which displays n-type semi-conductor behavior.

The threshold oxygen partial pressure between these regions varies as a

function of temperature and ceria content.

2) The slopes of the log σ - log P_{O2} plots can assist in the characterization of the dominant charge carrier. In the n-type region, the 12m/o CeO_2-ZrO_2 slope suggests that reduced cerium ions generate electrons. These electrons conduct via hopping (or bands) amidst the cerium ions by the reaction:

$$Ce_{Zr}' \dashrightarrow Ce_{Zr}^x + e^- \dashrightarrow Ce_{Zr}'.$$
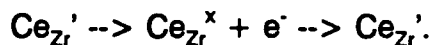
(The slopes in the 15 mole percent sample provide a less definite interpretation.)

3) The 20 mole percent ceria samples have a more complex conduction mechanism. The log σ - log P_{O2} slopes do not correspond to values of the other compositions. At 700°C, the results indicate the formation of Ce^{3+}-oxygen vacancy associates. These associates break up at higher temperatures, and the specimen reverts to the reduced cerium ion conduction mechanism described in 2).

4) At P_{O2} = 0.21 atm, the three compositions have similar activation energies which are comparable to oxygen vacancy activation energies in yttria- and calcia-stabilized zirconia. Therefore, oxygen vacancies are the dominant charge carrier in this region.

5) At low oxygen activities, the difference between the activation energies of the 15 and 20m/o and the 12 m/o sample is about 0.30 eV. This value corresponds closely with calculated association energies for dopant ion-vacancy pairs, thus, confirming the formation of associates in samples with

higher ceria contents.

6) In temperature cycling experiments, the 12 and 15m/o specimens showed hysteresis-like conductivity behavior. High temperature x-ray diffraction demonstrated that monoclinic-tetragonal transformations or the formation of known ordered phases are not responsible for these phenomena. In conductivity versus temperature measurements, the 20 mole percent ceria sample evidenced a single slope through two thermal cycles. X-ray data confirmed that only the tetragonal species exists in this material at temperatures below 900°C.

7) Between 800 and 900°C, ionic transport measurements indicate that in the n-type region the conduction modes are almost entirely electronic.

8) For 12, 15, and 20m/o ceria, high temperature x-ray diffraction experiments in air indicate that the tetragonal species is the dominant entity at high temperatures; however, in the 12 and 15 mole percent specimens, unknown reflections have been observed. These reflections do not correspond with any known zirconia polymorph or ceria-zirconia ordered phase.

9) At low P_{O2}'s, the high temperature x-ray patterns exhibit the same unidentified peaks. It is certain that the samples were reduced prior to measurement, and that these peaks are a product of this reduction process.

10) Point defect models have been constructed for both unassociated and associated reduced cerium ions.

REFERENCES

1. N.S. Bornstein, Literature Review of Inhibition of Vanadate Attack, ONR N00014-88-M-0013, June 1988

2. N.S. Bornstein and M.A. DeCrescente, Corrosion, 26, 7, 1988, 209-14.

3. K. Luthra and D. Shores, A Study of the Mechanism of Hot Corrosion in Environments Containing NaCl, NRL Contract N000173-77-C-0253, Fifth Quarterly Progress Report, November 1978

4. K. Luthra and D. Shores, A Study of the Mechanism of Hot Corrosion in Environments Containing NaCl, NRL Contract N000173-77-C-0253, Sixth Quarterly Progress Report, February 1979

5. K. Luthra and D. Shores, A Study of the Mechanism of Hot Corrosion in Environments Containing NaCl, NRL Contract N000173-77-C-0253, Sixth Quarterly Progress Report, May 1979

6. R.L. Jones and S. Gadomski, J. Electrochem. Soc., 124, 10, 1977, 1641-1648.

7. D. Shores, D., D. McKee, and T. Kerr, Sodium Chloride Induced Hot Corrosion: Literature Survey and Preliminary Experiments, Contract 7A003-CIP105 (EPN HT05), April 1976

8. R.L. Jones, Low Quality Fuel Problems With Advanced Materials, NRL Report 6252, August 1988

9. E. Fitzer and J. Schwab, Corrosion, 12, 1956, 49-54.

10. H. Flood and T. Forland, Acta Chem. Scand., 1, 1947, 592.

11. J. A. Goebel and F. S. Petit, Met. Trans., 1, 1970, 1943.

12. K. Weiss, Z, Phys. Chem. (N.F.), 59, 1968 242.

13. J. Stringer, "Hot Corrosion in Gas Turbines," Princeton, Electrochemical Society, 1974, p. 29.

14. R.E.W. Casselton, Phys. Stat. Sol. A, 1, 1970, 788-794.

15. P. Kofstad and A.Z. Hed, J. Am. Ceram. Soc., 50, 1967, 681.

16. A.B. Sobolev, A.N. Varaksin, O.A. Keda, and A.P. Khaimenov, Phys. Stat. Sol. B, 162, 1990, 165.

17. A. Nakamura and J.B. Wagner, J. Electrochem. Soc., 127, 11, 1980, 2325-2333.

18. A. Nakamura and J.B. Wagner, J. Electrochem. Soc., 133, 8, 1986, 1542-1548.

19. P. Duwez and F Odell, J. Am. Ceram. Soc., 33, 1950, 274.

20. E.C. Subbarao, Science and Technology of Zirconia, Advances in Ceram. Vol.3, ed. by Heuer, A. H. and L. W. Hobbs, (Am. Ceram. Soc., 1981)

21. A.N. Cormack and C.R.A. Catlow, Transport in Non-stoichiometric Compounds, ed. G. Simkovich and V. Stubican, (Plenum Press, New York, 1985) p.101-110.

22. E. Tani, M. Yoshimura, and S. Somiya, J. of the Am. Ceram. Soc., 66, 7, 1983, 506-510.

23. P. Duran, M. Gonzalez, C. Moure, J.R. Jurado, C. Pascual, J. Mat. Sci., 25, 1990, 5001-5006.

24. H. McMurdie, Pow. Diff. Jour., 1, 1986, 275.

25. G. Teufer, Acta. Cryst., 15, 1962, 1187.

26. G. Spinolo and S. Meriani, Pow. Diff., 2, 4, 1987, 255-256.

27. J. Katz, J. Am. Ceram. Soc., 54, 1971, 531.

28. V. Longo and D. Minichelli, J. Am. Ceram. Soc., 56, 1973, 600.

29. H. Toraya, M. Yoshimura, and S. Somiya, J. Am. Ceram. Soc., 67, 1984, C119-121.

30. T.H. Etsell and S.N. Flengas, J. Electrochem. Soc., 119, 1, 1972, 1-7.